



LATTICE BOLTZMANN METHOD APPLIED TO MULTIPHASE FLOWS AND  
PREFERENTIAL PATHS IN POROUS MEDIA

Ramon Gomes de Castro Lourenço

Dissertação de Mestrado apresentada ao Programa de Engenharia Química, COPPE, da Universidade Federal do Rio de Janeiro, como parte dos requisitos necessários à obtenção do título de Mestre em Engenharia Química.

Orientadores: Frederico Wanderley Tavares  
Pedro Henrique Davi Constantino

Rio de Janeiro  
Abril de 2021

LATTICE BOLTZMANN METHOD APPLIED TO MULTIPHASE FLOWS AND  
PREFERENTIAL PATHS IN POROUS MEDIA

Ramon Gomes de Castro Lourenço

DISSERTAÇÃO SUBMETIDA AO CORPO DOCENTE DO INSTITUTO ALBERTO  
LUIZ COIMBRA DE PÓS-GRADUAÇÃO E PESQUISA DE ENGENHARIA DA  
UNIVERSIDADE FEDERAL DO RIO DE JANEIRO COMO PARTE DOS REQUISITOS  
NECESSÁRIOS PARA A OBTENÇÃO DO GRAU DE MESTRE EM CIÊNCIAS EM  
ENGENHARIA QUÍMICA.

Orientadores: Frederico Wanderley Tavares  
Pedro Henrique Davi Constantino

Aprovada por: Prof. Frederico Wanderley Tavares  
Eng. Pedro Henrique Davi Constantino  
Prof. Luís Fernando Mercier Franco  
Prof. Gabriel Gonçalves da Silva Ferreira

RIO DE JANEIRO, RJ - BRASIL

ABRIL DE 2021

Lourenço, Ramon Gomes de Castro

Lattice Boltzmann Method Applied to Multiphase Flows and Preferential Paths in Porous Media / Ramon Gomes de Castro Lourenço. – Rio de Janeiro: UFRJ/COPPE, 2021.

XXII, 135 p.: il.; 29,7 cm.

Orientadores: Frederico Wanderley Tavares

Pedro Henrique Davi Constantino

Dissertação (mestrado) – UFRJ/ COPPE/ Programa de Engenharia Química, 2021.

Referências Bibliográficas: p. 117-130.

1. Mesoscale modeling. 2. Pseudopotential model. 3. Droplet dynamics. 4. Pore-Scale. 5. Preferential flow. I. Tavares, Frederico Wanderley *et al.* II. Universidade Federal do Rio de Janeiro, COPPE, Programa de Engenharia Química. III. Título.

*Para os meus avós, Edson e Therezinha,  
que me ensinaram quão simples cada momento pode ser.*

# Agradecimentos

Começo agradecendo aos meus pais, José Randall e Tereza Cristina, que, durante todo o meu crescimento, nunca deixaram de estimular meu estudo e minha curiosidade. Se hoje eu amo ciência, é porque eles participaram desta construção ativamente. Obrigado por me estruturarem e me prepararem para a realidade. Vocês sempre estarão no meu coração.

Agradeço também ao meu amor, Suzana Gomes, por todo seu companheirismo, compreensão e encorajamento. O apoio que nos damos mutuamente é o que nos faz subir cada dia mais no nosso relacionamento e na nossa carreira. É excepcional saber que podemos confiar um no outro. Obrigado por chorar comigo nos momentos ruins e comemorar nos momentos bons. Obrigado por ser quem você é e por me completar na medida certa.

Agradeço a todo o laboratório ATOMS pela amizade, solidariedade e carisma que cada um dos seus membros demonstrou desde a minha chegada ao laboratório. Agradeço também a presença e o bom humor constante dos meus colegas do PEQ e da Representação Discente 2019, que ajudaram a tornar o nosso ambiente de estudo tão agradável. Em especial, registro o meu muito obrigado a Renan Barbosa, a Tamires Silva e a Alan Nunes, que sempre estiveram por perto, seja trazendo boas conversas ou simplesmente compartilhando nossas frustrações.

Agradeço às agências financiadoras CAPES (Coordenação de Aperfeiçoamento de Pessoal de Nível Superior) e FAPERJ (Fundação de Amparo à Pesquisa do Estado do Rio de Janeiro) pelas bolsas concedidas, sem as quais não seria possível a realização deste trabalho.

Finalmente agradeço muito aos meus orientadores, Frederico Tavares e Pedro Constantino, pela confiança e pelo conhecimento transmitido. Obrigado pela preocupação que ambos sempre expressaram para com a minha saúde e a da minha família durante a pandemia de COVID-19, que afetou parte do meu mestrado. Agradeço o carinho, a tranquilidade, a disponibilidade para conversas, a liberdade para tomadas de decisão, e as incomparáveis dicas que tanto ajudaram na composição deste trabalho. Vocês são, inquestionavelmente, responsáveis por meu amadurecimento acadêmico nesses dois últimos anos.

Resumo da Dissertação apresentada à COPPE/UFRJ como parte dos requisitos necessários para a obtenção do grau de Mestre em Ciências (M.Sc.).

## MÉTODO LATTICE BOLTZMANN APLICADO A ESCOAMENTOS MULTIFÁSICOS E CAMINHOS PREFERENCIAIS EM MEIO POROSO

Ramon Gomes de Castro Lourenço

Abril/2021

Orientadores: Frederico Wanderley Tavares

Pedro Henrique Davi Constantino

Programa: Engenharia Química

O Método Lattice Boltzmann (LBM) tem sido crescentemente adotado na Engenharia Química. Embora popular e fácil de implementar, o modelo pseudopotencial de Shan-Chen possui limitações como inconsistência termodinâmica, geração de velocidades espúrias, dentre outras. Vários modelos alternativos que corrigem essas limitações são encontrados na literatura. Neste trabalho, por meio de manipulações algébricas, propomos um modelo unificado a partir do qual diferentes forças de interação multifásicas podem ser recuperadas. Simulações isotérmicas e monocomponentes de transição de fase de gotas estacionária e oscilante validam o modelo numericamente como também reforçam que as forças de interação são essencialmente equivalentes. Os parâmetros multifásicos são ajustados com base nas densidades da fase vapor na região de baixa temperatura da curva de coexistência de Maxwell. A consistência termodinâmica é melhorada ao escrever os parâmetros como funções da temperatura reduzida, sem perda de estabilidade numérica ou aumento das velocidades espúrias. A validade de um modelo preditor de caminho preferencial para um regime não Darcyano é verificada e seus resultados são confrontados com os das simulações. LBM recupera com sucesso a equação de Forchheimer. Embora o modelo preveja razoavelmente os caminhos preferidos, as contribuições inerciais no regime de Forchheimer fazem o padrão poroso, a forma do grão e as deflexões do caminho perturbarem essas previsões.

Abstract of Dissertation presented to COPPE/UFRJ as a partial fulfillment of the requirements for the degree of Master of Science (M.Sc.).

LATTICE BOLTZMANN METHOD APPLIED TO MULTIPHASE FLOWS AND  
PREFERENTIAL PATHS IN POROUS MEDIA

Ramon Gomes de Castro Lourenço

April/2021

Advisors: Frederico Wanderley Tavares

Pedro Henrique Davi Constantino

Department: Chemical Engineering

The Lattice Boltzmann Method (LBM) has been increasingly adopted in Chemical Engineering. Although popular and easy to implement, the Shan-Chen pseudopotential model suffers from many limitations regarding thermodynamic consistency, the formation of spurious currents, and others. Several alternative models that mitigate these effects are found in the literature. Through algebraic manipulations, we propose a unified model from which these multiphase interaction forces can be recovered. Isothermal phase transition simulations of single-component stationary and oscillating droplets validate the model numerically and reinforce that the multiphase forces are essentially interchangeable. The multiphase parameters are selected based on the vapor densities at low temperatures in the Maxwell coexistence curve, where there is a narrow range of optimal values. Writing them as functions of the reduced temperature enhances the thermodynamic consistency without losing stability or increasing spurious velocities. The validity of a preferential path predictor in a non-Darcy regime is also verified, and the results are confronted with the simulated preferred paths. LBM successfully recovers the Forchheimer equation. Although the model reasonably predicts the preferred paths, the inertial contributions in the Forchheimer regime make the porous pattern, grain shape, and path deflections disturb those predictions.

# Contents

<b>List of Figures</b> .....	x
<b>List of Symbols</b> .....	xv
<b>List of Acronyms</b> .....	xxii
<b>Chapter 1: Introduction</b> .....	1
1.1 Motivation .....	1
1.2 Objectives .....	2
1.3 Document structure .....	3
<b>Chapter 2: Theoretical background</b> .....	4
2.1 Boltzmann Transport Equation .....	4
2.2 Lattice Boltzmann Method .....	6
2.3 Collision models .....	10
2.3.1 Bhatnagar-Gross-Krook model .....	11
2.3.2 Multiple-Relaxation-Time model .....	12
2.4 Boundary conditions .....	14
2.4.1 Bounce-back scheme .....	15
2.4.2 Periodic condition .....	18
2.5 Forcing schemes .....	20
<b>Chapter 3: Recovery of transport equations</b> .....	23
3.1 Chapman-Enskog expansion .....	23
3.2 Moment evaluation .....	28
3.3 Continuity equation .....	32
3.4 Navier-Stokes equation .....	34
<b>Chapter 4: Computational aspects of LBM</b> .....	57
4.1 Couette flow .....	58
4.2 Square-cavity flow .....	67
<b>Chapter 5: Unified multiphase model</b> .....	71
5.1 Introduction .....	71
5.2 Pseudopotential multiphase models .....	73

5.2.1 Shan-Chen multiphase model .....	73
5.2.2 Other multiphase models .....	73
5.3 Equations of State and thermodynamic consistency .....	76
5.4 A unified multiphase model .....	78
5.4.1 Model proposal .....	78
5.4.2 Checking the pressure tensors .....	80
5.5 Static droplet .....	83
5.5.1 Methodology .....	83
5.5.2 Results and discussion .....	84
5.5.2.1 Numerical validation .....	84
5.5.2.2 Parameter improvement .....	88
5.6 Droplet oscillation .....	91
5.6.1 Methodology .....	91
5.6.2 Results and discussion .....	92
5.7 Conclusions .....	97
<b>Chapter 6: Preferential paths of non-Darcy flow .....</b>	<b>99</b>
6.1 Introduction .....	99
6.2 Theoretical description .....	101
6.2.1 Physical properties .....	101
6.2.2 Governing equations in porous media .....	103
6.3 Methodology .....	104
6.4 Results and discussion .....	108
6.4.1 Preferential paths through porous structures .....	108
6.4.2 Flow with clogging .....	111
6.5 Conclusions .....	114
<b>Chapter 7: Final remarks .....</b>	<b>115</b>
7.1 Work contributions .....	115
7.2 Future works .....	116
<b>References .....</b>	<b>117</b>
<b>Appendix A: Perturbation theory .....</b>	<b>131</b>
<b>Appendix B: Moments and isotropy in LBM .....</b>	<b>134</b>

# List of Figures

Figure 1: Lattice structure of D2Q9 model. The lattice nodes (circles) are numbered from zero to eight, which identifies each direction, i.e.,  $i = 0, 1, \dots, 8$ . ..... 7

Figure 2: Illustration of the streaming process for D2Q9 model. The circles are the fluid nodes. The solid arrows (—) are the distribution functions known in the current step ( $t$ ) after the collisions, and the dashed arrows (--) are the unknown distribution functions in the next step ( $t + \delta t$ ). Hence, the unknown distribution function in direction  $i$  at the resting node is  $f_i(t + \delta t) = f_{post_i}(t)$ . ..... 9

Figure 3: Difference between link-wise and wet-node approaches. The solid and fluid nodes are, respectively, the black and white nodes. The solid line (—) and the dashed line (--) are the computational boundary in the wet-node and link-wise approaches, respectively. .... 15

Figure 4: Example of the bounce-back scheme for D2Q9 model. The solid and fluid nodes are, respectively, the black and white nodes. The dashed line (--) is the computational boundary in the link-wise approach. The solid and dashed arrows are, respectively, the known distribution functions in the step  $t$  and the unknown distribution functions in the step  $t + \delta t$ . 15

Figure 5: Bounce-back scheme in concave corners for D2Q9 model. The solid, fluid and corner nodes are, respectively, the black, white, and red nodes. The solid arrows (—) are the distribution functions known from streaming ( $f_0, f_3, f_4$ , and  $f_7$ ) or calculated from the bounce-back scheme ( $f_1, f_2$ , and  $f_5$ ). The dashed arrows (--) are the unknown distribution functions. .... 17

Figure 6: An example of a D2Q9 domain with open boundaries where the periodic conditions can be applied. The solid and fluid nodes are, respectively, the black and white nodes. The solid arrows (—) are the distribution functions known from streaming, and the dashed arrows (--) are the distribution functions calculated implementing periodic conditions. .... 18

Figure 7: General diagram for an LBM code. Sections 2.3 to 2.5 cover the implementations of  $\Omega_i(f_i)$ ,  $F_i$  and boundary conditions. .... 57

Figure 8: Illustrative sketch of the Couette flow benchmark, where the blue region and the arrows represent, respectively, the fluid and the velocity profile. .... 58

Figure 9: Domain representation for the Couette flow problem considered when  $N_y = 4$ . The solid, fluid and ignored nodes are, respectively, the black, white and dashed nodes. The dashed lines (--) are the computational boundary in the link-wise approach. .... 60

Figure 10: Initialization of the probability distribution function employing the equilibrium scheme, in which  $cu \equiv \vec{c}_i \cdot \vec{u}$ ,  $U2 \equiv \vec{u} \cdot \vec{u}$ ,  $feq \equiv f_i^{eq}$ , and  $w \equiv \omega_i$ . The discrete velocities  $cx[\text{direction}]$  and  $cy[\text{direction}]$  are found in Equation (2.14). .... 62

Figure 11: BGK collision step, in which  $cu \equiv \vec{c}_i \cdot \vec{u}$ ,  $U2 \equiv \vec{u} \cdot \vec{u}$ ,  $feq \equiv f_i^{eq}$ ,  $w \equiv \omega_i$ , and  $\omega \equiv 1/\tau$ . The discrete velocities  $cx[\text{direction}]$  and  $cy[\text{direction}]$  are found in Equation (2.14). .... 63

Figure 12: Streaming step calculation. The discrete velocities  $cx[\text{direction}]$  and  $cy[\text{direction}]$  are found in Equation (2.14). .... 64

Figure 13: Macroscopic quantities calculation through Equations (2.22) and (2.23). The discrete velocities  $cx[\text{direction}]$  and  $cy[\text{direction}]$  are already considered for  $\delta x = 1$  and  $\delta t = 1$ . .... 65

Figure 14: Normalized velocity profile of the Couette flow for  $|\vec{u}_w| = 0.067$  l.u. ( $\tau = 0.6$ ) and  $|\vec{u}_w| = 0.333$  l.u. ( $\tau = 1.0$ ). In both cases,  $Ma = |\vec{u}_w|/c_s < 0.3$ , which ensures accuracy..... 66

Figure 15: Illustrative sketch of (a) the square-cavity flow benchmark, and (b) LBM domain when  $N_y = 9$ . The blue region represents the fluid. The solid, fluid, corner, and ignored nodes are, respectively, the black, white, red, and dashed nodes. The dashed lines are (a) the central axes of the domain, and (b) the computational boundary for the link-wise approach. .... 68

Figure 16: Corrections of the corner nodes distribution functions in the streaming step, through which Equation (2.47) is incorporated. .... 69

Figure 17: Normalized velocities ( $Re = 400$ ) over the central axes varying the relaxation time ( $\tau = 0.6$  and  $\tau = 0.8$ ) and the number of nodes ( $N = 101$  and  $N = 257$ ), which leads to  $|\vec{u}_w| = 0.052$  l.u. ( $\tau = 0.6$  and  $N = 257$ ),  $|\vec{u}_w| = 0.157$  l.u. ( $\tau = 0.8$ ), and  $|\vec{u}_w| = 0.135$  l.u. ( $\tau = 0.6$  and  $N = 101$ ). .... 70

Figure 18: Normalized velocities ( $Re = 5000$ ) over the central axes for  $\tau = 0.55$  and  $N = 501$ , which leads to  $|\vec{u}_w| = 0.167$  l.u. .... 70

Figure 19: Comparison of the Maxwell coexistence curve with the LB interaction models coexistence curves. .... 85

Figure 20: Relative errors of the LBM densities in the (a) vapor and (b) liquid phases. The Maxwell construction densities were considered as a benchmark to calculate the errors. Lines are plotted to help guide the eye. .... 85

Figure 21: Maximum spurious velocities versus reduced temperature for the interaction models considered. Lines are plotted to help guide the eye. .... 86

Figure 22: Location of the spurious velocities in the domain for (a) Shan-Chen model, (b)  $\beta$ -scheme and Yang-He models, and (c) Kupershtokh et al. model. .... 87

Figure 23: Interface thickness changes with reduced temperature for the interaction models considered. Lines are plotted to help guide the eye. .... 88

Figure 24: Polynomial fitting of the parameter values. Solid line (—):  $A(T_r) = 0.870 T_r^2 - 1.118 T_r + 0.174$ . Dashed line (---):  $\beta(T_r) = -0.870 T_r^2 + 1.118 T_r + 0.826$ . .... 89

Figure 25: Comparison between the density relative errors using Kupershtokh et al. model in the (a) vapor and (b) liquid phases. The Maxwell construction densities were considered as a benchmark to calculate the errors. Lines are plotted to help guide the eye. .... 90

Figure 26: Changes in (a) maximum spurious velocities and (b) interface thickness with the reduced temperature for the Kupershtokh et al. model. The lines are plotted to help guide the eye. .... 90

Figure 27: Young-Laplace test for the interaction models considered at  $T_r = [0.50, 0.70, 0.90]$ . Lines are the linear fit of the points. .... 93

Figure 28: Time evolutions of the elliptic radius for  $\theta = 0$  at (a)  $T_r = 0.90$ , (b)  $T_r = 0.70$ , and (c)  $T_r = 0.50$ . The points were collected at each 200 time steps. We accepted  $\dot{\varepsilon}_n(0) = 0$  to achieve the analytical solution. .... 94

Figure 29: Comparison between the analytical and the simulated initial periods. The lines are plotted to help guide the eye. .... 95

Figure 30: Velocity maps outside (cases (a), (b) and (c)) and inside (cases (d), (e) and (f)) the droplet for  $T_r = 0.50$  at  $t/T_{p,0} = [0.23, 0.52, 0.80]$ . .... 96

Figure 31: Simulated domain with artificial porous media. White and black areas represent, respectively, fluid and grain regions, while  $L_{PM}$  is the length of the porous medium. .... 105

Figure 32: Simulated velocity field for varied heights of water column: (a) 2 m, (b) 8 m, (c) 14 m and (d) 20 m. .... 106

Figure 33: Identification of the nodes, inlets and outlets in the considered porous media. 106

Figure 34: Linear regression of the calculated points (circles) with the linearized Forchheimer equation (dashed line):  $\frac{1}{K_{app}} = (0.72|\vec{u}| + 1.37)10^{10}$  with  $R^2 = 0.998$ . .... 109

Figure 35: Velocity field of the flow simulation for  $H = 10$  m in the original porous media. .... 110

Figure 36: Flow simulation through a rectangular pore with a triangle with length  $L$  in the center. The sketch is presented in (a), where the solid (—) and dashed (---) lines are the shortest paths passing under and above the triangle, respectively. The flow is presented in (b), where the white rectangles specify the two regions that have the same area. .... 111

Figure 37: Velocity field of the flow simulation with  $H = 10\text{ m}$  and the outlets (a) A and (b) E closed. .... 112

Figure 38: Velocity field of the flow simulation with  $H = 10\text{ m}$  and the nodes (a) 4, (b) 5, (c) 32, (d) 51 and (e) 58 closed. .... 113

Figure A.1: The logarithmic plot compares the analytical first roots of the quadratic equation with the ones from perturbation theory. .... 133

# List of Symbols

$a$	Carnahan-Starling with van der Waals attractive term parameter
$A$	Kupershtokh <i>et al.</i> parameter
$\vec{a}_c$	Acceleration related to an external force $\vec{F}$
$A^{eq}$	Parameter to calculate the equilibrium velocity
$A^{Li}$	Parameter to calculate the modified velocity in Liu <i>et al.</i> forcing scheme
$A_w$	Wetted surface
$b$	Carnahan-Starling parameter
$b(x, y)$	Boolean variable
$B_e$	Parameter in Liu <i>et al.</i> general forcing scheme
$C$	Constant related to the chosen permeability model
$C_e$	Parameter in Liu <i>et al.</i> general forcing scheme
$C_f$	Conversion factor
$\vec{c}_i$	Discrete lattice velocity
$c_s$	Sound speed
$\vec{dA}$	Infinitesimal area element vector
$\vec{dF}$	Infinitesimal force through $\vec{dA}$
$E$	Total energy density
$f$	Density distribution function
$\vec{F}$	External force
$\vec{F}_b$	Body force per unit of volume
$f^{eq}$	Equilibrium distribution function
$F_i$	Forcing term in the LBE
$\mathbf{F}_i$	Forcing matrix in the LBE for MRT model

$F_x$	Horizontal component of the external force
$\vec{F}^K$	Kupershtokh <i>et al.</i> interaction force
$f^{neq}$	Non-equilibrium distribution function
$f_{post}$	Post-collision distribution function
$\vec{F}^{SC}$	Shan-Chen interaction force
$F_x$	Horizontal component of the external force
$F_y$	Vertical component of the external force
$\vec{F}^{YH}$	Yang-He interaction force
$\vec{F}^{ZC}$	Zhang-Chen interaction force
$\vec{F}^\beta$	$\beta$ -scheme interaction force
$\vec{g}$	Gravitational acceleration
$G$	Interaction strength in the pseudopotential model
$G_{flow}$	Flow resistance
$h$	Height between the walls
$H$	Water column height
$i$	Lattice direction
$i$	Unit imaginary number
$\bar{i}$	Opposite direction of $i$
$\mathbf{I}$	Identity tensor
$j$	Counter in Taylor's series
$k$	Order in the Chapman-Enskog expansion
$K$	Permeability
$K_{app}$	Apparent permeability
$L$	Linear distance from inlet to outlet
$l_c$	Characteristic length

$L_e$	Sinuous length through the porous structures
$L_{PM}$	Porous media length
$m_j$	Moment in the MRT model
$m_j^{eq}$	Equilibrium moment in the MRT model
$m_{post_j}$	Post-collision moment in the MRT model
$M$	Mass experiencing the momentum $\vec{p}$
$\mathbf{M}$	Transformation matrix in the MRT model
$Ma$	Mach number
$n$	Mode of oscillation
$N$	Total number of nodes in the domain
$N_x$	Total number of lattice nodes in $x$ direction
$N_y$	Total number of lattice nodes in $y$ direction
$p$	Pressure
$\vec{p}$	Momentum
$\mathbf{P}$	Pressure tensor
$p_0$	Saturation pressure
$p_c$	Critical pressure
$p_{EOS}$	Pressure from the equation of state
$\mathbf{P}^K$	Pressure tensor for Kupershtokh <i>et al.</i> model
$\mathbf{P}^{SC}$	Pressure tensor for the Shan-Chen model
$\mathbf{P}^\beta$	Pressure tensor for $\beta$ -scheme
$q$	A given variable in Taylor's series
$\mathbf{Q}$	Convenient definition in Equation (B.3)
$q_0$	Initial value of variable $q$
$r$	Variable used in the perturbation theory example

$R$	Universal gas constant
$\mathbf{R}$	Third-order moment
$R^2$	Correlation
$R_0$	Initialized radius of the droplet
$Re$	Reynolds number
$Re_K$	Permeability Reynolds number
$R_{el}$	Radius of the ellipse at a given angle and time
$R_{eq}$	Equilibrium radius of the elliptic droplet
$R_{max}$	Maximum radius of the ellipse
$R_{min}$	Minimum radius of the ellipse
$R_{sp}$	Radius of the spherical droplet
$s$	A given variable in Taylor's series
$\mathbf{S}$	Deviatoric stress tensor
$s_0$	Initial value of variable $s$
$t$	Time
$t_1$	Time related to fast phenomena
$t_2$	Time related to slow phenomena
$T$	Temperature
$T_c$	Critical temperature
$T_{p,0}$	Initial oscillation period
$T_r$	Reduced temperature
$\vec{u}$	Macroscopic velocity in LBM
$U$	Zhang-Chen potential
$\vec{u}^{eq}$	Equilibrium velocity
$\vec{u}_{Li}$	Modified velocity in Liu <i>et al.</i> general forcing scheme

$u_{max}$	Maximum spurious velocity
$\vec{u}_w$	Macroscopic velocity of the wall in LBM
$u_x$	Horizontal component of the macroscopic velocity
$\vec{u}_{xnode}$	Axial lattice velocity at a node
$u_y$	Vertical component the macroscopic velocity
$v$	Molar volume
$\vec{v}$	Particle velocity
$v_r$	Reduced volume
$V_b$	Bulk volume of the porous media
$V_{flow}$	The volume that cooperates with the flow
$V_v$	Void volume
$w$	Static weight
$W$	Interface thickness
$w^K$	Static weight with the dimensions of Kupershtokh <i>et al.</i> model
$w^\beta$	Static weight with the dimensions of $\beta$ -scheme
$x$	Position variable for the horizontal direction
$\vec{x}$	Position vector
$x_c$	Center of the lattice domain in the horizontal direction
$x_0$	Position of the resting node in the horizontal direction
$y$	Position variable for the vertical direction
$y_c$	Center of the lattice domain in the vertical direction
$y_i$	Initial node when employing periodic condition
$y_0$	Position of the resting node in the vertical direction
$z$	Final value of the counter in Taylor's series
$\beta$	$\beta$ -scheme parameter

$\beta_F$	Empirical constant in the Forchheimer equation
$\gamma_s$	Surface tension
$\delta$	Kronecker delta
$\delta p$	Pressure drop
$\delta q$	Variation of variable $q$
$\delta s$	Variation of variable $s$
$\delta t$	Time variation
$\delta x$	Space variation
$\delta \rho$	Density variation
$\Delta'_n$	Damping regime discriminant
$\varepsilon$	Yang-He parameter
$\varepsilon_n$	A function of time to calculate the radius of an oscillating droplet
$\varepsilon_{n,max}$	Maximum value of $\varepsilon_n$
$\dot{\varepsilon}_n$	Time derivative of $\varepsilon_n$
$\epsilon$	Small parameter in the perturbation theory
$\zeta_n$	Initial value of the cosine argument to calculate $\varepsilon_n$
$\eta$	Carnahan-Starling variable
$\theta$	Angle with the horizontal axis
$\kappa$	Dilatational viscosity
$\lambda_n$	An expression that includes the oscillating mode of a droplet and some physical properties
$\Lambda$	Relaxation matrix in the MRT model
$\mu$	Shear viscosity
$\mu_l$	Shear viscosity in the liquid phase
$\nu$	Kinematic viscosity
$\pi$	Second-order moment

$\rho$	Macroscopic density
$\bar{\rho}$	Average density
$\rho_c$	Critical density
$\rho_l$	Liquid density
$\rho_v$	Vapor density
$\rho_w$	Fluid density near the solid wall
$\tau$	Relaxation time
$\tau_e$	Relaxation time related to the dilatational viscosity
$\tau_j$	Relaxation time for momentum
$\tau_q$	Free parameter in the MRT model
$\tau_{tort}$	Tortuosity
$\tau_\epsilon$	Free parameter in the MRT model
$\tau_v$	Relaxation time related to the shear viscosity
$\tau_\rho$	Relaxation time for density
$\Upsilon$	Unified parameter
$\phi$	Kupershtokh <i>et al.</i> potential
$\phi_o$	Overall porosity
$\phi_e$	Effective porosity
$\chi$	Convenient definition in Equation (3.126)
$\chi'$	Convenient definition in Equation (3.167)
$\psi$	Pseudopotential
$\omega$	Weight specified to each different lattice
$\omega_{n,0}$	Initial oscillation frequency
$\Omega$	Collision operator

# List of Acronyms

ALE	Arbitrary Lagrangian-Eulerian, p. 1
BGK	Bhatnagar-Gross-Krook, p. 10
BTE	Boltzmann Transport Equation, p. 5
CFD	Computational Fluid Dynamics, p. 1
CPA	Cubic-Plus-Association equation of state, p. 76
CSvdW	Carnahan-Starling & van der Waals, p. 83
DdQq	Lattice Boltzmann model with d spatial dimensions and q discrete velocities domain, p. 7
D2Q9	Lattice Boltzmann model with nine discrete velocities in a bidimensional domain, p. 7
EDM	Exact Difference Method, p. 21
EOR	Enhanced Oil Recovery, p. 1
EOS	Equation of State, p. 19
LB	Lattice Boltzmann, p. 1
LBE	Lattice Boltzmann Equation, p. 7
LBM	Lattice Boltzmann Method, p. 1
MRT	Multiple-Relaxation-Time, p. 10
REV	Representative Element Volume, p. 100
RHS	Right-Hand Side, p. 4
SAFT	Statistical Associated-Fluid Theory, p. 116
SRT	Single-Relaxation-Time, p. 11
VOF	Volume of Fluid, p. 1

# Chapter 1

## Introduction

### 1.1 Motivation

The Lattice Boltzmann Method (LBM) has evolved from the Lattice Gas Automata model [1, 2]. The method is an attractive, mesoscopic approach for simulating numerous problems, such as bubble dynamics, fluid flows in complex geometries, and reactive flows with coupled transport phenomena [3, 4]. To correctly simulate these phenomena, the equations must ensure reasonable interactions among fluid-fluid and fluid-solid phases, and satisfy mass, momentum, and energy balances.

Arguably, the main feature of LBM is its straightforward computational implementation, effortless description of interfacial systems, and feasible insertion of capillary effects and other thermodynamic phenomena. For instance, while traditional Computational Fluid Dynamics (CFD) methods (e.g., Volume of Fluid (VOF) and Arbitrary Lagrangian-Eulerian (ALE)) are interface-tracking methods [5, 6, 7], the interface width and location arise naturally in LBM from the density profile, without tracking or reconstruction [8, 9, 10]. Even though, the no-slip boundary condition is still easily extended to complex geometries [4, 11].

Hence, several LBM applications have been advancing in the industry [3, 12], especially in chemical processes. The multiphase flow problems, commonly associated with separation processes and operations in the oil industry, e.g., emulsions and enhanced oil recovery (EOR), are engaging LBM applications [13, 14]. Most studies focus on analyzing the dynamic behavior of the fluid and ensuring recovery of the conservation equations (i.e., mass, momentum, and energy). The availability of the Lattice Boltzmann (LB) multiphase and multicomponent models turns the method suitable for simulating such types of flow.

The ubiquitous approach for multiphase and multicomponent modeling in LBM is the pseudopotential method, a bottom-up model, initially proposed by Shan and Chen in 1993 [15], that mimics particle interactions and performs phase transitions. Besides being a promising candidate for multiphase problems, LBM is also suitable for modeling porous media flows [11, 16, 17]. One branch of study is the preferential flow, an elusive phenomenon in porous media that impacts the oil industry, micro- and nanofluidic applications, and soil sciences. Notably, LBM with the Pore-Scale approach deals with complex geometries [3], accounts for mesoscopic properties that are hardly considered using macroscopic methods [18], details velocity fields, and identifies preferred pathways. Since preferential flow has several causes, it is hard to distinguish and evaluate the diverse contributions to the phenomenon. However, a starting simplification assumes that geometrical features are its primary cause, like in the Ju *et al.* model [19], a tortuosity-dependent resistance model.

## 1.2 Objectives

The primary objectives of this dissertation are to gain theoretical knowledge about LBM and practical experience with its computational implementation for future applications in multiphase flows in porous media. To achieve these objectives, this dissertation can be divided into three independent parts: (i) the deduction of the transport equations, (ii) the unified multiphase model proposal, and (iii) the LBM performance in porous media flow.

First, we deduce the transport equations in detail by employing the asymptotic analysis in the Boltzmann equation. This derivation enhances our confidence in algebraic manipulations for future LB deductions and provides a clear and didactic procedure to derive the transport equations, which is an information gap in the literature.

In the second part, we investigate the pseudopotential model. Several multiphase interaction models have been proposed in the literature, based on the same bottom-up concept, to reduce intrinsic limitations of the original Shan-Chen model. However, these interaction models are widespread in the literature under various names. Some of them are commonly presented as unique formulations that seem to yield similar results. Here, we propose a unified pseudopotential model, which recovers five previous multiphase models

depending on a tuned parameter. Combining the interaction models in simpler mathematical form makes later work more concise and quickly directs the reader to a unified parameter.

In the third part, parallel to developing the unified model for future multiphase simulations, we also study a porous media flow problem. We perform non-Darcy flow simulations with complex geometry to check the recovery of the Forchheimer equation and the prediction of the preferred path according to the Ju *et al.* model.

We aim to investigate the pseudopotential model and test a simple implementation of porous media independently. More specifically, in this dissertation, we intend to:

- clarify the theoretical details for the recovery of the continuity and the Navier-Stokes equations from LBM;
- investigate the correlation among different pseudopotential models;
- establish a proper region in the coexistence curve to tune the pseudopotential parameter;
- compare the limitations (thermodynamic consistency, density ratio, spurious velocity, and interface thickness) of the pseudopotential models and suggest an alternative way to decrease them;
- carry out simulations in complex geometries;
- verify if LBM recovers the Forchheimer model for a porous media flow;
- explore Ju *et al.* resistance model to search for preferential paths.

### 1.3 Document structure

Initially, Chapter 2 addresses the main aspects of the LBM theory to understanding the following sections, such as the general mathematical formalism, boundary conditions, and forcing schemes. Then, in Chapter 3, we thoroughly prove that LBM recovers the transport equations. Next, in Chapter 4, we implement two frequent benchmarks to demonstrate the theory and validate our implementation. In Chapter 5, we develop and test the unified model for multiphase interactions. Chapter 6 displays the results from a parallel investigation in which we demonstrate the LBM applicability to porous media simulations by performing a preferential flow study. Lastly, Chapter 7 concludes with a summary of the central ideas presented in this dissertation.

# Chapter 2

## Theoretical background

In this chapter, we present an LBM overview. Interested readers, however, are referred to Guo and Shu [20] and Kruger *et al.* [21] for additional theoretical details. We must clarify here that throughout the text we use an arrow to indicate vectors (e.g.,  $\vec{v}$ ) and bold notation to indicate tensors (e.g.,  $\mathbf{S}$ ), regardless of the tensor order. Throughout the chapter we will also often use the Einstein summation convention (index notation).

### 2.1 Boltzmann Transport Equation

LBM uses the density distribution function  $f(\vec{x}, \vec{v}, t)$  to track the distribution of particles in the system. This function describes the probability of finding a particle with velocity  $\vec{v}$  (associated with a momentum  $\vec{p}$ ) in a position  $\vec{x}$  at time  $t$ . The total derivative of  $f(\vec{x}, \vec{v}, t)$  in the physical space is [22]:

$$\frac{df}{dt} = \frac{\partial f}{\partial x_\alpha} \frac{dx_\alpha}{dt} + \frac{\partial f}{\partial v_\alpha} \frac{dv_\alpha}{dt} + \frac{\partial f}{\partial t} \frac{dt}{dt} . \quad (2.1)$$

Since  $v_\alpha \equiv dx_\alpha/dt$ ,  $dt/dt = 1$ , and  $p_\alpha \equiv M v_\alpha$ , where  $M$  is the mass experiencing the momentum  $p_\alpha$ , the right-hand side (RHS) of Equation (2.1) is rewritten as:

$$\frac{df}{dt} = v_\alpha \frac{\partial f}{\partial x_\alpha} + \frac{\partial f}{\partial p_\alpha} \frac{\partial p_\alpha}{\partial v_\alpha} \frac{dv_\alpha}{dt} + \frac{\partial f}{\partial t} . \quad (2.2)$$

From the definition of  $p_\alpha$ , we know that  $\partial p_\alpha / \partial v_\alpha = M$ . Also,  $dv_\alpha/dt \equiv a_{c\alpha}$ , where  $\vec{a}_c$  is the acceleration. Then,

$$\frac{df}{dt} = v_\alpha \frac{\partial f}{\partial x_\alpha} + M a_{c\alpha} \frac{\partial f}{\partial p_\alpha} + \frac{\partial f}{\partial t} . \quad (2.3)$$

Recalling that  $F_\alpha \equiv M a_{c\alpha}$ , where  $\vec{F}$  is an external force,

$$\frac{df}{dt} = v_\alpha \frac{\partial f}{\partial x_\alpha} + F_\alpha \frac{\partial f}{\partial p_\alpha} + \frac{\partial f}{\partial t} . \quad (2.4)$$

Defining the collision operator as  $\Omega \equiv df/dt$  and returning to the direct tensor notation:

$$[\vec{v} \cdot \vec{\nabla}_x + \vec{F} \cdot \vec{\nabla}_p + \partial_t] f(\vec{x}, \vec{v}, t) = \Omega(f) , \quad (2.5)$$

where,  $\vec{\nabla}_x$ ,  $\vec{\nabla}_p$ , and  $\partial_t$  are the short notations for  $\partial/\partial x_\alpha$ ,  $\partial/\partial p_\alpha$  and  $\partial/\partial t$ . Equation (2.5) is the Boltzmann Transport Equation (BTE), which governs the advection dynamics of the density distribution function of particles in the presence of an external force (e.g., gravity) [21]. The collision operator describes the complex dynamical interactions during particle collisions. Later, Section 2.3 presents two relevant collision models in LBM.

Once  $f(\vec{x}, \vec{v}, t)$  is calculated, the macroscopic quantities can be obtained from moments of the distribution in the velocity space:

$$\rho = \int f(\vec{x}, \vec{v}, t) d\vec{v} , \quad (2.6)$$

$$\rho \vec{u} = \int \vec{v} f(\vec{x}, \vec{v}, t) d\vec{v} , \quad (2.7)$$

$$\rho E = \frac{1}{2} \int |\vec{v}|^2 f(\vec{x}, \vec{v}, t) d\vec{v} , \quad (2.8)$$

where  $\rho$ ,  $\vec{u}$ , and  $E$  are respectively the macroscopic density, velocity, and total energy.

To assure the LBM can reproduce correctly the transport phenomena, one is interested in recovering the hydrodynamic equations of the continuum theory, such as the continuity equation,

$$\partial_t \rho + \vec{\nabla} \cdot \rho \vec{u} = 0 , \quad (2.9)$$

which expresses the mass conservation in the conservative form [23, 24], and the motion equation,

$$\partial_t \rho \vec{u} = -\vec{\nabla} \cdot \rho \vec{u} \vec{u} - \vec{\nabla} p - \vec{\nabla} \cdot \mathbf{S} + \vec{F}_b , \quad (2.10)$$

which guarantees the momentum conservation in the Eulerian specification [23, 24]. In Equation (2.10),  $p$  is the pressure,  $\mathbf{S}$  is the deviatoric stress tensor and  $\vec{F}_b$  is a body force (e.g., gravity or electric forces) per unit of volume.

The Chapman-Enskog expansion is a typical methodology to recover these equations [25, 26, 27]. It is a perturbation expansion of  $f(\vec{x}, \vec{v}, t)$  around its equilibrium value  $f^{eq}$ . The small parameter used in this asymptotic analysis is related to the Knudsen number, which is a ratio between the molecular mean free path and a characteristic length of the flow. The reader can find the foundation of the perturbation expansion in Appendix A, and the Chapman-Enskog analysis is detailed Chapter 3, where LBM recovers both Equations (2.9) and (2.10). Appendix B details the moments required for such derivations, like the moments in Equations (2.6) to (2.8).

## 2.2 Lattice Boltzmann Method

The solution of the BTE is cumbersome since it is a non-linear partial integrodifferential equation [28]. The computational time could be affected depending on the numerical treatment. For instance,  $f(\vec{x}, \vec{v}, t)$  depends on five (in a bidimensional domain:  $x_\alpha, x_\beta, v_\alpha, v_\beta$ , and  $t$ ) or seven physical continuous variables (in a three-dimensional domain:

$x_\alpha, x_\beta, x_\gamma, v_\alpha, v_\beta, v_\gamma$ , and  $t$ ). One can simplify the continuous dependence by performing the discretization of the space and velocity. As a result, the LBM emerges as a numerical method to solve the BTE, in which space, time, and velocity ( $\vec{c}_i$ ) are now discretized. The outcome is a discrete distribution function  $f_i = f_i(\vec{x}, \vec{c}_i, t)$ , where  $\vec{x}$ ,  $\vec{c}_i$ , and  $t$  are given in lattice units rather than physical units.

The fully discrete form of BTE is the Lattice Boltzmann Equation (LBE),

$$f_i(\vec{x} + \vec{c}_i \delta t, t + \delta t) - f_i(\vec{x}, t) = [\Omega_i(f_i) + F_i] \delta t, \quad (2.11)$$

which is applied to each direction  $i$  in the lattice node.

Depending on the extent of physical consistency and time-cost one may provide for the simulations, different lattice arrangements arise. They are often gathered in the DdQq model, in which  $d$  is the dimension (e.g.,  $d = 2$  for a bidimensional domain) and  $q$  is the number of discrete velocities [29]. D1Q3, D2Q7, D2Q9, D2Q25, D3Q19, and D3Q27 models are some examples. The most common model for bidimensional domains is the D2Q9, displayed in Figure 1.

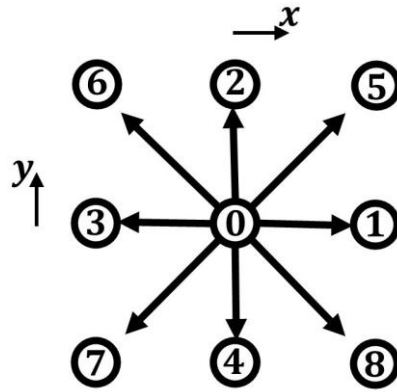


Figure 1: Lattice structure of D2Q9 model. The lattice nodes (circles) are numbered from zero to eight, which identifies each direction, i.e.,  $i = 0, 1, \dots, 8$ .

In the equilibrium, the distribution function is generally expressed by a Maxwell-Boltzmann distribution function, which, after discretization, is given by:

$$f_i^{eq}(\vec{x}, t) = \omega_i \rho \left[ 1 + \frac{\vec{c}_i \cdot \vec{u}^{eq}}{c_s^2} + \frac{(\vec{c}_i \cdot \vec{u}^{eq})^2}{2c_s^4} - \frac{(\vec{u}^{eq})^2}{2c_s^2} \right], \quad (2.12)$$

where  $\vec{u}^{eq}$  is the equilibrium velocity,  $c_s$  is the speed of sound and  $\omega_i$  are the weights. In the absence of external forces, the equilibrium velocity is the same as the real fluid velocity, i.e.,  $\vec{u}^{eq}(\vec{x}) = \vec{u}(\vec{x})$ . On the other hand, Section 2.5 reveals how to calculate  $\vec{u}^{eq}$  when considering external force. Also, Appendix B demonstrates the mandatory isotropy conditions, independent of the orthogonal transformations, to ensure that the transport equations are recovered and to calculate the weights for each different lattice model [20, 30]. For instance, the D2Q9 model fixes the speed of sound as  $c_s = (\delta x / \delta t) / \sqrt{3}$  and sets the weights and discrete velocities as:

$$\omega_i = \begin{cases} 4/9, & i = 0 \\ 1/9, & i = 1, 2, 3, 4 \\ 1/36, & i = 5, 6, 7, 8 \end{cases}, \quad (2.13)$$

$$\begin{aligned} & \left\{ \begin{pmatrix} c_{0x} \\ c_{0y} \end{pmatrix}, \dots, \begin{pmatrix} c_{8x} \\ c_{8y} \end{pmatrix} \right\} = \\ & = \left\{ \begin{pmatrix} 0 \\ 0 \end{pmatrix}, \begin{pmatrix} 1 \\ 0 \end{pmatrix}, \begin{pmatrix} 0 \\ 1 \end{pmatrix}, \begin{pmatrix} -1 \\ 0 \end{pmatrix}, \begin{pmatrix} 0 \\ -1 \end{pmatrix}, \begin{pmatrix} 1 \\ 1 \end{pmatrix}, \begin{pmatrix} -1 \\ 1 \end{pmatrix}, \begin{pmatrix} -1 \\ -1 \end{pmatrix}, \begin{pmatrix} 1 \\ -1 \end{pmatrix} \right\} \left( \frac{\delta x}{\delta t} \right). \end{aligned} \quad (2.14)$$

The LBM encloses two main steps: the collision and the streaming. In the collision step, the collision model is inserted (Section 2.3) in the LBE and further calculate the post-collision distribution function  $f_{post_i}(\vec{x}, t)$  for all fluid nodes of the lattice:

$$f_{post_i}(\vec{x}, t) = f_i(\vec{x}, t) + [\Omega_i(f_i) + F_i] \delta t. \quad (2.15)$$

The effects of the particle collisions propagate through the lattice. Hence, in the streaming step, the distribution functions  $f_i(\vec{x} + \vec{c}_i \delta t, t + \delta t)$  are calculated after the collisions, i.e., the post-collision distribution function of the resting node propagates to each neighboring node, as given by:

$$f_i(\vec{x} + \vec{c}_i \delta t, t + \delta t) = f_{post_i}(\vec{x}, t) . \quad (2.16)$$

Exemplifying the streaming step using the D2Q9 model and  $\delta t = 1$  for a resting node centered at  $(x_0, y_0)$ , as in the case of Figure 2, Equation (2.16) is rewritten nine times:

$$f_0(x_0, y_0, t + \delta t) = f_{post_0}(x_0, y_0, t) \quad (2.17)$$

$$f_1(x_0, y_0, t + \delta t) = f_{post_1}(x_0 - 1, y_0, t) \quad (2.18)$$

$$f_2(x_0, y_0, t + \delta t) = f_{post_2}(x_0, y_0 - 1, t) \quad (2.19)$$

(:)

$$f_7(x_0, y_0, t + \delta t) = f_{post_7}(x_0 + 1, y_0 + 1, t) \quad (2.20)$$

$$f_8(x_0, y_0, t + \delta t) = f_{post_8}(x_0 - 1, y_0 + 1, t) \quad (2.21)$$

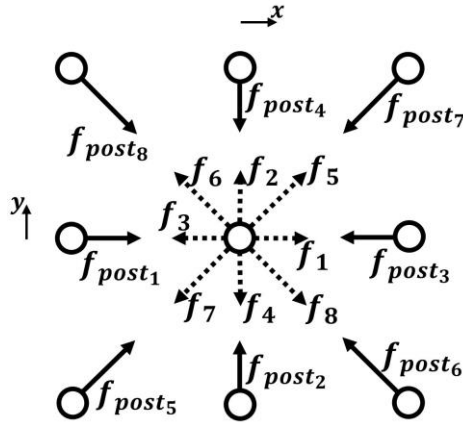


Figure 2: Illustration of the streaming process for D2Q9 model. The circles are the fluid nodes. The solid arrows (—) are the distribution functions known in the current step ( $t$ ) after the collisions, and the dashed arrows (---) are the unknown distribution functions in the next step ( $t + \delta t$ ). Hence, the unknown distribution function in direction  $i$  at the resting node is  $f_i(t + \delta t) = f_{post_i}(t)$ .

After the streaming, the macroscopic density and velocity are obtained similarly to Equations (2.6) and (2.7),

$$\rho = \sum_i f_i , \quad (2.22)$$

$$\vec{u}(\vec{x}) = \frac{1}{\rho} \sum_i f_i(\vec{x}, t) \vec{c}_i . \quad (2.23)$$

## 2.3 Collision models

The collision operator is a double integral in the velocity space [28]. Since its solution is not a simple task, collision models have been conceived through some simplifications [20], as the Bhatnagar-Gross-Krook (BGK) (Section 2.3.1) and the improved Multiple-Relaxation-Time (MRT) models (Section 2.3.2). Indeed, other robust collision schemes, such as the Cascaded [31, 32, 33], the Karlin-Bosch-Chikatamarala [34], and the entropic [35, 36] methods achieve stable and accurate results and reduce the Galilean invariance [3]. Regardless of the model chosen, the collision operator must conserve mass, momentum, and energy [28], which are mathematically expressed as,

$$\int \Omega(f) d\vec{v} = 0 , \quad (2.24)$$

$$\int \vec{v} \Omega(f) d\vec{v} = \vec{0} , \quad (2.25)$$

$$\int |\vec{v}|^2 \Omega(f) d\vec{v} = 0 . \quad (2.26)$$

Additionally, the collision model must be consistent with the Boltzmann  $\mathcal{H}$ -Theorem, which declares that a quantity  $\mathcal{H}$ , defined as,

$$\mathcal{H} = \int f \ln f d\vec{v} , \quad (2.27)$$

always decreases until it reaches the equilibrium ( $f = f^{eq}$ ) [37].

### 2.3.1 Bhatnagar-Gross-Krook model

The BGK model, proposed by Bhatnagar *et al.* in 1954 [38], presumes that the collision operator varies linearly with  $f_i$ ,

$$\Omega_i(f) = -\frac{1}{\tau}(f_i - f_i^{eq}) , \quad (2.28)$$

where the relaxation time  $\tau$  specifies how fast the system converges to equilibrium. Since BGK includes only one parameter ( $\tau$ ), the model is often named Single-Relaxation-Time (SRT).

Considering de BGK model, the LBE reads:

$$f_i(\vec{x} + \vec{c}_i \delta t, t + \delta t) - f_i(\vec{x}, t) = -\frac{1}{\tau}[f_i(\vec{x}, t) - f_i^{eq}(\vec{x}, t)]\delta t + F_i \delta t . \quad (2.29)$$

Because of this simplicity, BGK is broadly used in LBM literature; however, it yields a few artificial anomalies, such as viscosity-dependent results (e.g., Poiseuille flow, permeability, and wall location) [39]. This dependence arises because, as Chapter 3 demonstrates through the Chapman-Enskog expansion, the relaxation time is a connection between the mesoscopic approach and the continuum theory through its relation with the shear viscosity  $\mu$  of the fluid:

$$\mu = \rho c_s^2 \left( \tau - \frac{\delta t}{2} \right) . \quad (2.30)$$

Regarding Equation (2.30), one must set  $\tau > \delta t/2$  to avoid unphysical shear viscosities ( $\mu \leq 0$ ) and instabilities. In fact, the BGK provides limited stable simulations. For instance, the model requires many lattice nodes to reproduce stable turbulent problems, increasing computational time. Similarly, the modeling of viscous fluids demands higher  $\tau$ , raising the simulation fluid velocity and causing inaccuracy [3]. Other collision operators,

such as the MRT model presented in Section 2.3.2, are usually considered to attain more accurate and stable simulations.

### 2.3.2 Multiple-Relaxation-Time model

The BGK model establishes that all  $f_i$  relax together with the same  $\tau$  in the collision step of the population space. The MRT model proposed by d’Humières in 1992 [40] employs a set of different parameters instead to relax the moments  $m_j$  individually in the moment space.

The mapping of  $f_i$  from the population space to the moment space is conducted through a linear transformation as follows:

$$m_j = \sum_i M_{ji} f_i , \quad (2.31)$$

$$m_j^{eq} = \sum_i M_{ji} f_i^{eq} , \quad (2.32)$$

where  $m_j^{eq}$  is the equilibrium moment, and  $M_{ji}$  (or  $\mathbf{M}$ ) is the transformation matrix given by:

$$\mathbf{M} = \begin{bmatrix} 1 & 1 & 1 & 1 & 1 & 1 & 1 & 1 & 1 \\ -4 & -1 & -1 & -1 & -1 & 2 & 2 & 2 & 2 \\ 4 & -2 & -2 & -2 & -2 & 1 & 1 & 1 & 1 \\ 0 & 1 & 0 & -1 & 0 & 1 & -1 & -1 & 1 \\ 0 & -2 & 0 & 2 & 0 & 1 & -1 & -1 & 1 \\ 0 & 0 & 1 & 0 & -1 & 1 & 1 & -1 & -1 \\ 0 & 0 & -2 & 0 & 2 & 1 & 1 & -1 & -1 \\ 0 & 1 & -1 & 1 & -1 & 0 & 0 & 0 & 0 \\ 0 & 0 & 0 & 0 & 0 & 1 & -1 & 1 & -1 \end{bmatrix} . \quad (2.33)$$

The collisions are then executed in the moment space with the calculated moments,

$$m_{post_j} = m_j - \Lambda_{jj}(m_j - m_j^{eq})\delta t , \quad (2.34)$$

where  $m_{post_j}$  is the moment after the collision,  $\Lambda_{jj}$  (or  $\mathbf{\Lambda}$ ) is the diagonal relaxation matrix,

$$\mathbf{\Lambda} = \text{diag}(\tau_\rho^{-1}, \tau_e^{-1}, \tau_\epsilon^{-1}, \tau_j^{-1}, \tau_q^{-1}, \tau_j^{-1}, \tau_q^{-1}, \tau_v^{-1}, \tau_v^{-1}) , \quad (2.35)$$

and  $\tau_\rho$  and  $\tau_j$  are the relaxation times for the conserved moments (i.e., density and momentum),  $\tau_\epsilon$  and  $\tau_q$  are free parameters adjusted to keep the method stable,  $\tau_e$  is related to the dilatational viscosity (or bulk viscosity)  $\kappa$  and  $\tau_v$  is related to the shear viscosity  $\mu$ ,

$$\kappa = \rho c_s^2 \left( \tau_e - \frac{\delta t}{2} \right) - \frac{\mu}{3} , \quad (2.36)$$

$$\mu = \rho c_s^2 \left( \tau_v - \frac{\delta t}{2} \right) . \quad (2.37)$$

After the collision step, the moments are mapped back to the population space through:

$$f_{post_i} = \sum_j M_{ij}^{-1} m_{post_j} , \quad (2.38)$$

where  $M_{ij}^{-1}$  (or  $\mathbf{M}^{-1}$ ) is the inverse of  $\mathbf{M}$ , as displayed in Equation (2.39).

The matrices can be calculated either from Hermite (the moments are Hermite polynomials) or from Gram-Schmidt (orthogonal-based method) approaches [21]. Since the latter is predominant in LBM literature, Equations (2.33), (2.35), and (2.39) present the matrices from the Gram-Schmidt approach, which are adopted in this work. Accordingly, the insertion of the MRT model in the LBE originates Equation (2.40), which recovers Equation (2.29). This is possible because  $\mathbf{\Lambda} = \tau^{-1}\mathbf{I}$  and  $\mathbf{M}^{-1}\mathbf{M} = \mathbf{I}$ , where  $\mathbf{I}$  is the identity matrix, which is unable to modify the equations. Hence, the only difference between the BGK and MRT models is the collision step. The additional parameters in the moment space result in more accurate and stable simulations with the MRT model [3, 21].

$$\mathbf{M}^{-1} = \begin{bmatrix} \frac{1}{9} & -\frac{1}{9} & \frac{1}{9} & 0 & 0 & 0 & 0 & 0 & 0 \\ \frac{1}{9} & \frac{1}{36} & \frac{1}{18} & \frac{1}{6} & -\frac{1}{6} & 0 & 0 & \frac{1}{4} & 0 \\ \frac{1}{9} & -\frac{1}{36} & -\frac{1}{18} & 0 & 0 & \frac{1}{6} & -\frac{1}{6} & -\frac{1}{4} & 0 \\ \frac{1}{9} & \frac{1}{36} & \frac{1}{18} & -\frac{1}{6} & \frac{1}{6} & 0 & 0 & \frac{1}{4} & 0 \\ \frac{1}{9} & -\frac{1}{36} & -\frac{1}{18} & 0 & 0 & -\frac{1}{6} & \frac{1}{6} & -\frac{1}{4} & 0 \\ \frac{1}{9} & \frac{1}{18} & \frac{1}{36} & \frac{1}{6} & \frac{1}{12} & \frac{1}{6} & \frac{1}{12} & 0 & \frac{1}{4} \\ \frac{1}{9} & \frac{1}{18} & \frac{1}{36} & -\frac{1}{6} & -\frac{1}{12} & \frac{1}{6} & \frac{1}{12} & 0 & -\frac{1}{4} \\ \frac{1}{9} & \frac{1}{18} & \frac{1}{36} & -\frac{1}{6} & -\frac{1}{12} & -\frac{1}{6} & -\frac{1}{12} & 0 & \frac{1}{4} \\ \frac{1}{9} & \frac{1}{18} & \frac{1}{36} & \frac{1}{6} & \frac{1}{12} & -\frac{1}{6} & -\frac{1}{12} & 0 & -\frac{1}{4} \end{bmatrix}. \quad (2.39)$$

$$f_i(\vec{x} + \vec{c}_i \delta t, t + \delta t) - f_i(\vec{x}, t) = -\mathbf{M}^{-1} \mathbf{\Lambda} \mathbf{M} [f_i(\vec{x}, t) - f_i^{eq}(\vec{x}, t)] \delta t + F_i \delta t. \quad (2.40)$$

## 2.4 Boundary conditions

Two different approaches to model boundary conditions can be distinguished: the link-wise and the wet-node. In the latter, the lattice nodes constitute the computational boundary on their own, as shown in Figure 3. In the former, the computational boundary is located on the lattice links, i.e., the boundary lies between the fluid and solid nodes [21].

The link-wise approach is more attractive because it simultaneously yields high stability, exact mass conservation, and simplicity. Therefore, the link-wise description was chosen to model the boundary conditions in the simulations of this work. Consequently, this section only presents boundary conditions related to the link-wise, i.e., the bounce-back scheme and the periodic condition.

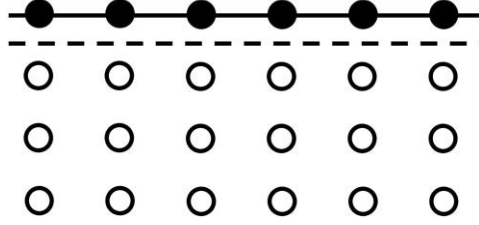


Figure 3: Difference between link-wise and wet-node approaches. The solid and fluid nodes are, respectively, the black and white nodes. The solid line (—) and the dashed line (---) are the computational boundary in the wet-node and link-wise approaches, respectively.

### 2.4.1 Bounce-back scheme

The bounce-back scheme is a systematic method employed to model solid boundaries in the link-wise approach. It brings the outstanding no-slip boundary condition to the mesoscopic procedure, establishing that the fluid velocity near the wall is the same as the wall velocity. Within this method, when a group of particles hits the boundary in a direction  $i$  with a known  $f_i$ , it will be reflected in the opposite direction  $\bar{i}$  but with the same value of  $f_i$ , as illustrated in Figure 4.

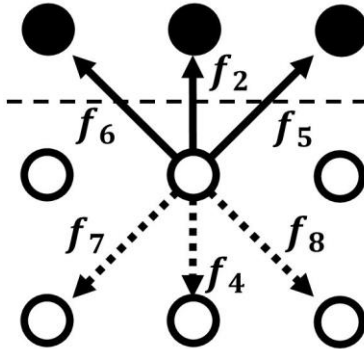


Figure 4: Example of the bounce-back scheme for D2Q9 model. The solid and fluid nodes are, respectively, the black and white nodes. The dashed line (---) is the computational boundary in the link-wise approach. The solid and dashed arrows are, respectively, the known distribution functions in the step  $t$  and the unknown distribution functions in the step  $t + \delta t$ .

The bounce-back scheme can be performed in two ways, using (i) the fullway bounce-back scheme [41], in which the population travels entirely from the fluid to the solid nodes, i.e., the known  $f_i(\vec{x}, t)$  are stored in the solid nodes in step  $t + \delta t$  and collect the values from them in step  $t + 2\delta t$ ; or (ii) the halfway bounce-back scheme [42], which the population

travels only the half distance between the fluid and solid nodes, i.e., the values of  $f_i(\vec{x}, t)$  are directly used to calculate  $f_i(\vec{x}, t + \delta t)$ , without storing them in the solid nodes. Therefore, when applying the fullway bounce-back scheme, the lattice demands more nodes (solid nodes), and there is a  $2\delta t$  time delay to the information get back to the original fluid node.

For Figure 4, the halfway bounce-back scheme is mathematically implemented as:

$$f_4(\vec{x}, t + \delta t) = f_2(\vec{x}, t) , \quad (2.41)$$

$$f_7(\vec{x}, t + \delta t) = f_5(\vec{x}, t) , \quad (2.42)$$

$$f_8(\vec{x}, t + \delta t) = f_6(\vec{x}, t) , \quad (2.43)$$

where  $f_2$ ,  $f_5$ , and  $f_6$  are the known distribution functions from the streaming in the step  $t$ , and  $f_4$ ,  $f_7$ , and  $f_8$  are the distribution functions that must be calculated in step  $t + \delta t$ .

The halfway bounce-back scheme for moving walls can be extended as,

$$f_i(\vec{x}, t + \delta t) = f_i(\vec{x}, t) - 2\omega_i\rho_w \frac{\vec{c}_i \cdot \vec{u}_w}{c_s^2} , \quad (2.44)$$

where  $\rho_w$  and  $\vec{u}_w$  are, respectively, the density and the macroscopic velocity of the wall. A usual simplification is to define  $\rho_w$  as the fluid density near the wall, i.e.,  $\rho_w = \rho(\vec{x}, t)$ .

For stationary walls ( $\vec{u}_w = \vec{0}$ ), the last term in Equation (2.44) vanishes and the standard halfway bounce-back scheme is recovered:

$$f_i(\vec{x}, t + \delta t) = f_i(\vec{x}, t) . \quad (2.45)$$

In this way, the bounce-back scheme ensures there is no mass flux either through resting or moving solid walls. A complication that may arise is the modeling of boundary conditions in concave corners, where it is impossible to determine two ( $f_6$  and  $f_8$ ) of the nine density distribution functions at the corner node [30], i.e., the red node in Figure 5. The reason is that the values of  $f_6$  and  $f_8$  cannot be obtained from the streaming step, since the neighbors where they must originate are solid nodes.

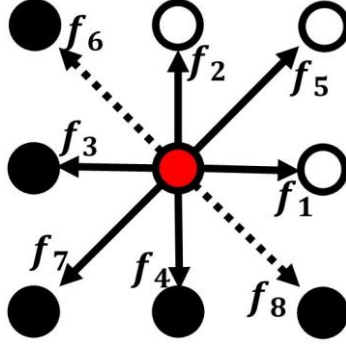


Figure 5: Bounce-back scheme in concave corners for D2Q9 model. The solid, fluid and corner nodes are, respectively, the black, white, and red nodes. The solid arrows (—) are the distribution functions known from streaming ( $f_0, f_3, f_4,$  and  $f_7$ ) or calculated from the bounce-back scheme ( $f_1, f_2,$  and  $f_5$ ). The dashed arrows (- -) are the unknown distribution functions.

Ignoring this situation can lead to unstable simulations. Hence, a typical solution is to set the central corner node density as the average density of the system. This adjustment reduces the degrees of freedom, making it possible to calculate  $f_6$  and  $f_8$ . From Equation (2.22) [43],

$$\rho = f_6 + f_8 + \sum_{\substack{i \neq 6 \\ i \neq 8}} f_i . \quad (2.46)$$

Note that  $f_6$  and  $f_8$  are enclosed in the corner node, which means that their information does not stream over the lattice. Then, imposing  $f_6 = f_8$  in Equation (2.46), the remainder  $f_i$  is calculated through:

$$f_6 = f_8 = \frac{1}{2} \left( \rho - \sum_{\substack{i \neq 6 \\ i \neq 8}} f_i \right) . \quad (2.47)$$

## 2.4.2 Periodic condition

A periodic condition in open boundaries (Figure 6) is introduced when one intends to make the outflow enter the opposite side. This condition implies that the zeroth and first order moments at the outlet ( $x = L$ ) are equal to those at the inlet ( $x = 0$ ),

$$\rho(x = 0, y, t) = \rho(x = L, y, t) , \quad (2.48)$$

$$\rho(x = 0, y, t)\vec{u}(x = 0, y, t) = \rho(x = L, y, t)\vec{u}(x = L, y, t) . \quad (2.49)$$

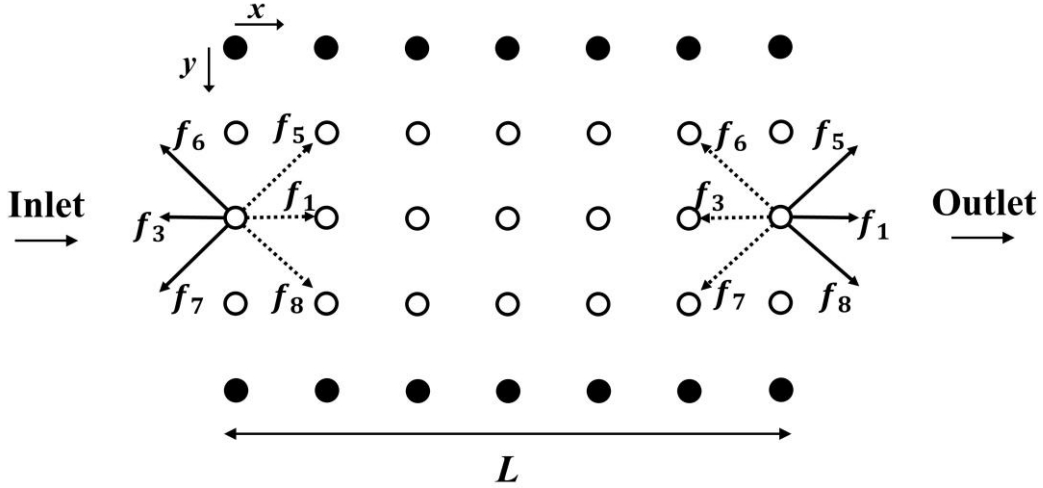


Figure 6: An example of a D2Q9 domain with open boundaries where the periodic conditions can be applied. The solid and fluid nodes are, respectively, the black and white nodes. The solid arrows (—) are the distribution functions known from streaming, and the dashed arrows (---) are the distribution functions calculated implementing periodic conditions.

In other words, the known density distribution functions leaving the domain, both at the inlet and outlet, stream to the opposite side. Exemplifying for D2Q9 model,

$$f_i(x = 0, y, t + \delta t) = f_{post_i}(x = L, y_i, t) , \text{ for } i = 1, 5 \text{ and } 8, \quad (2.50)$$

$$f_i(x = L, y, t + \delta t) = f_{post_i}(x = 0, y_i, t) , \text{ for } i = 3, 6 \text{ and } 7, \quad (2.51)$$

where  $y_i = y + |\vec{c}_i|_y \delta t$ , and  $|\vec{c}_i|_y$  is the magnitude of  $\vec{c}_i$  in the  $y$  direction.

In this way, the periodic condition in Figure 6 is written as:

$$f_1(x = 0, y, t + \delta t) = f_{post_1}(x = L, y, t) , \quad (2.52)$$

$$f_5(x = 0, y, t + \delta t) = f_{post_5}(x = L, y + 1, t) , \quad (2.53)$$

$$f_8(x = 0, y, t + \delta t) = f_{post_8}(x = L, y - 1, t) , \quad (2.54)$$

$$f_3(x = L, y, t + \delta t) = f_{post_3}(x = 0, y, t) , \quad (2.55)$$

$$f_6(x = L, y, t + \delta t) = f_{post_6}(x = 0, y + 1, t) , \quad (2.56)$$

$$f_7(x = L, y, t + \delta t) = f_{post_7}(x = 0, y - 1, t) . \quad (2.57)$$

There exist some cases, however, that one must simulate a pressure flow. Since the inlet pressure is higher than the outlet pressure, a generalized periodic condition must regard the pressure drop. To do so, one starts first with the ideal equation of state (EOS) that emerges from the LBM:

$$p(\vec{x}) = \rho(\vec{x})c_s^2 . \quad (2.58)$$

The periodic condition with pressure variation [44] can be applied in these circumstances. From Equation (2.58), the pressure drop in Figure 6 reads:

$$\delta p = [\rho(x = 0) - \rho(x = L)]c_s^2 = c_s^2 \delta \rho . \quad (2.59)$$

Once  $\delta p$  is available,  $\delta \rho$  is calculated. Hence, if an average density  $\bar{\rho}$  is set inside the domain, the macroscopic densities would be specified in the open boundaries,

$$\rho(x = 0) = \bar{\rho} + 0.5\delta \rho , \quad (2.60)$$

$$\rho(x = L) = \bar{\rho} - 0.5\delta \rho . \quad (2.61)$$

Implementing  $f_i^{neq}(x = 0, y, t) = f_i^{neq}(x = L, y, t)$  in the open boundaries, where  $f_i^{neq} = f_i - f_i^{eq}$  is the non-equilibrium distribution function, the periodic condition with pressure variation for a compressible flow is:

$$f_i(x = 0, y, t + \delta t) = f_i^{eq}(\rho(x = 0, y, t), \vec{u}(x = L, y, t)) + f_{post_i}(x = L, y, t) - f_i^{eq}(x = L, y, t), \quad (2.62)$$

$$f_i(x = L, y, t + \delta t) = f_i^{eq}(\rho(x = L, y, t), \vec{u}(x = 0, y, t)) + f_{post_i}(x = 0, y, t) - f_i^{eq}(x = 0, y, t). \quad (2.63)$$

The periodic condition works as a momentum source when the pressure variation is considered. Still, when only the periodic condition is implemented without pressure variation, one must insert a momentum source, e.g., a moving wall or an external force; otherwise, the simulation will fade in time. Section 2.5 presents how to insert external forces in LBM.

## 2.5 Forcing schemes

Gravitational and electromagnetic forces are present in a great variety of engineering problems. Thus, one is frequently interested in inserting an external force into the LBM procedure, which can be carried out through the forcing term  $F_i$  in the LBE. In 2012, Li *et al.* [45] grouped notable forcing schemes as follows:

$$F_i = \omega_i \left[ \frac{B_e(\vec{F} \cdot \vec{c}_i)}{c_s^2} + \frac{C_e(\vec{u}_{Li}\vec{F} + \vec{F}\vec{u}_{Li}) : (\vec{c}_i\vec{c}_i - c_s^2\mathbf{I})}{2c_s^4} \right], \quad (2.64)$$

where the modified velocity  $\vec{u}_{Li}$  is:

$$\vec{u}_{Li}(\vec{x}) = \frac{1}{\rho} \sum_i f_i \vec{c}_i + A^{Li} \frac{\vec{F} \delta t}{2\rho}, \quad (2.65)$$

and the parameters  $A^{Li}$ ,  $B_e$  and  $C_e$  depend on the forcing scheme selected (see Table 1).

Table 1. Specifications of different forcing schemes.

Forcing schemes	$B_e$ and $C_e$	$A^{Li}$	$A^{eq}$
Shan-Chen [15]	1	$\frac{\tau}{\delta t}$	$\frac{\tau}{\delta t}$
EDM (Exact Difference Method) [46]	1	1	0
Guo <i>et al.</i> [47]	$1 - \frac{1}{2\tau}$	1	$\frac{1}{2}$
Luo <i>et al.</i> [48]	1	0	0
Ladd and Verberg [49]	1	0	0

To ensure second-order space-time accuracy, the real fluid velocity  $\vec{u}$  is calculated through:

$$\vec{u}(\vec{x}) = \frac{1}{\rho} \sum_i f_i \vec{c}_i + \frac{\vec{F} \delta t}{2\rho}. \quad (2.66)$$

Luo *et al.* scheme is the only one which  $\vec{u}$  is still given by Equation (2.23), inducing some additional relevant errors. Another famous method is the He *et al.* forcing scheme [50], but it is essentially the same as the Ladd and Verberg forcing scheme [51].

To calculate  $f_i^{eq}$  in Equation (2.12), the general equilibrium velocity must be written as:

$$\vec{u}^{eq} = \frac{1}{\rho} \sum_i f_i \vec{c}_i + A^{eq} \frac{\vec{F} \delta t}{\rho}, \quad (2.67)$$

where  $A^{eq}$  is a parameter that depends on the forcing scheme (see Table 1).

Li *et al.* [45] have found evidence that the stability and accuracy of LB simulations are strongly connected to the forcing scheme adopted. The Shan-Chen and EDM schemes, for instance, recover the motion equation with additional  $\tau$ -dependent terms. As a consequence, their results (spurious velocities, densities, and surface tensions) are dependent on  $\tau$ . On the other hand, Ladd and Verberg scheme is independent on  $\tau$ , but it achieves weak stability. Among the models in Table 1, the Luo *et al.* scheme attains the worse stability since it causes negative surface tensions in multiphase problems [51].

Although the EDM forcing scheme, directly derived from the BTE [9, 46], is  $\tau$ -dependent, it is a straightforward method to introduce the force. Notice that one handles the forcing schemes displayed in Table 1 only with the BGK model. For MRT, instead, other forcing schemes must be considered [52, 53]. The most common approach for the MRT model [54, 55] is:

$$\mathbf{F}_i = \begin{bmatrix} 0 \\ 6(u_x F_x + u_y F_y) \\ -6(u_x F_x + u_y F_y) \\ F_x \\ -F_x \\ F_y \\ -F_y \\ 2(u_x F_x - u_y F_y) \\ u_x F_x + u_y F_y \end{bmatrix}, \quad (2.68)$$

where  $x$  and  $y$  represent the horizontal and vertical components of  $\vec{F}$  and  $\vec{u}$ . The equilibrium and real macroscopic velocities are still calculated through Equations (2.67) and (2.66) with  $A^{eq} = 1/2$ .

# Chapter 3

## Recovery of transport equations

Various methodologies, such as Finite Volume and Finite Element Methods, can be used numerically to solve the transport equations. In Chapter 2, however, we presented the LBM procedure, centered in the LBE, to model the fluid flow. Chapter 3 mathematically demonstrates, through asymptotic analysis of the BGK-LBE without external force, that the much simpler LBE recovers both the continuity and the Navier-Stokes equations. Although the literature already recognizes it for low Mach number ( $Ma = |\vec{u}|/c_s$ ), the algebraic manipulations are hardly exposed. Looking for providing a clear and didactic way to derive the transport equations, here, instead, based on the thesis of Viggen [30], we exhaustively detail the intermediate mathematical steps. Furthermore, this deduction also contributes to gaining the mathematical tools for performing this type of analysis whenever new LB models are proposed, allowing us to test them for consistency and physical meaning. At the end of this chapter, the connection between the mesoscale modeling and the macroscopic properties will be clear. Understanding it makes us more conscious and critical in discerning assumptions and approximations for a given physical problem. Throughout the chapter, we will often use the Einstein summation convention (index notation).

### 3.1 Chapman-Enskog expansion

In this section, we carry out the Chapman-Enskog expansion. It is essentially a perturbation expansion (see Appendix A) of the LBM variables around their equilibrium values (e.g.,  $f_i^{eq}$ ) that makes the discretization disappear to check for the method consistency.

Initially, we recall the LBE in the absence of an external force:

$$\Omega_i(\vec{x}, t) = f(\vec{x} + \vec{c}_i \delta t, t + \delta t) - f_i(\vec{x}, t) \quad (3.1)$$

With the usual simplification that  $\delta t = 1$ ,

$$\Omega_i(\vec{x}, t) = f_i(\vec{x} + \vec{c}_i, t + 1) - f_i(\vec{x}, t) \quad (3.2)$$

Taylor's series for functions of two variables  $s$  and  $q$  is:

$$\begin{aligned} f(s_0 + \delta s, q_0 + \delta q) = & f(s_0, q_0) + \frac{\partial f(s_0, q_0)}{\partial s} \delta s + \frac{\partial f(s_0, q_0)}{\partial q} \delta q + \\ & + \frac{1}{2!} \left( \frac{\partial^2 f(s_0, q_0)}{\partial s^2} \delta s^2 + \frac{2\partial^2 f(s_0, q_0)}{\partial s \partial q} \delta s \delta q + \right. \\ & \left. + \frac{\partial^2 f(s_0, q_0)}{\partial q^2} \delta q^2 \right) + \\ & + \dots + \frac{1}{z!} \sum_{j=0}^z \binom{z}{j} \frac{\partial^z f(s_0, q_0)}{\partial s^{z-j} \partial q^j} \delta s^{z-j} \delta q^j + R_{z+1}(\delta s, \delta q) \end{aligned} \quad (3.3)$$

where,

$$R_{z+1}(\delta s, \delta q) = \frac{1}{(z+1)!} \sum_{j=0}^{z+1} \binom{z+1}{j} \frac{\partial^{z+1} f(s_0 + \delta s, q_0 + \delta q)}{\partial s^{z+1-j} \partial q^j} \delta s^{z+1-j} \delta q^j \quad (3.4)$$

Then, the second-order Taylor expansion on the RHS of LBE, i.e., Equation (3.2), is:

$$\begin{aligned} \Omega_i(\vec{x}, t) = & f_i(\vec{x}, t) + \left( \vec{\nabla} f_i(\vec{x}, t) \right) \cdot \vec{c}_i + \partial_t f_i(\vec{x}, t) + \frac{1}{2} \left[ \vec{\nabla} \left( \vec{\nabla} f_i(\vec{x}, t) \right) : \vec{c}_i \vec{c}_i \right] + \\ & + \partial_t \left( \vec{\nabla} f_i(\vec{x}, t) \right) \cdot \vec{c}_i + \frac{1}{2} \partial_t^2 f_i(\vec{x}, t) - f_i(\vec{x}, t) \end{aligned} \quad (3.5)$$

After the organization and simplification of terms and the omission of the explicit spatial and time dependence of  $f_i(\vec{x}, t)$ , we find:

$$\Omega_i(\vec{x}, t) = \partial_t f_i + (\vec{\nabla} f_i) \cdot \vec{c}_i + \frac{1}{2} [\vec{\nabla} (\vec{\nabla} f_i) : \vec{c}_i \vec{c}_i] + \partial_t (\vec{\nabla} f_i) \cdot \vec{c}_i + \frac{1}{2} \partial_t^2 f_i \quad (3.6)$$

Through the Einstein summation convention, we can demonstrate that:

$$\vec{\nabla} f_i \cdot \vec{c}_i = \partial_\alpha f_i c_{i\alpha} = \partial_\alpha c_{i\alpha} f_i = \vec{\nabla} \cdot \vec{c}_i f_i \quad (3.7)$$

$$\vec{\nabla} \vec{\nabla} f_i : \vec{c}_i \vec{c}_i = \partial_\alpha \partial_\beta f_i c_{i\beta} c_{i\alpha} = \partial_\alpha \partial_\beta c_{i\beta} c_{i\alpha} f_i = \vec{\nabla} \vec{\nabla} : \vec{c}_i \vec{c}_i f_i \quad (3.8)$$

Note that  $i$  is not an index term of Einstein convention. Instead, here, the index terms are greek letters (i.e.,  $\alpha, \beta, \gamma, \delta, \epsilon$ ). Using Equations (3.7) and (3.8), and factoring out the common factor  $f_i$  in Equation (3.6),

$$\Omega_i(\vec{x}, t) = (\partial_t + \vec{\nabla} \cdot \vec{c}_i) f_i + \left[ \frac{1}{2} (\vec{\nabla} \vec{\nabla} : \vec{c}_i \vec{c}_i) + \partial_t \vec{\nabla} \cdot \vec{c}_i + \frac{1}{2} \partial_t^2 \right] f_i \quad (3.9)$$

From the perturbation theory (see Appendix A), we can expand  $\partial_t, \vec{\nabla}, \Omega_i$  and  $f_i$ . The equilibrium distribution function ( $f_i^{eq}$ ) that emerges in the asymptotic expansion of  $f_i$  is also identified as  $f_i^{(0)}$ . Equations (3.10) to (3.13) are the Chapman-Enskog expansions, where  $\epsilon$  is a small parameter proportional to the Knudsen number. Equation (3.14) arises from the rearrangement of Equation (3.13).

$$\partial_t = \epsilon \partial_{t_1} + \epsilon^2 \partial_{t_2} + \mathcal{O}(\epsilon^3) \quad (3.10)$$

$$\vec{\nabla} = \epsilon \vec{\nabla}_1 + \mathcal{O}(\epsilon^2) \quad (3.11)$$

$$\Omega_i = \Omega_i^{(0)} + \epsilon \Omega_i^{(1)} + \epsilon^2 \Omega_i^{(2)} + \mathcal{O}(\epsilon^3) \quad (3.12)$$

$$f_i = f_i^{(0)} + \epsilon f_i^{(1)} + \mathcal{O}(\epsilon^2) \quad (3.13)$$

$$f_i - f_i^{(0)} = \epsilon f_i^{(1)} + \mathcal{O}(\epsilon^2) \quad (3.14)$$

In Equation (3.10),  $t_1$  and  $t_2$  have physical meanings:  $t_1$  is the time related to the fast phenomena (e.g., advection), and  $t_2$  is related to the slow phenomena (e.g., diffusion).

Substituting the asymptotic expansions of  $\partial_t$  and  $\vec{\nabla}$ , i.e., Equations (3.10) and (3.11), into Equation (3.9),

$$\begin{aligned} \Omega_i(\vec{x}, t) = & (\epsilon \partial_{t_1} + \epsilon^2 \partial_{t_2} + \epsilon \vec{\nabla}_1 \cdot \vec{c}_i) f_i + \left[ \frac{1}{2} (\epsilon^2 \vec{\nabla}_1 \vec{\nabla}_1 : \vec{c}_i \vec{c}_i) + (\epsilon \partial_{t_1} + \right. \\ & \left. + \epsilon^2 \partial_{t_2}) \epsilon \vec{\nabla}_1 \cdot \vec{c}_i + \frac{1}{2} (\epsilon \partial_{t_1} + \epsilon^2 \partial_{t_2}) (\epsilon \partial_{t_1} + \epsilon^2 \partial_{t_2}) \right] f_i \end{aligned} \quad (3.15)$$

Neglecting terms with order greater than  $\mathcal{O}(\epsilon^2)$  and factoring out the common factor  $f_i$ ,

$$\begin{aligned} \Omega_i(\vec{x}, t) = & \left[ \epsilon \partial_{t_1} + \epsilon^2 \partial_{t_2} + \epsilon \vec{\nabla}_1 \cdot \vec{c}_i + \frac{\epsilon^2}{2} (\vec{\nabla}_1 \vec{\nabla}_1 : \vec{c}_i \vec{c}_i) + \epsilon^2 \partial_{t_1} \vec{\nabla}_1 \cdot \right. \\ & \left. \vec{c}_i + \frac{\epsilon^2}{2} \partial_{t_1}^2 \right] f_i + \mathcal{O}(\epsilon^3) \end{aligned} \quad (3.16)$$

Now substituting the asymptotic expansion of  $f_i$ , i.e., Equation (3.13), into Equation (3.16),

$$\begin{aligned} \Omega_i(\vec{x}, t) = & \left[ \epsilon \partial_{t_1} + \epsilon^2 \partial_{t_2} + \epsilon \vec{\nabla}_1 \cdot \vec{c}_i + \frac{\epsilon^2}{2} (\vec{\nabla}_1 \vec{\nabla}_1 : \vec{c}_i \vec{c}_i) + \epsilon^2 \partial_{t_1} \vec{\nabla}_1 \cdot \vec{c}_i + \right. \\ & \left. + \frac{\epsilon^2}{2} \partial_{t_1}^2 \right] (f_i^{(0)} + \epsilon f_i^{(1)}) + \mathcal{O}(\epsilon^3) \end{aligned} \quad (3.17)$$

Factoring out the common factor  $\epsilon$  and neglecting the terms with order greater than  $\mathcal{O}(\epsilon^2)$ ,

$$\begin{aligned} \Omega_i(\vec{x}, t) = & \left[ \epsilon (\partial_{t_1} + \vec{\nabla}_1 \cdot \vec{c}_i) + \epsilon^2 (\partial_{t_2} + \frac{1}{2} (\vec{\nabla}_1 \vec{\nabla}_1 : \vec{c}_i \vec{c}_i) + \partial_{t_1} \vec{\nabla}_1 \cdot \vec{c}_i + \right. \\ & \left. \frac{1}{2} \partial_{t_1}^2) \right] (f_i^{(0)} + \epsilon f_i^{(1)}) + \mathcal{O}(\epsilon^3) \end{aligned} \quad (3.18)$$

$$\begin{aligned} \Omega_i(\vec{x}, t) = & \epsilon (\partial_{t_1} + \vec{\nabla}_1 \cdot \vec{c}_i) f_i^{(0)} + \epsilon^2 \left[ (\partial_{t_2} + \frac{1}{2} (\vec{\nabla}_1 \vec{\nabla}_1 : \vec{c}_i \vec{c}_i) + \partial_{t_1} \vec{\nabla}_1 \cdot \right. \\ & \left. \vec{c}_i + \frac{1}{2} \partial_{t_1}^2) f_i^{(0)} + (\partial_{t_1} + \vec{\nabla}_1 \cdot \vec{c}_i) f_i^{(1)} \right] + \mathcal{O}(\epsilon^3) \end{aligned} \quad (3.19)$$

From a comparison between Equations (3.12) and (3.19), we achieve that:

$$\Omega_i^{(0)} = 0 \quad (3.20)$$

$$\Omega_i^{(1)} = (\partial_{t_1} + \vec{V}_1 \cdot \vec{c}_i) f_i^{(0)} \quad (3.21)$$

$$\begin{aligned} \Omega_i^{(2)} = & \left( \partial_{t_2} + \frac{1}{2} (\vec{V}_1 \vec{V}_1 \cdot \vec{c}_i \vec{c}_i) + \partial_{t_1} \vec{V}_1 \cdot \vec{c}_i + \frac{1}{2} \partial_{t_1}^2 \right) f_i^{(0)} + (\partial_{t_1} + \\ & + \vec{V}_1 \cdot \vec{c}_i) f_i^{(1)} \end{aligned} \quad (3.22)$$

These equations are the main results of the Chapman-Enskog expansion. They will be further used in Section 3.2 when evaluating the zeroth and first moments. But before changing the sections, we have to prove two other equations. Hence, substituting Equation (3.14) into the BGK model,

$$\Omega_i = -\frac{1}{\tau} \left( \epsilon f_i^{(1)} + \mathcal{O}(\epsilon^2) \right) \quad (3.23)$$

Recalling that the collision operator must conserve mass and momentum, i.e.,  $\sum_i \Omega_i = 0$  and  $\sum_i \vec{c}_i \Omega_i = \vec{0}$ ,

$$\sum_i \Omega_i^{(1)} = -\frac{1}{\tau} \epsilon \sum_i f_i^{(1)} \rightarrow \sum_i f_i^{(1)} = 0 \quad (3.24)$$

$$\sum_i \vec{c}_i \Omega_i^{(1)} = -\frac{1}{\tau} \epsilon \sum_i \vec{c}_i f_i^{(1)} \rightarrow \sum_i \vec{c}_i f_i^{(1)} = \vec{0} \quad (3.25)$$

and generalizing,

$$\sum_i f_i^{(k)} = 0, \quad k > 0 \quad (3.26)$$

$$\sum_i \vec{c}_i f_i^{(k)} = \vec{0}, \quad k > 0 \quad (3.27)$$

## 3.2 Moment evaluation

In this section, we use the equations deduced in Section 3.1 to evaluate the zeroth and first-order moments. Just after this assessment, we will be accomplished to recover the transport equations. Initially, we evaluate the zeroth moments, i.e.,  $\sum_i f_i$  or  $\sum_i \Omega_i$ . Hence, imposing the mass conservation  $\sum_i \Omega_i^{(k)} = 0$  in Equation (3.21), i.e., for  $k = 1$ ,

$$\sum_i \Omega_i^{(1)} = \sum_i (\partial_{t_1} + \vec{\nabla}_1 \cdot \vec{c}_i) f_i^{(0)} = \partial_{t_1} \sum_i f_i^{(0)} + \vec{\nabla}_1 \cdot \sum_i \vec{c}_i f_i^{(0)} = 0 \quad (3.28)$$

Since  $\sum_i f_i^{(0)} = \rho$  and  $\sum_i \vec{c}_i f_i^{(0)} = \rho \vec{u}$ , we attain the continuity equation for the time  $t_1$ ,

$$\partial_{t_1} \rho + \vec{\nabla}_1 \cdot \rho \vec{u} = 0 \quad (3.29)$$

Again, imposing the mass conservation  $\sum_i \Omega_i^{(k)} = 0$  in Equation (3.22), i.e., for  $k = 2$ ,

$$\begin{aligned} \sum_i \Omega_i^{(2)} = & \partial_{t_2} \sum_i f_i^{(0)} + \frac{1}{2} (\vec{\nabla}_1 \vec{\nabla}_1 : \sum_i \vec{c}_i \vec{c}_i f_i^{(0)}) + \partial_{t_1} \vec{\nabla}_1 \cdot \sum_i \vec{c}_i f_i^{(0)} + \\ & + \frac{1}{2} \partial_{t_1}^2 \sum_i f_i^{(0)} + \partial_{t_1} \sum_i f_i^{(1)} + \vec{\nabla}_1 \cdot \sum_i \vec{c}_i f_i^{(1)} \end{aligned} \quad (3.30)$$

Since  $\sum_i f_i^{(0)} = \rho$  and  $\sum_i \vec{c}_i f_i^{(0)} = \rho \vec{u}$ , and also recalling Equations (3.26) and (3.27), Equation (3.30) is rewritten as:

$$\partial_{t_2} \rho + \frac{1}{2} (\vec{\nabla}_1 \vec{\nabla}_1 : \sum_i \vec{c}_i \vec{c}_i f_i^{(0)}) + \partial_{t_1} \vec{\nabla}_1 \cdot \rho \vec{u} + \frac{1}{2} \partial_{t_1}^2 \rho = 0 \quad (3.31)$$

As defined in Appendix B,  $\sum_i \vec{c}_i \vec{c}_i f_i^{(k)} = \boldsymbol{\pi}^{(k)} + c_s^2 \mathbf{I} \sum_i f_i^{(k)}$ . Rewriting, then, Equation (3.31),

$$\partial_{t_2}\rho + \frac{1}{2} \left[ \vec{\nabla}_1 \vec{\nabla}_1 : \left( \boldsymbol{\pi}^{(0)} + c_s^2 \mathbf{I} \sum_i f_i^{(0)} \right) \right] + \partial_{t_1} \vec{\nabla}_1 \cdot \rho \vec{u} + \frac{1}{2} \partial_{t_1}^2 \rho = 0 \quad (3.32)$$

Again,  $\sum_i f_i^{(0)} = \rho$ ,

$$\partial_{t_2}\rho + \frac{1}{2} (\vec{\nabla}_1 \vec{\nabla}_1 : \boldsymbol{\pi}^{(0)}) + \frac{c_s^2 \rho}{2} (\vec{\nabla}_1 \vec{\nabla}_1 : \rho \mathbf{I}) + \partial_{t_1} \vec{\nabla}_1 \cdot \rho \vec{u} + \frac{1}{2} \partial_{t_1}^2 \rho = 0 \quad (3.33)$$

Through the Einstein summation convention, we prove that:

$$\vec{\nabla}_1 \vec{\nabla}_1 : \mathbf{I} = \partial_\alpha \partial_\beta \delta_{\beta\alpha} = \partial_\alpha \partial_\alpha = \vec{\nabla}_1 \cdot \vec{\nabla}_1 \quad (3.34)$$

Hence, substituting Equation (3.34) into Equation (3.33),

$$\partial_{t_2}\rho + \frac{1}{2} (\vec{\nabla}_1 \vec{\nabla}_1 : \boldsymbol{\pi}^{(0)}) + \frac{c_s^2}{2} \vec{\nabla}_1 \cdot \vec{\nabla}_1 \rho + \partial_{t_1} \vec{\nabla}_1 \cdot \rho \vec{u} + \frac{1}{2} \partial_{t_1}^2 \rho = 0 \quad (3.35)$$

Equations (3.29) and (3.35) arise from the zeroth-order moment evaluation. Now, we have to evaluate the first-order moments, i.e.,  $\sum_i \vec{c}_i f_i$  or  $\sum_i \vec{c}_i \Omega_i$ . Multiplying Equation (3.21) by  $\vec{c}_i$  and employing the summation,

$$\sum_i \vec{c}_i \Omega_i^{(1)} = \sum_i (\partial_{t_1} + \vec{\nabla}_1 \cdot \vec{c}_i) \vec{c}_i f_i^{(0)} \quad (3.36)$$

Establishing the momentum conservation  $\sum_i \vec{c}_i \Omega_i^{(1)} = \vec{0}$  and breaking the RHS summation,

$$\sum_i \partial_{t_1} \vec{c}_i f_i^{(0)} + \sum_i \vec{\nabla}_1 \cdot \vec{c}_i \vec{c}_i f_i^{(0)} = \vec{0} \quad (3.37)$$

Rearranging the terms,

$$\partial_{t_1} \sum_i \vec{c}_i f_i^{(0)} + \vec{\nabla}_1 \cdot \sum_i \vec{c}_i \vec{c}_i f_i^{(0)} = \vec{0} \quad (3.38)$$

Appendix B shows that  $\sum_i \vec{c}_i f_i^{(0)} = \rho \vec{u}$ ,  $\sum_i f_i^{(0)} = \rho$  and  $\sum_i \vec{c}_i \vec{c}_i f_i^{(0)} = \boldsymbol{\pi}^{(0)} + c_s^2 \mathbf{I} \sum_i f_i^{(0)}$ . Substituting these conditions into Equation (3.38),

$$\partial_{t_1} \rho \vec{u} + \vec{\nabla}_1 \cdot (\boldsymbol{\pi}^{(0)} + c_s^2 \mathbf{I} \rho) = \vec{0} \quad (3.39)$$

and breaking the second term into two components,

$$\partial_{t_1} \rho \vec{u} + \vec{\nabla}_1 \cdot \boldsymbol{\pi}^{(0)} + c_s^2 \vec{\nabla}_1 \cdot (\mathbf{I} \rho) = \vec{0} \quad (3.40)$$

Through Einstein summation convention,

$$\vec{\nabla}_1 \cdot (\mathbf{I} \rho) = \partial_\alpha \delta_{\alpha\beta} \rho = \partial_\beta \rho = \vec{\nabla}_1 \rho, \quad (3.41)$$

we can rewrite  $\vec{\nabla}_1 \cdot (\mathbf{I} \rho)$  in Equation (3.40),

$$\partial_{t_1} \rho \vec{u} + \vec{\nabla}_1 \cdot \boldsymbol{\pi}^{(0)} + c_s^2 \vec{\nabla}_1 \rho = \vec{0} \quad (3.42)$$

We must check the same first-order moment analysis for  $\Omega_i^{(2)}$ . Similarly, as we have done for  $\Omega_i^{(1)}$ , multiplying Equation (3.22) by  $\vec{c}_i$  and employing the summation,

$$\begin{aligned} \sum_i \vec{c}_i \Omega_i^{(2)} &= \partial_{t_2} \sum_i \vec{c}_i f_i^{(0)} + \frac{1}{2} (\vec{\nabla}_1 \vec{\nabla}_1 : \sum_i \vec{c}_i \vec{c}_i \vec{c}_i f_i^{(0)}) + \partial_{t_1} \vec{\nabla}_1 \cdot \sum_i \vec{c}_i \vec{c}_i f_i^{(0)} + \\ &\quad + \frac{1}{2} \partial_{t_1}^2 \sum_i \vec{c}_i f_i^{(0)} + \partial_{t_1} \sum_i \vec{c}_i f_i^{(1)} + \vec{\nabla}_1 \cdot \sum_i \vec{c}_i \vec{c}_i f_i^{(1)} \end{aligned} \quad (3.43)$$

Including the momentum conservation  $\sum_i \vec{c}_i \Omega_i^{(2)} = \vec{0}$  and regarding that, from Appendix B,  $\sum_i \vec{c}_i f_i^{(0)} = \rho \vec{u}$ ,  $\sum_i \vec{c}_i \vec{c}_i f_i^{(0)} = \boldsymbol{\pi}^{(0)} + c_s^2 \mathbf{I} \sum_i f_i^{(0)}$ ,  $\sum_i \vec{c}_i \vec{c}_i \vec{c}_i f_i^{(0)} = \mathbf{R}^{(0)}$ , and  $\sum_i f_i^{(0)} = \rho$ , Equation (3.43) is simplified to:

$$\begin{aligned} \partial_{t_2} \rho \vec{u} + \frac{1}{2} (\vec{\nabla}_1 \vec{\nabla}_1 : \mathbf{R}^{(0)}) + \partial_{t_1} \vec{\nabla}_1 \cdot (\boldsymbol{\pi}^{(0)} + c_s^2 \mathbf{I} \rho) + \frac{1}{2} \partial_{t_1}^2 \rho \vec{u} + \\ + \partial_{t_1} \sum_i \vec{c}_i f_i^{(1)} + \vec{\nabla}_1 \cdot \sum_i \vec{c}_i \vec{c}_i f_i^{(1)} = \vec{0} \end{aligned} \quad (3.44)$$

Since  $\sum_i \vec{c}_i \vec{c}_i f_i^{(1)} = \boldsymbol{\pi}^{(1)} + c_s^2 \mathbf{I} \sum_i f_i^{(1)}$  (see Appendix B) and  $\sum_i \vec{c}_i f_i^{(1)} = \vec{0}$  (see Equation (3.27)),

$$\partial_{t_2} \rho \vec{u} + \frac{1}{2} (\vec{\nabla}_1 \vec{\nabla}_1 : \mathbf{R}^{(0)}) + \partial_{t_1} \vec{\nabla}_1 \cdot (\boldsymbol{\pi}^{(0)} + c_s^2 \mathbf{I} \rho) + \frac{1}{2} \partial_{t_1}^2 \rho \vec{u} + \vec{\nabla}_1 \cdot \boldsymbol{\pi}^{(1)} = \vec{0} \quad (3.45)$$

Breaking the third term into two components,

$$\begin{aligned} \partial_{t_2} \rho \vec{u} + \frac{1}{2} (\vec{\nabla}_1 \vec{\nabla}_1 : \mathbf{R}^{(0)}) + \partial_{t_1} \vec{\nabla}_1 \cdot \boldsymbol{\pi}^{(0)} + c_s^2 \partial_{t_1} (\vec{\nabla}_1 \cdot \mathbf{I} \rho) + \frac{1}{2} \partial_{t_1}^2 \rho \vec{u} + \\ + \vec{\nabla}_1 \cdot \boldsymbol{\pi}^{(1)} = \vec{0}, \end{aligned} \quad (3.46)$$

and as we have already demonstrated that:

$$\vec{\nabla}_1 \cdot \mathbf{I} \rho = \vec{\nabla}_1 \rho, \quad (3.47)$$

we can write:

$$\begin{aligned} \partial_{t_2} \rho \vec{u} + \frac{1}{2} (\vec{\nabla}_1 \vec{\nabla}_1 : \mathbf{R}^{(0)}) + \partial_{t_1} \vec{\nabla}_1 \cdot \boldsymbol{\pi}^{(0)} + \vec{\nabla}_1 \cdot \boldsymbol{\pi}^{(1)} + c_s^2 \partial_{t_1} \vec{\nabla}_1 \rho + \frac{1}{2} \partial_{t_1}^2 \rho \vec{u} = \\ = \vec{0} \end{aligned} \quad (3.48)$$

Finally, we gained four main equations by evaluating the moments: Equations (3.29) and (3.35) arose from the zeroth-order moment evaluation, and Equations (3.42) and (3.48) from the first-order moment evaluation. They will be further combined and used in Sections 3.3 and 3.4 to recover the continuity and Navier-Stokes equations.

### 3.3 Continuity equation

In this section, we deduce the continuity equation by combining Equations (3.29), (3.35), and (3.42) from Section 3.2. Initially, we can write Equation (3.29) as:

$$\partial_{t_1}\rho = -\vec{\nabla}_1 \cdot \rho\vec{u} \quad (3.49)$$

Substituting Equation (3.49) into Equation (3.35),

$$\partial_{t_2}\rho + \frac{1}{2}(\vec{\nabla}_1\vec{\nabla}_1:\boldsymbol{\pi}^{(0)}) + \frac{c_s^2}{2}\vec{\nabla}_1 \cdot \vec{\nabla}_1\rho + \partial_{t_1}\vec{\nabla}_1 \cdot \rho\vec{u} - \frac{1}{2}\partial_{t_1}(\vec{\nabla}_1 \cdot \rho\vec{u}) = 0 \quad , \quad (3.50)$$

and simplifying,

$$\partial_{t_2}\rho + \frac{1}{2}(\vec{\nabla}_1\vec{\nabla}_1:\boldsymbol{\pi}^{(0)}) + \frac{c_s^2}{2}\vec{\nabla}_1 \cdot \vec{\nabla}_1\rho + \frac{1}{2}\partial_{t_1}\vec{\nabla}_1 \cdot \rho\vec{u} = 0 \quad (3.51)$$

Equation (3.51) is the first outcome obtained by manipulating two main equations of Section 3.2, i.e., Equations (3.29) and (3.35). Now, we quickly investigate Equation (3.42). Employing the divergence operator in Equation (3.42) and multiplying it by  $\frac{1}{2}$ ,

$$\frac{1}{2}\partial_{t_1}\vec{\nabla}_1 \cdot \rho\vec{u} + \frac{1}{2}\vec{\nabla}_1 \cdot (\vec{\nabla}_1 \cdot \boldsymbol{\pi}^{(0)}) + \frac{c_s^2}{2}\vec{\nabla}_1 \cdot (\vec{\nabla}_1\rho) = 0 \quad (3.52)$$

Through Einstein summation convention, we note that:

$$\vec{\nabla}_1 \cdot (\vec{\nabla}_1 \cdot \boldsymbol{\pi}^{(0)}) = \partial_\alpha (\partial_\alpha \pi_{\alpha\beta}) = \partial_\alpha \partial_\alpha \pi_{\alpha\beta} = \vec{\nabla}_1 \vec{\nabla}_1 : \boldsymbol{\pi}^{(0)} \quad (3.53)$$

Then, Equation (3.52) becomes:

$$\frac{1}{2} (\vec{\nabla}_1 \vec{\nabla}_1 : \boldsymbol{\pi}^{(0)}) + \frac{c_s^2}{2} \vec{\nabla}_1 \cdot \vec{\nabla}_1 \rho + \frac{1}{2} \partial_{t_1} \vec{\nabla}_1 \cdot \rho \vec{u} = 0 \quad (3.54)$$

Substituting Equation (3.54) into Equation (3.51),

$$\partial_{t_2} \rho = 0 \quad (3.55)$$

As we have disclosed,  $t_2$  is the time related to slow phenomena, e.g., diffusion. Equation (3.55) specifies there is mass conservation for this kind of phenomenon. But what about advection phenomena? We must inspect the complete continuity equation, i.e., when we consider the time  $t$ , instead of only  $t_1$  or  $t_2$ .

Employing the time derivative of the density  $\rho$  and recalling the asymptotic expansion of  $\partial_t$  from Equation (3.10),

$$\partial_t \rho = \epsilon \partial_{t_1} \rho + \epsilon^2 \partial_{t_2} \rho \quad (3.56)$$

Substituting Equation (3.55) into Equation (3.56),

$$\partial_t \rho = \epsilon \partial_{t_1} \rho \quad (3.57)$$

Substituting Equations (3.57) and (3.11) into Equation (3.29),

$$\frac{1}{\epsilon} \partial_t \rho + \frac{1}{\epsilon} \vec{\nabla} \cdot \rho \vec{u} = 0 \quad , \quad (3.58)$$

and multiplying by  $\epsilon$ , we finally recover the continuity equation,

$$\partial_t \rho + \vec{\nabla} \cdot \rho \vec{u} = 0 \quad (3.59)$$

Hence, we recovered the continuity equation, which expresses the mass conservation, combining three of the four main equations deduced in Section 3.2, i.e., Equations (3.29), (3.35), and (3.42).

### 3.4 Navier-Stokes equation

Similar to what we have performed in Section 3.3 to recover the continuity equation, we can also combine the main equations of Section 3.2 to recover the Navier-Stokes equation. Note that Equation (3.48) was not used yet; we use it in this section. But, first, employing the time derivative related to the fast phenomena ( $\partial_{t_1}$ ) in Equation (3.42), multiplying it by  $\frac{1}{2}$ , and isolating the first term, we get:

$$\frac{1}{2} \partial_{t_1}^2 \rho \vec{u} = -\frac{1}{2} \partial_{t_1} \vec{\nabla}_1 \cdot \boldsymbol{\pi}^{(0)} - \frac{1}{2} c_s^2 \partial_{t_1} \vec{\nabla}_1 \rho \quad (3.60)$$

Substituting Equation (3.60) into Equation (3.48),

$$\begin{aligned} \partial_{t_2} \rho \vec{u} + \frac{1}{2} (\vec{\nabla}_1 \vec{\nabla}_1 : \mathbf{R}^{(0)}) + \partial_{t_1} \vec{\nabla}_1 \cdot \boldsymbol{\pi}^{(0)} + \vec{\nabla}_1 \cdot \boldsymbol{\pi}^{(1)} + c_s^2 \partial_{t_1} \vec{\nabla}_1 \rho + \\ -\frac{1}{2} \partial_{t_1} \vec{\nabla}_1 \cdot \boldsymbol{\pi}^{(0)} - \frac{1}{2} c_s^2 \partial_{t_1} \vec{\nabla}_1 \rho = \vec{0} \quad , \end{aligned} \quad (3.61)$$

and simplifying it,

$$\partial_{t_2} \rho \vec{u} + \frac{1}{2} (\vec{\nabla}_1 \vec{\nabla}_1 : \mathbf{R}^{(0)}) + \frac{1}{2} \partial_{t_1} \vec{\nabla}_1 \cdot \boldsymbol{\pi}^{(0)} + \vec{\nabla}_1 \cdot \boldsymbol{\pi}^{(1)} + \frac{1}{2} c_s^2 \partial_{t_1} \vec{\nabla}_1 \rho = \vec{0} \quad (3.62)$$

To recover  $\partial_t$  and  $\vec{\nabla}$ , we must perform the reverse Chapman-Enskog expansion. Thus, multiplying Equation (3.42) by  $\epsilon$  and Equation (3.62) by  $\epsilon^2$ , we find, respectively,

$$\epsilon \partial_{t_1} \rho \vec{u} + \epsilon \vec{\nabla}_1 \cdot \boldsymbol{\pi}^{(0)} + c_s^2 \epsilon \vec{\nabla}_1 \rho = \vec{0} \quad (3.63)$$

$$\begin{aligned} \epsilon^2 \partial_{t_2} \rho \vec{u} + \frac{1}{2} (\epsilon \vec{\nabla}_1 \epsilon \vec{\nabla}_1 : \mathbf{R}^{(0)}) + \frac{1}{2} \epsilon \partial_{t_1} \epsilon \vec{\nabla}_1 \cdot \boldsymbol{\pi}^{(0)} + \epsilon^2 \vec{\nabla}_1 \cdot \boldsymbol{\pi}^{(1)} + \\ + \frac{1}{2} c_s^2 \epsilon \partial_{t_1} \epsilon \vec{\nabla}_1 \rho = \vec{0} \end{aligned} \quad (3.64)$$

Summing both equations and grouping similar terms,

$$\begin{aligned} (\epsilon \partial_{t_1} + \epsilon^2 \partial_{t_2}) \rho \vec{u} + \epsilon \vec{\nabla}_1 \cdot (\boldsymbol{\pi}^{(0)} + \epsilon \boldsymbol{\pi}^{(1)}) + \left(1 + \frac{\epsilon}{2} \partial_{t_1}\right) c_s^2 \epsilon \vec{\nabla}_1 \rho + \\ + \frac{1}{2} \epsilon \partial_{t_1} \epsilon \vec{\nabla}_1 \cdot \boldsymbol{\pi}^{(0)} + \frac{1}{2} (\epsilon \vec{\nabla}_1 \epsilon \vec{\nabla}_1 : \mathbf{R}^{(0)}) = \vec{0} \end{aligned} \quad (3.65)$$

Substituting the asymptotic expansions of  $\partial_t$  and  $\vec{\nabla}$ , i.e., Equations (3.10) and (3.11),

$$\begin{aligned} \partial_t \rho \vec{u} + \vec{\nabla} \cdot (\boldsymbol{\pi}^{(0)} + \epsilon \boldsymbol{\pi}^{(1)}) + \left(1 + \frac{\epsilon}{2} \partial_{t_1}\right) c_s^2 \vec{\nabla} \rho + \frac{1}{2} \epsilon \partial_{t_1} \vec{\nabla} \cdot \boldsymbol{\pi}^{(0)} + \\ + \frac{1}{2} (\vec{\nabla} \vec{\nabla} : \mathbf{R}^{(0)}) = \vec{0} \end{aligned} \quad (3.66)$$

But we can rewrite the third term as,

$$\left(1 + \frac{\epsilon}{2} \partial_{t_1}\right) c_s^2 \vec{\nabla} \rho = c_s^2 \vec{\nabla} \rho + \frac{\epsilon}{2} \partial_{t_1} c_s^2 \vec{\nabla} \rho = c_s^2 \vec{\nabla} \rho + \frac{c_s^2}{2} \vec{\nabla} \epsilon \partial_{t_1} \rho, \quad (3.67)$$

and then, substitute Equation (3.57) into Equation (3.67),

$$\left(1 + \frac{\epsilon}{2} \partial_{t_1}\right) c_s^2 \vec{\nabla} \rho = c_s^2 \vec{\nabla} \rho + \frac{c_s^2}{2} \vec{\nabla} \partial_t \rho = \left(1 + \frac{\partial_t}{2}\right) c_s^2 \vec{\nabla} \rho \quad (3.68)$$

Hence, the third term of Equation (3.66) can be rewritten as shown in Equation (3.68). Equation (3.66), then, becomes:

$$\partial_t \rho \vec{u} + \vec{\nabla} \cdot (\boldsymbol{\pi}^{(0)} + \epsilon \boldsymbol{\pi}^{(1)}) + \left(1 + \frac{\partial_t}{2}\right) c_s^2 \vec{\nabla} \rho + \frac{\epsilon}{2} \partial_{t_1} \vec{\nabla} \cdot \boldsymbol{\pi}^{(0)} + \frac{1}{2} (\vec{\nabla} \vec{\nabla} : \mathbf{R}^{(0)}) = \vec{0} \quad (3.69)$$

Equation (3.69) is already the Navier-Stokes equation; however, we can customize it to present the equation with well-known terms. In Appendix B, we observe that  $\boldsymbol{\pi}^{(0)}$  and  $\mathbf{R}^{(0)}$  depend on the equilibrium distribution function  $f_i^{(0)}$ , which emerges from the Maxwell distribution as:

$$f_i^{(0)} = \rho \omega_i \left( 1 + \frac{\vec{u} \cdot \vec{c}_i}{c_s^2} + \frac{(\vec{u} \cdot \vec{c}_i)^2}{2 c_s^4} - \frac{\vec{u} \cdot \vec{u}}{2 c_s^2} \right) \quad (3.70)$$

Rewriting Equation (3.70) by considering the Einstein summation convention,

$$f_i^{(0)} = \rho \omega_i \left( 1 + \frac{u_\alpha c_{i\alpha}}{c_s^2} + \frac{u_\alpha c_{i\alpha} u_\beta c_{i\beta}}{2 c_s^4} - \frac{u_\alpha u_\alpha}{2 c_s^2} \right) \quad (3.71)$$

Similarly, we can also write  $\boldsymbol{\pi}^{(0)}$  (see Appendix B) with Einstein summation convention and recall that  $\sum_i f_i^{(0)} = \rho$ ,

$$\pi_{\alpha\beta}^{(0)} = \sum_i c_{i\alpha} c_{i\beta} f_i^{(0)} - c_s^2 \delta_{\alpha\beta} \rho \quad (3.72)$$

Substituting Equation (3.71) into Equation (3.72),

$$\begin{aligned} \pi_{\alpha\beta}^{(0)} = & \rho \sum_i \omega_i c_{i\alpha} c_{i\beta} + \frac{\rho u_\gamma}{c_s^2} \sum_i \omega_i c_{i\alpha} c_{i\beta} c_{i\gamma} + \frac{\rho u_\gamma u_\delta}{2 c_s^4} \sum_i \omega_i c_{i\alpha} c_{i\beta} c_{i\gamma} c_{i\delta} + \\ & - \frac{\rho u_\gamma u_\gamma}{2 c_s^2} \sum_i \omega_i c_{i\alpha} c_{i\beta} - c_s^2 \delta_{\alpha\beta} \rho \quad , \end{aligned} \quad (3.73)$$

and substituting the isotropy conditions (see Appendix B) for BGK collision operator,

$$\begin{aligned} \boldsymbol{\pi}^{(0)} = & \rho c_s^2 \delta_{\alpha\beta} + \frac{\rho u_\gamma u_\delta}{2} \delta_{\alpha\beta} \delta_{\gamma\delta} + \frac{\rho u_\gamma u_\delta}{2} \delta_{\alpha\gamma} \delta_{\beta\delta} + \frac{\rho u_\gamma u_\delta}{2} \delta_{\alpha\delta} \delta_{\beta\gamma} + \\ & - \frac{\rho u_\gamma u_\gamma}{2} \delta_{\alpha\beta} - \rho c_s^2 \delta_{\alpha\beta} \end{aligned} \quad (3.74)$$

To attain the final expression for  $\boldsymbol{\pi}^{(0)}$ , we must observe some index operations. First, resolving the dot products between tensor and vector,

$$u_\gamma u_\delta \delta_{\alpha\beta} \delta_{\gamma\delta} = u_\gamma u_\gamma \delta_{\alpha\beta} \quad (3.75)$$

$$u_\gamma u_\delta \delta_{\alpha\gamma} \delta_{\beta\delta} = u_\alpha u_\beta \quad (3.76)$$

$$u_\gamma u_\delta \delta_{\alpha\delta} \delta_{\beta\gamma} = u_\beta u_\alpha \quad (3.77)$$

Implementing these operations in Equation (3.74),

$$\boldsymbol{\pi}^{(0)} = \frac{\rho u_\gamma u_\gamma}{2} \delta_{\alpha\beta} + \frac{\rho u_\alpha u_\beta}{2} + \frac{\rho u_\beta u_\alpha}{2} - \frac{\rho u_\gamma u_\gamma}{2} \delta_{\alpha\beta} , \quad (3.78)$$

and simplifying it,

$$\boldsymbol{\pi}^{(0)} = \frac{\rho}{2} u_\alpha u_\beta + \frac{\rho}{2} u_\beta u_\alpha \quad (3.79)$$

$$\boldsymbol{\pi}^{(0)} = \frac{\rho}{2} (u_\alpha u_\beta + u_\beta u_\alpha) \quad (3.80)$$

Returning to the direct tensor notation, since  $u_\alpha$  and  $u_\beta$  are the same vector  $\vec{u}$ ,

$$\boldsymbol{\pi}^{(0)} = \frac{\rho}{2} (\vec{u}\vec{u} + \vec{u}\vec{u}) \quad (3.81)$$

$$\boldsymbol{\pi}^{(0)} = \rho \vec{u}\vec{u} \quad (3.82)$$

Therefore, we calculated the tensor  $\boldsymbol{\pi}^{(0)}$ , which can already be substituted into Equation (3.69). But, as a next step, we first evaluate the tensor  $\mathbf{R}^{(0)} = \sum_i \vec{c}_i \vec{c}_i \vec{c}_i f_i^{(0)}$ . Substituting Equation (3.71) into  $\mathbf{R}^{(0)}$  definition,

$$\begin{aligned} \mathbf{R}^{(0)} = & \left( \sum_i \omega_i c_{i\alpha} c_{i\beta} c_{i\gamma} \right) \rho + \frac{u_\delta}{c_s^2} \left( \sum_i \omega_i c_{i\alpha} c_{i\beta} c_{i\gamma} c_{i\delta} \right) \rho + \\ & + \frac{u_\delta u_\epsilon}{2c_s^4} \left( \sum_i \omega_i c_{i\alpha} c_{i\beta} c_{i\gamma} c_{i\delta} c_{i\epsilon} \right) \rho - \frac{u_\delta u_\delta}{2c_s^2} \left( \sum_i \omega_i c_{i\alpha} c_{i\beta} c_{i\gamma} \right) \rho \end{aligned} \quad (3.83)$$

Enforcing the isotropy conditions (see Appendix B),

$$\mathbf{R}^{(0)} = u_\delta c_s^2 (\delta_{\alpha\beta} \delta_{\gamma\delta} + \delta_{\alpha\gamma} \delta_{\beta\delta} + \delta_{\alpha\delta} \delta_{\beta\gamma}) \rho, \quad (3.84)$$

and calculating the dot products,

$$u_\delta \delta_{\alpha\beta} \delta_{\gamma\delta} = u_\gamma \delta_{\alpha\beta} \quad (3.85)$$

$$u_\delta \delta_{\alpha\gamma} \delta_{\beta\delta} = u_\beta \delta_{\alpha\gamma} \quad (3.86)$$

$$u_\delta \delta_{\alpha\delta} \delta_{\beta\gamma} = u_\alpha \delta_{\beta\gamma} \quad (3.87)$$

Substituting the dot operations into Equation (3.84), we obtain  $\mathbf{R}^{(0)}$ , which we will maintain in index notation because it will be further required.

$$\mathbf{R}^{(0)} = c_s^2 (u_\gamma \delta_{\alpha\beta} + u_\beta \delta_{\alpha\gamma} + u_\alpha \delta_{\beta\gamma}) \rho \quad (3.88)$$

Hence, in this section, we already reached the tensors  $\mathbf{R}^{(0)}$  and  $\boldsymbol{\pi}^{(0)}$ . However, to complete Equation (3.69), we must determine  $\boldsymbol{\pi}^{(1)}$ . Differently to  $\mathbf{R}^{(0)}$  and  $\boldsymbol{\pi}^{(0)}$  calculations, which we know  $f_i^{(0)}$ ,  $f_i^{(1)}$  is unknown to calculate  $\boldsymbol{\pi}^{(1)}$ . The deduction of  $f_i^{(1)}$  goes from Equation (3.89) to Equation (3.136). The strategy to obtain it is to substitute Equation (3.21) into  $\Omega_i^{(1)} = -\frac{1}{\tau} f_i^{(1)}$  (see Equation (3.23)) and isolate  $f_i^{(1)}$ ,

$$f_i^{(1)} = -\tau(\partial_{t_1} + \vec{\nabla}_1 \cdot \vec{c}_i)f_i^{(0)} \quad (3.89)$$

Before we substitute Equation (3.70) into Equation (3.89), to turn the algebraic manipulations easier, we need to rearrange two terms of Equation (3.70),  $(\vec{u} \cdot \vec{c}_i)^2$  and  $\vec{u} \cdot \vec{u}$ ,

$$(\vec{u} \cdot \vec{c}_i)^2 = (\vec{u} \cdot \vec{c}_i)(\vec{u} \cdot \vec{c}_i) = u_\alpha c_{i\alpha} u_\beta c_{i\beta} = u_\alpha u_\beta c_{i\beta} c_{i\alpha} = \vec{u}\vec{u} : \vec{c}_i \vec{c}_i \quad (3.90)$$

$$\vec{u} \cdot \vec{u} = u_\alpha u_\alpha = u_\alpha u_\beta \delta_{\beta\alpha} = \vec{u}\vec{u} : \mathbf{I} \quad (3.91)$$

Equation (3.70) becomes, then,

$$f_i^{(0)} = \rho\omega_i \left( 1 + \frac{\vec{u} \cdot \vec{c}_i}{c_s^2} + \frac{\vec{u}\vec{u} : \vec{c}_i \vec{c}_i}{2 c_s^4} - \frac{\vec{u}\vec{u} : \mathbf{I}}{2 c_s^2} \right) \quad (3.92)$$

When we sum the last two terms of Equation (3.92),

$$f_i^{(0)} = \rho\omega_i \left[ 1 + \frac{\vec{u} \cdot \vec{c}_i}{c_s^2} + \frac{(\vec{u}\vec{u} : \vec{c}_i \vec{c}_i) - c_s^2(\vec{u}\vec{u} : \mathbf{I})}{2 c_s^4} \right] \quad (3.93)$$

From Appendix B,  $\vec{c}_i \vec{c}_i = \mathbf{Q}_i + c_s^2 \mathbf{I}$ ,

$$f_i^{(0)} = \rho\omega_i \left[ 1 + \frac{\vec{u} \cdot \vec{c}_i}{c_s^2} + \frac{(\vec{u}\vec{u} : (\mathbf{Q}_i + c_s^2 \mathbf{I})) - (\vec{u}\vec{u} : c_s^2 \mathbf{I})}{2 c_s^4} \right] \quad (3.94)$$

Simplifying,

$$f_i^{(0)} = \rho\omega_i \left[ 1 + \frac{\vec{u} \cdot \vec{c}_i}{c_s^2} + \frac{\vec{u}\vec{u} : \mathbf{Q}_i}{2 c_s^4} \right] \quad (3.95)$$

Substituting Equation (3.95) into Equation (3.89),

$$f_i^{(1)} = -\tau(\partial_{t_1} + \vec{\nabla}_1 \cdot \vec{c}_i)\rho\omega_i \left[ 1 + \frac{\vec{u} \cdot \vec{c}_i}{c_s^2} + \frac{\vec{u}\vec{u} : \mathbf{Q}_i}{2 c_s^4} \right], \quad (3.96)$$

and employing the distributive property,

$$f_i^{(1)} = -\tau\omega_i \left[ \partial_{t_1}\rho + \frac{\partial_{t_1}(\rho\vec{u} \cdot \vec{c}_i)}{c_s^2} + \frac{\partial_{t_1}(\rho\vec{u}\vec{u} : \mathbf{Q}_i)}{2 c_s^4} + (\vec{\nabla}_1 \cdot \vec{c}_i)\rho + \frac{(\vec{\nabla}_1 \cdot \vec{c}_i)(\vec{u} \cdot \vec{c}_i)\rho}{c_s^2} + \frac{(\vec{\nabla}_1 \cdot \vec{c}_i)(\rho\vec{u}\vec{u} : \mathbf{Q}_i)}{2 c_s^4} \right] \quad (3.97)$$

Using the Einstein summation convention, we can prove that:

$$(\vec{\nabla}_1 \cdot \vec{c}_i)\rho = \partial_\alpha c_{i\alpha}\rho = c_{i\alpha} \partial_\alpha \rho = \vec{c}_i \cdot \vec{\nabla}_1 \rho \quad (3.98)$$

$$(\vec{\nabla}_1 \cdot \vec{c}_i)(\rho\vec{u} \cdot \vec{c}_i) = \partial_\alpha c_{i\alpha}\rho u_\beta c_{i\beta} = c_{i\alpha} c_{i\beta} \partial_\alpha \rho u_\beta = \vec{c}_i \vec{c}_i : \vec{\nabla}_1(\rho\vec{u}) \quad (3.99)$$

Substituting these relations into Equation (3.97),

$$f_i^{(1)} = -\tau\omega_i \left[ \partial_{t_1}\rho + \frac{\partial_{t_1}(\rho\vec{u} \cdot \vec{c}_i)}{c_s^2} + \frac{\partial_{t_1}(\rho\vec{u}\vec{u} : \mathbf{Q}_i)}{2 c_s^4} + \vec{c}_i \cdot \vec{\nabla}_1 \rho + \frac{\vec{c}_i \vec{c}_i : \vec{\nabla}_1(\rho\vec{u})}{c_s^2} + \frac{(\vec{\nabla}_1 \cdot \vec{c}_i)(\rho\vec{u}\vec{u} : \mathbf{Q}_i)}{2 c_s^4} \right] \quad (3.100)$$

We will substitute and simplify some terms of Equation (3.100), but we must first handle some algebraic efforts. From Equation (3.29),

$$\partial_{t_1}\rho = -\vec{\nabla}_1 \cdot \rho\vec{u} \quad (3.101)$$

Employing the dot product of each term of Equation (3.42) by  $\frac{\vec{c}_i}{c_s^2}$ ,

$$\partial_{t_1}\rho\vec{u} \cdot \frac{\vec{c}_i}{c_s^2} + \vec{\nabla}_1 \cdot \boldsymbol{\pi}^{(0)} \cdot \frac{\vec{c}_i}{c_s^2} + c_s^2 \vec{\nabla}_1 \rho \cdot \frac{\vec{c}_i}{c_s^2} = \vec{0} \quad (3.102)$$

Isolating the first term,

$$\frac{\partial_{t_1}(\rho\vec{u} \cdot \vec{c}_i)}{c_s^2} = -\frac{\vec{\nabla}_1 \cdot \boldsymbol{\pi}^{(0)} \cdot \vec{c}_i}{c_s^2} - \vec{\nabla}_1 \rho \cdot \vec{c}_i \quad (3.103)$$

Again, employing the Einstein summation convention, we can see that:

$$\vec{\nabla}_1 \cdot \boldsymbol{\pi}^{(0)} \cdot \vec{c}_i = \partial_\alpha \pi_{\alpha\beta} c_{i\beta} = c_{i\beta} \partial_\alpha \pi_{\alpha\beta} = \vec{c}_i \vec{\nabla}_1 : \boldsymbol{\pi}^{(0)} \quad (3.104)$$

Using Equation (3.104) to rewrite Equation (3.103),

$$\frac{\partial_{t_1}(\rho\vec{u} \cdot \vec{c}_i)}{c_s^2} = -\frac{\vec{c}_i \vec{\nabla}_1 : \boldsymbol{\pi}^{(0)}}{c_s^2} - \vec{\nabla}_1 \rho \cdot \vec{c}_i \quad (3.105)$$

Since we already know  $\boldsymbol{\pi}^{(0)}$  from Equation (3.82),

$$\frac{\partial_{t_1}(\rho\vec{u} \cdot \vec{c}_i)}{c_s^2} = -\frac{\vec{c}_i \vec{\nabla}_1 : \rho\vec{u}\vec{u}}{c_s^2} - \vec{\nabla}_1 \rho \cdot \vec{c}_i \quad (3.106)$$

Stay aware that we want an expression for  $f_i^{(1)}$  to calculate  $\boldsymbol{\pi}^{(1)}$ . So, substituting Equations (3.101) and (3.106) into Equation (3.100), and regarding that  $\vec{\nabla}_1 \rho \cdot \vec{c}_i = \vec{c}_i \cdot \vec{\nabla}_1 \rho$ ,

$$f_i^{(1)} = -\tau\omega_i \left[ -\vec{c}_i \cdot \vec{\nabla}_1 \rho - \vec{\nabla}_1 \cdot \rho\vec{u} - \frac{\vec{c}_i \vec{\nabla}_1 : \rho\vec{u}\vec{u}}{c_s^2} + \frac{\partial_{t_1}(\rho\vec{u}\vec{u} : \mathbf{Q}_i)}{2 c_s^4} + \vec{c}_i \cdot \vec{\nabla}_1 \rho + \frac{\vec{c}_i \vec{c}_i : \vec{\nabla}_1(\rho\vec{u})}{c_s^2} + \frac{(\vec{\nabla}_1 \cdot \vec{c}_i)(\rho\vec{u}\vec{u} : \mathbf{Q}_i)}{2 c_s^4} \right] \quad (3.107)$$

Simplifying,

$$f_i^{(1)} = -\tau\omega_i \left[ -\vec{\nabla}_1 \cdot \rho\vec{u} - \frac{\vec{c}_i \vec{\nabla}_1 : \rho\vec{u}\vec{u}}{c_s^2} + \frac{\partial_{t_1}(\rho\vec{u}\vec{u} : \mathbf{Q}_i)}{2 c_s^4} + \frac{\vec{c}_i \vec{c}_i : \vec{\nabla}_1(\rho\vec{u})}{c_s^2} + \frac{(\vec{\nabla}_1 \cdot \vec{c}_i)(\rho\vec{u}\vec{u} : \mathbf{Q}_i)}{2 c_s^4} \right] \quad (3.108)$$

Note that we can write the third term of Equation (3.108) in another way,

$$\partial_{t_1}(\rho\vec{u}\vec{u} : \mathbf{Q}_i) = \partial_{t_1}(\rho u_\alpha u_\beta Q_{\beta\alpha}) = Q_{\beta\alpha} \partial_{t_1}(\rho u_\alpha u_\beta) = \mathbf{Q}_i : \partial_{t_1}(\rho\vec{u}\vec{u}) \quad (3.109)$$

In this way, we can quickly evaluate the time derivative of  $\rho\vec{u}\vec{u}$ . Employing the product rule with Einstein notation,

$$\partial_{t_1}(\rho\vec{u}\vec{u}) = \partial_{t_1}(\rho u_\alpha u_\beta) = [\partial_{t_1}(\rho u_\alpha)] u_\beta + \rho u_\alpha \partial_{t_1} u_\beta \quad (3.110)$$

Employing the product rule of the first derivative again on RHS,

$$\partial_{t_1}(\rho u_\alpha u_\beta) = u_\alpha (\partial_{t_1} \rho) u_\beta + (\partial_{t_1} u_\alpha) \rho u_\beta + \rho u_\alpha \partial_{t_1} u_\beta \quad (3.111)$$

We can write  $\partial_{t_1}(\rho\vec{u}\vec{u})$  differently than the way expressed by Equation (3.110) if the product rule regards another set of terms,

$$\partial_{t_1}(\rho u_\alpha u_\beta) = \partial_{t_1}(\rho u_\alpha u_\beta) = u_\alpha \partial_{t_1}(\rho u_\beta) + (\partial_{t_1} u_\alpha) \rho u_\beta \quad (3.112)$$

Summing Equations (3.110) with (3.112) and subtracting Equation (3.111) from them,

$$\begin{aligned} 2\partial_{t_1}(\rho u_\alpha u_\beta) - \partial_{t_1}(\rho u_\alpha u_\beta) &= [\partial_{t_1}(\rho u_\alpha)] u_\beta + \rho u_\alpha \partial_{t_1} u_\beta + u_\alpha \partial_{t_1}(\rho u_\beta) + \\ &\quad + (\partial_{t_1} u_\alpha) \rho u_\beta - u_\alpha (\partial_{t_1} \rho) u_\beta + \\ &\quad - (\partial_{t_1} u_\alpha) \rho u_\beta - \rho u_\alpha \partial_{t_1} u_\beta \end{aligned} \quad (3.113)$$

Simplifying,

$$\partial_{t_1}(\rho u_\alpha u_\beta) = \partial_{t_1}(\rho u_\alpha)u_\beta + u_\alpha \partial_{t_1}(\rho u_\beta) - (\partial_{t_1}\rho)u_\alpha u_\beta \quad (3.114)$$

Returning to the direct tensor notation:

$$\partial_{t_1}(\rho \vec{u}\vec{u}) = \partial_{t_1}(\rho \vec{u})\vec{u} + \vec{u} \partial_{t_1}(\rho \vec{u}) - (\partial_{t_1}\rho)\vec{u}\vec{u} \quad (3.115)$$

Substituting Equation (3.115) into Equation (3.109),

$$\partial_{t_1}(\rho \vec{u}\vec{u} : \mathbf{Q}_i) = \mathbf{Q}_i : [\partial_{t_1}(\rho \vec{u})\vec{u} + \vec{u} \partial_{t_1}(\rho \vec{u}) - (\partial_{t_1}\rho)\vec{u}\vec{u}] \quad (3.116)$$

To recover the Navier-Stokes equation, we must neglect terms of order greater than  $\mathcal{O}(Ma^2)$  [30]. The first two terms on the RHS of Equation (3.116) present  $\mathcal{O}(Ma^2)$ ; however, as  $\partial_{t_1}\rho = -\vec{V}_1 \cdot \rho \vec{u}$  (see Equation (3.29)), the third term yields  $\mathcal{O}(Ma^3)$  and must be neglected. Therefore, Equation (3.116) is written as:

$$\partial_{t_1}(\rho \vec{u}\vec{u} : \mathbf{Q}_i) = \mathbf{Q}_i : [\partial_{t_1}(\rho \vec{u})\vec{u} + \vec{u} \partial_{t_1}(\rho \vec{u})] \quad (3.117)$$

Since  $\mathbf{Q}_i$  is a symmetric tensor, i.e.,  $Q_{i\alpha\beta} = Q_{i\beta\alpha}$ ,

$$\mathbf{Q}_i : \vec{u} \partial_{t_1}(\rho \vec{u}) = Q_{i\alpha\beta} u_\beta \partial_{t_1}(\rho u_\alpha) = Q_{i\beta\alpha} \partial_{t_1}(\rho u_\alpha) u_\beta = \mathbf{Q}_i : \partial_{t_1}(\rho \vec{u})\vec{u} \quad (3.118)$$

Hence, rewriting the last term of Equation (3.117),

$$\partial_{t_1}(\rho \vec{u}\vec{u} : \mathbf{Q}_i) = \mathbf{Q}_i : [\partial_{t_1}(\rho \vec{u})\vec{u} + \partial_{t_1}(\rho \vec{u})\vec{u}] \quad (3.119)$$

$$\partial_{t_1}(\rho \vec{u}\vec{u} : \mathbf{Q}_i) = \mathbf{Q}_i : 2 \partial_{t_1}(\rho \vec{u})\vec{u} = 2\mathbf{Q}_i : \partial_{t_1}(\rho \vec{u})\vec{u} \quad (3.120)$$

We know  $\partial_{t_1}(\rho\vec{u})$  from Equation (3.42). Substituting its expression into Equation (3.120),

$$\partial_{t_1}(\rho\vec{u}\vec{u} : \mathbf{Q}_i) = 2\mathbf{Q}_i : (-\vec{\nabla}_1 \cdot \boldsymbol{\pi}^{(0)} - c_s^2 \vec{\nabla}_1 \rho) \vec{u} \quad , \quad (3.121)$$

and substituting  $\boldsymbol{\pi}^{(0)}$  from Equation (3.82),

$$\partial_{t_1}(\rho\vec{u}\vec{u} : \mathbf{Q}_i) = 2\mathbf{Q}_i : (-\vec{\nabla}_1 \cdot \rho\vec{u}\vec{u} - c_s^2 \vec{\nabla}_1 \rho) \vec{u} \quad (3.122)$$

The first term inside the parenthesis on the RHS achieves  $\mathcal{O}(Ma^3)$  and must be neglected,

$$\partial_{t_1}(\rho\vec{u}\vec{u} : \mathbf{Q}_i) = -2c_s^2 \mathbf{Q}_i : (\vec{\nabla}_1 \rho) \vec{u} \quad (3.123)$$

Keep in mind that we are deducing  $f_i^{(1)}$  and, consequently,  $\boldsymbol{\pi}^{(1)}$ . Therefore, substituting Equation (3.123) into Equation (3.108),

$$f_i^{(1)} = -\tau\omega_i \left[ -\vec{\nabla}_1 \cdot \rho\vec{u} - \frac{\check{c}_i \vec{\nabla}_1 : \rho\vec{u}\vec{u}}{c_s^2} - \frac{2c_s^2 \mathbf{Q}_i : (\vec{\nabla}_1 \rho) \vec{u}}{2c_s^4} + \frac{\check{c}_i \check{c}_i : \vec{\nabla}_1(\rho\vec{u})}{c_s^2} + \frac{(\vec{\nabla}_1 \cdot \check{c}_i)(\rho\vec{u}\vec{u} : \mathbf{Q}_i)}{2c_s^4} \right] \quad (3.124)$$

Simplifying and factoring out  $\frac{1}{c_s^2}$ ,

$$f_i^{(1)} = \frac{\tau\omega_i}{c_s^2} \left[ c_s^2 \vec{\nabla}_1 \cdot \rho\vec{u} + \check{c}_i \vec{\nabla}_1 : \rho\vec{u}\vec{u} + \mathbf{Q}_i : (\vec{\nabla}_1 \rho) \vec{u} - \check{c}_i \check{c}_i : \vec{\nabla}_1(\rho\vec{u}) + \frac{(\vec{\nabla}_1 \cdot \check{c}_i)(\rho\vec{u}\vec{u} : \mathbf{Q}_i)}{2c_s^2} \right] \quad (3.125)$$

Next, we will simplify some terms of Equation (3.125). To avoid writing the same long term repeatedly and turning the equations longer, we define:

$$\chi = c_s^2 \vec{\nabla}_1 \cdot \rho \vec{u} + \mathbf{Q}_i : (\vec{\nabla}_1 \rho) \vec{u} - \vec{c}_i \vec{c}_i : \vec{\nabla}_1 (\rho \vec{u}) \quad (3.126)$$

Using Einstein notation,

$$\chi = c_s^2 (\partial_\alpha \rho u_\alpha) + Q_{i\alpha\beta} (\partial_\beta \rho) u_\alpha - c_{i\alpha} c_{i\beta} (\partial_\beta \rho u_\alpha) \quad , \quad (3.127)$$

and employing the product rule,

$$\chi = c_s^2 \rho \partial_\alpha u_\alpha + c_s^2 u_\alpha \partial_\alpha \rho + Q_{i\alpha\beta} (\partial_\beta \rho) u_\alpha - c_{i\alpha} c_{i\beta} \rho \partial_\beta u_\alpha - c_{i\alpha} c_{i\beta} u_\alpha \partial_\beta \rho \quad (3.128)$$

From Appendix B,  $\mathbf{Q}_i = \vec{c}_i \vec{c}_i - c_s^2 \mathbf{I}$ , i.e.,  $Q_{i\alpha\beta} = c_{i\alpha} c_{i\beta} - c_s^2 \delta_{\alpha\beta}$ ,

$$\begin{aligned} \chi = & c_s^2 \rho \partial_\alpha u_\alpha + c_s^2 u_\alpha \partial_\alpha \rho + c_{i\alpha} c_{i\beta} (\partial_\beta \rho) u_\alpha - c_s^2 \delta_{\alpha\beta} (\partial_\beta \rho) u_\alpha + \\ & - c_{i\alpha} c_{i\beta} \rho \partial_\beta u_\alpha - c_{i\alpha} c_{i\beta} u_\alpha \partial_\beta \rho \end{aligned} \quad (3.129)$$

The order of the variables has no significance because all the terms are scalar. In this way, canceling out the third and the last terms and employing the dot product  $\delta_{\alpha\beta} \partial_\beta = \partial_\alpha$ ,

$$\chi = c_s^2 \rho \partial_\alpha u_\alpha + c_s^2 u_\alpha \partial_\alpha \rho - c_s^2 (\partial_\alpha \rho) u_\alpha - c_{i\alpha} c_{i\beta} \rho \partial_\beta u_\alpha \quad (3.130)$$

Similarly, simplifying the second and third terms on the RHS,

$$\chi = c_s^2 \rho \partial_\alpha u_\alpha - c_{i\alpha} c_{i\beta} \rho \partial_\beta u_\alpha \quad (3.131)$$

Again, seeing that  $Q_{i\alpha\beta} = c_{i\alpha} c_{i\beta} - c_s^2 \delta_{\alpha\beta} \leftrightarrow c_{i\alpha} c_{i\beta} = Q_{i\alpha\beta} + c_s^2 \delta_{\alpha\beta}$ ,

$$\chi = c_s^2 \rho \partial_\alpha u_\alpha - Q_{i\alpha\beta} \rho \partial_\beta u_\alpha - c_s^2 \delta_{\alpha\beta} \rho \partial_\beta u_\alpha \quad (3.132)$$

Employing the dot product  $\delta_{\alpha\beta} \partial_\beta = \partial_\alpha$ ,

$$\chi = c_s^2 \rho \partial_\alpha u_\alpha - Q_{i\alpha\beta} \rho \partial_\beta u_\alpha - c_s^2 \rho \partial_\alpha u_\alpha \quad (3.133)$$

Canceling out the first and the last terms on the RHS, and returning to the direct tensor notation,

$$\chi = -Q_{i\alpha\beta} \rho \partial_\beta u_\alpha \quad (3.134)$$

$$\chi = -\mathbf{Q}_i : \rho(\vec{\nabla}_1 \vec{u}) \quad (3.135)$$

Substituting Equations (3.135) and (3.126) into Equation (3.125),

$$f_i^{(1)} = -\frac{\tau \omega_i}{c_s^2} \left[ \mathbf{Q}_i : \rho(\vec{\nabla}_1 \vec{u}) - \check{c}_i \vec{\nabla}_1 : \rho \vec{u} \vec{u} + \frac{(\vec{\nabla}_1 \cdot \check{c}_i)(\rho \vec{u} \vec{u} : \mathbf{Q}_i)}{2 c_s^2} \right] \quad (3.136)$$

As we know  $f_i^{(1)}$ , we can now calculate  $\boldsymbol{\pi}^{(1)}$  and further substitute it into Equation (3.69) to complete the Navier-Stokes equation. Hence, substituting Equation (3.136) into the definition of  $\boldsymbol{\pi}^{(1)}$ , i.e.,  $\boldsymbol{\pi}^{(1)} = \sum_i \check{c}_i \check{c}_i f_i^{(1)} - c_s^2 \mathbf{I} \sum_i f_i^{(1)}$  (see Appendix B),

$$\boldsymbol{\pi}^{(1)} = -\frac{\tau}{c_s^2} \sum_i \omega_i \left\{ \begin{aligned} &\check{c}_i \check{c}_i [\mathbf{Q}_i : \rho(\vec{\nabla}_1 \vec{u})] - \check{c}_i \check{c}_i (\check{c}_i \vec{\nabla}_1 : \rho \vec{u} \vec{u}) + \\ &+ \check{c}_i \check{c}_i \left[ \frac{(\vec{\nabla}_1 \cdot \check{c}_i)(\rho \vec{u} \vec{u} : \mathbf{Q}_i)}{2 c_s^2} \right] - c_s^2 \mathbf{I} \sum_i f_i^{(1)} \end{aligned} \right\} \quad (3.137)$$

From Equation (3.26),  $\sum_i f_i^{(1)} = 0$ . Then, the last term of Equation (3.137) is zero. Next, we will analyze the remained terms. Writing the first term on the RHS using Einstein notation,

$$\sum_i \omega_i \check{c}_i \check{c}_i [\mathbf{Q}_i : \rho(\vec{\nabla}_1 \vec{u})] = \sum_i \omega_i c_{i\alpha} c_{i\beta} [Q_{i\gamma\delta} \rho \partial_\delta u_\gamma] \quad (3.138)$$

From Appendix B,  $Q_{i\gamma\delta} = c_{i\gamma}c_{i\delta} - c_s^2\delta_{\gamma\delta}$ ,

$$\begin{aligned} \sum_i \omega_i \vec{c}_i \vec{c}_i [\mathbf{Q}_i : \rho(\vec{\nabla}_1 \vec{u})] &= \sum_i \omega_i c_{i\alpha} c_{i\beta} c_{i\gamma} c_{i\delta} \rho \partial_\delta u_\gamma + \\ &\quad - \sum_i \omega_i c_{i\alpha} c_{i\beta} c_s^2 \delta_{\gamma\delta} \rho \partial_\delta u_\gamma \end{aligned} \quad (3.139)$$

Since  $\rho \partial_\delta u_\gamma$  and  $c_s^2 \delta_{\gamma\delta}$  play any role in the summation,

$$\begin{aligned} \sum_i \omega_i \vec{c}_i \vec{c}_i [\mathbf{Q}_i : \rho(\vec{\nabla}_1 \vec{u})] &= \left( \sum_i \omega_i c_{i\alpha} c_{i\beta} c_{i\gamma} c_{i\delta} \right) \rho \partial_\delta u_\gamma + \\ &\quad - \left( \sum_i \omega_i c_{i\alpha} c_{i\beta} \right) c_s^2 \delta_{\gamma\delta} \rho \partial_\delta u_\gamma \end{aligned} \quad (3.140)$$

Recalling the isotropy conditions (see Appendix B),

$$\begin{aligned} \sum_i \omega_i \vec{c}_i \vec{c}_i [\mathbf{Q}_i : \rho(\vec{\nabla}_1 \vec{u})] &= c_s^4 (\delta_{\alpha\beta} \delta_{\gamma\delta} + \delta_{\alpha\gamma} \delta_{\beta\delta} + \delta_{\alpha\delta} \delta_{\beta\gamma}) \rho \partial_\delta u_\gamma + \\ &\quad - c_s^4 \delta_{\alpha\beta} \delta_{\gamma\delta} \rho \partial_\delta u_\gamma \end{aligned} \quad (3.141)$$

Simplifying,

$$\sum_i \omega_i \vec{c}_i \vec{c}_i [\mathbf{Q}_i : \rho(\vec{\nabla}_1 \vec{u})] = c_s^4 (\delta_{\alpha\gamma} \delta_{\beta\delta} + \delta_{\alpha\delta} \delta_{\beta\gamma}) \rho \partial_\delta u_\gamma \quad (3.142)$$

Since  $\delta_{\alpha\gamma} \delta_{\beta\delta} \partial_\delta u_\gamma = \partial_\beta u_\alpha$  and  $\delta_{\alpha\delta} \delta_{\beta\gamma} \partial_\delta u_\gamma = \partial_\alpha u_\beta$ ,

$$\sum_i \omega_i \vec{c}_i \vec{c}_i [\mathbf{Q}_i : \rho(\vec{\nabla}_1 \vec{u})] = c_s^4 \rho (\partial_\beta u_\alpha + \partial_\alpha u_\beta) \quad (3.143)$$

Note that, when we return to the direct tensor notation, to maintain the index consistency, we have to write the transpose of  $\vec{\nabla}_1 \vec{u}$ ,

$$\sum_{\mathbf{i}} \omega_i \vec{c}_i \vec{c}_i [\mathbf{Q}_i : \rho(\vec{\nabla}_1 \vec{u})] = \rho c_s^4 [(\vec{\nabla}_1 \vec{u})^T + \vec{\nabla}_1 \vec{u}] \quad (3.144)$$

Equation (3.144) simplifies the first term inside the summation of Equation (3.137). Now, we analyze the second term,

$$\sum_{\mathbf{i}} \omega_i \vec{c}_i \vec{c}_i (\vec{c}_i \vec{\nabla}_1 : \rho \vec{u} \vec{u}) = \sum_{\mathbf{i}} \omega_i c_{i\alpha} c_{i\beta} [c_{i\gamma} \partial_\delta (\rho u_\delta u_\gamma)] \quad (3.145)$$

As  $\partial_\delta (\rho u_\delta u_\gamma)$  plays any role in the summation,

$$\sum_{\mathbf{i}} \omega_i \vec{c}_i \vec{c}_i (\vec{c}_i \vec{\nabla}_1 : \rho \vec{u} \vec{u}) = \left( \sum_{\mathbf{i}} \omega_i c_{i\alpha} c_{i\beta} c_{i\gamma} \right) \partial_\delta (\rho u_\delta u_\gamma) \quad (3.146)$$

Recalling the isotropy conditions (see Appendix B), we realize the summation is zero,

$$\sum_{\mathbf{i}} \omega_i \vec{c}_i \vec{c}_i (\vec{c}_i \vec{\nabla}_1 : \rho \vec{u} \vec{u}) = \mathbf{0} \quad (3.147)$$

Equation (3.147) simplifies the second term inside the summation of Equation (3.137). Now, we analyze the third term,

$$\sum_{\mathbf{i}} \omega_i \vec{c}_i \vec{c}_i \left[ \frac{(\vec{\nabla}_1 \cdot \vec{c}_i)(\rho \vec{u} \vec{u} : \mathbf{Q}_i)}{2 c_s^2} \right] = \frac{1}{2 c_s^2} \sum_{\mathbf{i}} \omega_i c_{i\alpha} c_{i\beta} (\partial_\gamma c_{i\gamma} \rho u_\delta u_\epsilon Q_{\epsilon\delta}) \quad (3.148)$$

Since  $\partial_\gamma c_{i\gamma} = c_{i\gamma} \partial_\gamma \leftrightarrow \vec{\nabla}_1 \cdot \vec{c}_i = \vec{c}_i \cdot \vec{\nabla}_1$ ,

$$\sum_i \omega_i \vec{c}_i \vec{c}_i \left[ \frac{(\vec{\nabla}_1 \cdot \vec{c}_i)(\rho \vec{u} \vec{u} : \mathbf{Q}_i)}{2 c_s^2} \right] = \frac{\rho}{2 c_s^2} \left( \sum_i \omega_i c_{i\alpha} c_{i\beta} c_{i\gamma} \right) \partial_\gamma u_\delta u_\epsilon Q_{\epsilon\delta} \quad (3.149)$$

Recalling the isotropy conditions (see Appendix B),

$$\sum_i \omega_i \vec{c}_i \vec{c}_i \left[ \frac{(\vec{\nabla}_1 \cdot \vec{c}_i)(\rho \vec{u} \vec{u} : \mathbf{Q}_i)}{2 c_s^2} \right] = \mathbf{0} \quad (3.150)$$

Equation (3.150) simplifies the third term inside the summation of Equation (3.137). Now, we can substitute Equations (3.144), (3.147), and (3.150) into Equation (3.137),

$$\boldsymbol{\pi}^{(1)} = -\frac{\tau}{c_s^2} \rho c_s^4 \left[ (\vec{\nabla}_1 \vec{u})^T + \vec{\nabla}_1 \vec{u} \right] \quad (3.151)$$

Simplifying,

$$\boldsymbol{\pi}^{(1)} = -\rho \tau c_s^2 \left[ (\vec{\nabla}_1 \vec{u})^T + \vec{\nabla}_1 \vec{u} \right] \quad (3.152)$$

We finally calculated the tensors  $\boldsymbol{\pi}^{(0)}$ ,  $\mathbf{R}^{(0)}$  and  $\boldsymbol{\pi}^{(1)}$ , respectively given by Equations (3.82), (3.88), and (3.152). We can now substitute these tensors into Equation (3.69) to enforce the well-known Navier-Stokes equation to arise. Substituting, first, Equations (3.82) and (3.152) into Equation (3.69),

$$\begin{aligned} \partial_t \rho \vec{u} + \vec{\nabla} \cdot \left\{ \rho \vec{u} \vec{u} - \epsilon \rho \tau c_s^2 \left[ (\vec{\nabla}_1 \vec{u})^T + \vec{\nabla}_1 \vec{u} \right] \right\} + \left( 1 + \frac{\partial_t}{2} \right) c_s^2 \vec{\nabla} \rho + \\ + \frac{\epsilon}{2} \partial_{t_1} \vec{\nabla} \cdot \rho \vec{u} \vec{u} + \frac{1}{2} (\vec{\nabla} \vec{\nabla} : \mathbf{R}^{(0)}) = \vec{0} \end{aligned} \quad (3.153)$$

To factor out the divergence operation in most terms of Equation (3.153), we can write the last term in another form,

$$\vec{\nabla} \cdot \mathbf{R}^{(0)} = \vec{\nabla} \cdot (\vec{\nabla} \cdot \mathbf{R}^{(0)}) \quad (3.154)$$

Undoubtedly, we must substitute  $\mathbf{R}^{(0)}$  into Equation (3.154) and, consequently, Equation (3.153), yet. As  $\mathbf{R}^{(0)}$  is given by Equation (3.88), we calculate  $\vec{\nabla} \cdot \mathbf{R}^{(0)}$ ,

$$\vec{\nabla} \cdot \mathbf{R}^{(0)} = c_s^2 \partial_\gamma [(u_\gamma \delta_{\alpha\beta} + u_\beta \delta_{\alpha\gamma} + u_\alpha \delta_{\beta\gamma}) \rho] \quad (3.155)$$

Implementing the derivative  $\partial_\gamma$  in each term, and recalling that  $\partial_\gamma \delta_{\alpha\gamma} = \partial_\alpha$  and  $\partial_\gamma \delta_{\beta\gamma} = \partial_\beta$ ,

$$\vec{\nabla} \cdot \mathbf{R}^{(0)} = c_s^2 (\partial_\gamma \rho u_\gamma \delta_{\alpha\beta} + \partial_\alpha \rho u_\beta + \partial_\beta \rho u_\alpha) \quad (3.156)$$

Returning to the direct tensor notation,

$$\vec{\nabla} \cdot \mathbf{R}^{(0)} = c_s^2 \{ (\vec{\nabla} \cdot \rho \vec{u}) \mathbf{I} + \vec{\nabla}(\rho \vec{u}) + [\vec{\nabla}(\rho \vec{u})]^T \} \quad (3.157)$$

Substituting Equations (3.154) and (3.157) into Equation (3.153),

$$\begin{aligned} \partial_t \rho \vec{u} + \vec{\nabla} \cdot \{ \rho \vec{u} \vec{u} - \epsilon \rho \tau c_s^2 [ (\vec{\nabla}_1 \vec{u})^T + \vec{\nabla}_1 \vec{u} ] \} + \left( 1 + \frac{\partial_t}{2} \right) c_s^2 \vec{\nabla} \rho + \\ + \frac{\epsilon}{2} \partial_{t_1} \vec{\nabla} \cdot \rho \vec{u} \vec{u} + \frac{c_s^2}{2} \vec{\nabla} \cdot \{ (\vec{\nabla} \cdot \rho \vec{u}) \mathbf{I} + \vec{\nabla}(\rho \vec{u}) + [\vec{\nabla}(\rho \vec{u})]^T \} = \vec{0} \end{aligned} \quad (3.158)$$

Factoring out the divergence operation,

$$\begin{aligned} \partial_t \rho \vec{u} + \\ + \vec{\nabla} \cdot \left\{ \begin{aligned} & \rho \vec{u} \vec{u} - \epsilon \rho \tau c_s^2 [ (\vec{\nabla}_1 \vec{u})^T + \vec{\nabla}_1 \vec{u} ] + \left( 1 + \frac{\partial_t}{2} \right) c_s^2 \rho \mathbf{I} + \frac{\epsilon}{2} \partial_{t_1} \rho \vec{u} \vec{u} + \\ & + \frac{c_s^2}{2} [ (\vec{\nabla} \cdot \rho \vec{u}) \mathbf{I} + \vec{\nabla}(\rho \vec{u}) + (\vec{\nabla}(\rho \vec{u}))^T ] \end{aligned} \right\} = \vec{0} \end{aligned} \quad (3.159)$$

Substituting Equation (3.115) into Equation (3.159),

$$\begin{aligned} & \partial_t \rho \vec{u} + \\ & + \vec{\nabla} \cdot \left\{ \begin{aligned} & \rho \vec{u} \vec{u} - \epsilon \rho \tau c_s^2 \left[ (\vec{\nabla}_1 \vec{u})^T + \vec{\nabla}_1 \vec{u} \right] + \left( 1 + \frac{\partial_t}{2} \right) c_s^2 \rho \mathbf{I} + \frac{\epsilon}{2} \partial_{t_1} (\rho \vec{u}) \vec{u} + \\ & + \frac{\epsilon}{2} \vec{u} \partial_{t_1} (\rho \vec{u}) - \frac{\epsilon}{2} (\partial_{t_1} \rho) \vec{u} \vec{u} + \frac{c_s^2}{2} \left[ (\vec{\nabla} \cdot \rho \vec{u}) \mathbf{I} + \vec{\nabla} (\rho \vec{u}) + \right. \\ & \left. + (\vec{\nabla} (\rho \vec{u}))^T \right] \end{aligned} \right\} = \vec{0} \end{aligned} \quad (3.160)$$

From Equation (3.29), we know that  $\partial_{t_1} \rho = -\vec{\nabla}_1 \cdot \vec{u}$ . Hence,  $(\partial_{t_1} \rho) \vec{u} \vec{u}$  has  $\mathcal{O}(Ma^3)$  and must be neglected. Considering this and also substituting Equation (3.42) into  $\partial_{t_1} (\rho \vec{u})$ ,

$$\begin{aligned} & \partial_t \rho \vec{u} + \\ & + \vec{\nabla} \cdot \left\{ \begin{aligned} & \rho \vec{u} \vec{u} - \epsilon \rho \tau c_s^2 \left[ (\vec{\nabla}_1 \vec{u})^T + \vec{\nabla}_1 \vec{u} \right] + \left( 1 + \frac{\partial_t}{2} \right) c_s^2 \rho \mathbf{I} + \\ & + \frac{\epsilon}{2} (-c_s^2 \vec{\nabla}_1 \rho - \vec{\nabla}_1 \cdot \boldsymbol{\pi}^{(0)}) \vec{u} + \frac{\epsilon}{2} \vec{u} (-c_s^2 \vec{\nabla}_1 \rho - \vec{\nabla}_1 \cdot \boldsymbol{\pi}^{(0)}) + \\ & + \frac{c_s^2}{2} \left[ (\vec{\nabla} \cdot \rho \vec{u}) \mathbf{I} + \vec{\nabla} (\rho \vec{u}) + \right. \\ & \left. + (\vec{\nabla} (\rho \vec{u}))^T \right] \end{aligned} \right\} = \vec{0} \end{aligned} \quad (3.161)$$

From Equation (3.82),  $\boldsymbol{\pi}^{(0)} = \rho \vec{u} \vec{u}$ . Therefore,  $(\vec{\nabla}_1 \cdot \boldsymbol{\pi}^{(0)}) \vec{u}$  and  $\vec{u} (\vec{\nabla}_1 \cdot \boldsymbol{\pi}^{(0)})$  in Equation (3.161) have  $\mathcal{O}(Ma^3)$  and must be neglected,

$$\begin{aligned} & \partial_t \rho \vec{u} + \vec{\nabla} \cdot \left\{ \begin{aligned} & \rho \vec{u} \vec{u} - \epsilon \rho \tau c_s^2 \left[ (\vec{\nabla}_1 \vec{u})^T + \vec{\nabla}_1 \vec{u} \right] + \left( 1 + \frac{\partial_t}{2} \right) c_s^2 \rho \mathbf{I} + \\ & - \frac{\epsilon c_s^2}{2} \left[ (\vec{\nabla}_1 \rho) \vec{u} + \vec{u} \vec{\nabla}_1 \rho \right] + \frac{c_s^2}{2} \left[ (\vec{\nabla} \cdot \rho \vec{u}) \mathbf{I} + \vec{\nabla} (\rho \vec{u}) + \right. \\ & \left. + (\vec{\nabla} (\rho \vec{u}))^T \right] \end{aligned} \right\} = \vec{0} \end{aligned} \quad (3.162)$$

Substituting Equation (3.11) into Equation into Equation (3.162), we recover  $\vec{\nabla}$  operator,

$$\partial_t \rho \vec{u} + \vec{\nabla} \cdot \left\{ \begin{array}{l} \rho \vec{u} \vec{u} - \rho \tau c_s^2 [(\vec{\nabla} \vec{u})^T + \vec{\nabla} \vec{u}] + \left(1 + \frac{\partial_t}{2}\right) c_s^2 \rho \mathbf{I} + \\ -\frac{c_s^2}{2} [(\vec{\nabla} \rho) \vec{u} + \vec{u} \vec{\nabla} \rho] + \frac{c_s^2}{2} \left[ \begin{array}{l} (\vec{\nabla} \cdot \rho \vec{u}) \mathbf{I} + \vec{\nabla}(\rho \vec{u}) + \\ + (\vec{\nabla}(\rho \vec{u}))^T \end{array} \right] \end{array} \right\} = \vec{0} \quad (3.163)$$

If we look closely, we can see that the continuity equation appears in Equation (3.163). If we multiply Equation (3.59) (the continuity equation) by  $\frac{c_s^2}{2} \mathbf{I}$ ,

$$\frac{c_s^2}{2} \partial_t \rho \mathbf{I} + \frac{c_s^2}{2} (\vec{\nabla} \cdot \rho \vec{u}) \mathbf{I} = 0 \quad (3.164)$$

Substituting Equation (3.164) into Equation (3.163),

$$\partial_t \rho \vec{u} + \vec{\nabla} \cdot \left\{ \begin{array}{l} \rho \vec{u} \vec{u} - \rho \tau c_s^2 [(\vec{\nabla} \vec{u})^T + \vec{\nabla} \vec{u}] + c_s^2 \rho \mathbf{I} + \\ -\frac{c_s^2}{2} [(\vec{\nabla} \rho) \vec{u} + \vec{u} \vec{\nabla} \rho] + \frac{c_s^2}{2} \left[ \vec{\nabla}(\rho \vec{u}) + (\vec{\nabla}(\rho \vec{u}))^T \right] \end{array} \right\} = \vec{0} \quad (3.165)$$

Factoring out  $\frac{c_s^2}{2}$ ,

$$\partial_t \rho \vec{u} + \vec{\nabla} \cdot \left\{ \begin{array}{l} \rho \vec{u} \vec{u} - \rho \tau c_s^2 [(\vec{\nabla} \vec{u})^T + \vec{\nabla} \vec{u}] + c_s^2 \rho \mathbf{I} + \\ + \frac{c_s^2}{2} \left[ -(\vec{\nabla} \rho) \vec{u} - \vec{u} \vec{\nabla} \rho + \vec{\nabla}(\rho \vec{u}) + (\vec{\nabla}(\rho \vec{u}))^T \right] \end{array} \right\} = \vec{0} \quad (3.166)$$

We can reduce the summation inside the brackets. Again, to avoid writing the same lengthy-term repeatedly and turning the equations longer, we define:

$$\chi' = -(\vec{\nabla} \rho) \vec{u} - \vec{u} \vec{\nabla} \rho + \vec{\nabla}(\rho \vec{u}) + (\vec{\nabla}(\rho \vec{u}))^T \quad (3.167)$$

Using Einstein summation convention to rewrite Equation (3.167),

$$\chi' = -(\partial_\alpha \rho)u_\beta - u_\alpha \partial_\beta \rho + \partial_\alpha(\rho u_\beta) + \partial_\beta(\rho u_\alpha) , \quad (3.168)$$

employing the product rule,

$$\chi' = -(\partial_\alpha \rho)u_\beta - u_\alpha \partial_\beta \rho + \rho \partial_\alpha u_\beta + (\partial_\alpha \rho)u_\beta + (\partial_\beta \rho)u_\alpha + \rho \partial_\beta u_\alpha , \quad (3.169)$$

and simplifying,

$$\chi' = \rho \partial_\alpha u_\beta + \rho \partial_\beta u_\alpha \quad (3.170)$$

Returning to the direct tensor notation,

$$\chi' = \rho \left[ \vec{\nabla} \vec{u} + (\vec{\nabla} \vec{u})^T \right] \quad (3.171)$$

Substituting Equations (3.167) and (3.171) into Equation (3.166),

$$\partial_t \rho \vec{u} + \vec{\nabla} \cdot \left\{ \rho \vec{u} \vec{u} - \rho \tau c_s^2 \left[ \vec{\nabla} \vec{u} + (\vec{\nabla} \vec{u})^T \right] + c_s^2 \rho \mathbf{I} + \frac{c_s^2}{2} \rho \left[ \vec{\nabla} \vec{u} + (\vec{\nabla} \vec{u})^T \right] \right\} = \vec{0} \quad (3.172)$$

Factoring out  $\vec{\nabla} \vec{u} + (\vec{\nabla} \vec{u})^T$ ,

$$\partial_t \rho \vec{u} + \vec{\nabla} \cdot \left\{ \rho \vec{u} \vec{u} + \left( \frac{\rho c_s^2}{2} - \rho \tau c_s^2 \right) \left[ \vec{\nabla} \vec{u} + (\vec{\nabla} \vec{u})^T \right] + \rho c_s^2 \mathbf{I} \right\} = \vec{0} \quad (3.173)$$

Factoring out  $\rho c_s^2$ ,

$$\partial_t \rho \vec{u} + \vec{\nabla} \cdot \left\{ \rho \vec{u} \vec{u} + \left( \frac{1}{2} - \tau \right) \rho c_s^2 \left[ \vec{\nabla} \vec{u} + (\vec{\nabla} \vec{u})^T \right] + \rho c_s^2 \mathbf{I} \right\} = \vec{0} \quad (3.174)$$

In LBM, the pressure for ideal gases is  $p = \rho c_s^2$ . Introducing it into Equation (3.174),

$$\partial_t \rho \vec{u} = -\vec{\nabla} \cdot \left\{ \rho \vec{u} \vec{u} - \left( \tau - \frac{1}{2} \right) \rho c_s^2 \left[ \vec{\nabla} \vec{u} + (\vec{\nabla} \vec{u})^T \right] + p \mathbf{I} \right\} = \vec{0} \quad (3.175)$$

Hence, we finally recovered the Navier-Stokes equation in its well-known form, i.e., Equation (3.175), for only small values of  $Ma$  (we neglected terms with order equals to or greater than  $\mathcal{O}(Ma^3)$ ). According to Bird *et al.* [24], in a system with a gravitational force field, the motion equation is:

$$\partial_t \rho \vec{u} = -\vec{\nabla} \cdot \rho \vec{u} \vec{u} - \vec{\nabla} p - \vec{\nabla} \cdot \mathbf{S} + \rho \vec{g} = \vec{0} , \quad (3.176)$$

where  $\vec{g}$  is the gravitational acceleration and  $\mathbf{S}$  is the deviatoric stress tensor.

We can compare our recovered equation, i.e., Equation (3.175), with the classical Navier-Stokes equation, i.e., Equation (3.176). The first, second, and third terms of Equation (3.175) are also in Equation (3.176). Since we started this deduction neglecting external forces (see Equation (3.1)), we must neglect  $\rho \vec{g}$  in Equation (3.176). Hence, comparing the remained terms,

$$-\vec{\nabla} \cdot \mathbf{S} = \vec{\nabla} \cdot \left\{ \left( \tau - \frac{1}{2} \right) \rho c_s^2 \left[ \vec{\nabla} \vec{u} + (\vec{\nabla} \vec{u})^T \right] \right\} \quad (3.177)$$

$$\mathbf{S} = - \left( \tau - \frac{1}{2} \right) \rho c_s^2 \left[ \vec{\nabla} \vec{u} + (\vec{\nabla} \vec{u})^T \right] \quad (3.178)$$

The stress tensor describes the distortion of a body and is defined as [24],

$$\mathbf{S} = -\mu \left[ \vec{\nabla} \vec{u} + (\vec{\nabla} \vec{u})^T \right] + \left( \frac{2}{3} \mu - \kappa \right) (\vec{\nabla} \cdot \vec{u}) \mathbf{I} , \quad (3.179)$$

where  $\mu$  and  $\kappa$  are, respectively, the shear and dilatational viscosities. From the continuity equation, we know that  $\vec{\nabla} \cdot \vec{u} = 0$  for incompressible flow. Then,

$$\mathbf{s} = -\mu \left[ \vec{\nabla} \vec{u} + (\vec{\nabla} \vec{u})^T \right] \quad (3.180)$$

Substituting Equation (3.180) into Equation (3.178),

$$-\mu \left[ \vec{\nabla} \vec{u} + (\vec{\nabla} \vec{u})^T \right] = -\left( \tau - \frac{1}{2} \right) \rho c_s^2 \left[ \vec{\nabla} \vec{u} + (\vec{\nabla} \vec{u})^T \right] , \quad (3.181)$$

and simplifying,

$$\mu = \left( \tau - \frac{1}{2} \right) \rho c_s^2 \quad (3.182)$$

Seeing that the kinematic viscosity is  $\nu = \mu/\rho$ , then,

$$\nu = \left( \tau - \frac{1}{2} \right) c_s^2$$
(3.183)

Equation (3.183) reveals that both physical and numerical frameworks are connected to only one parameter: the relaxation time, which links the mesoscale to the real fluid property (macroscopic value) when  $\delta t = 1$ . Hence, the relaxation time is associated with stability: values around  $\tau \sim 0.5$  may induce numerical instabilities since it approaches unphysical viscosities ( $\mu \leq 0$ ). For any interval of lattice time  $\delta t$ , Equation (2.30) is recovered instead.

We conclude Equation (3.175) recovers the Navier-Stokes equation for the BGK collision operator and small  $Ma$  (i.e., incompressible flow). Other collision operators, such as MRT, also recover the Navier-Stokes equation, but with a different format from Equation (3.174). Because of the Mach number influence in the deduction,  $Ma$  is understood as a dimensionless number that monitors the LBM accuracy: for higher  $Ma$ , the compressibility effects that arise deteriorate the simulation accuracy.

Note that the Navier-Stokes equation is recovered with a second-order approximation in  $f_i$  expansion, i.e., in Equation (3.13). Other relevant equations originate from different order expansions instead. For instance, the Euler and the Burnett equations emerge, respectively, when zeroth- and second-order approximations are considered. Both equations represent the momentum conservation, but the former is for an ideal fluid ( $\mu = 0$ ) and the latter for higher Knudsen numbers (e.g., ultrasonic sound propagation) [21]. On the other hand, it is only necessary a zeroth-order approximation in  $f_i$  expansion to recover the continuity equation.

The Chapman-Enskog proves to be a helpful method to check for LBM consistency. Still, one can also handle this analysis with other methods, such as the Maxwellian iteration, the regular error, and Hermite expansions, without losing information. Nevertheless, the Chapman-Enskog is the most used method in the literature.

# Chapter 4

## Computational aspects of LBM

The evidence of the LBM consolidation in the transport phenomena community is the amount of several available open-source codes (e.g., Palabos [56], OpenLB [57], Taxila LBM [58], and waLBerla [59]) and even commercial software (e.g., SIMULIA's PowerFLOW [60], and NUMECA's OMNIS/LB [61]) that implement LBM. Through commands modified exceptionally for this method, they improve the user programming, enhance productivity, efficiency, and performance, facilitate parallelization if desired, and support multidisciplinary investigations (e.g., thermal and multiphase combined flows). Although they present various LB models already implemented and validated, we write our own codes using C/C++ language in this work to ensure we understand the LB concepts entirely. We summarize a general LBM algorithm in Figure 7, the foundation of our codes. Hence, this chapter is a valuable starting point to demonstrate for LBM beginners how to use the theory equations presented in Chapters 2 and 3. Here, we validate our computational LBM implementation and highlight its main features. For this purpose, we perform two frequent

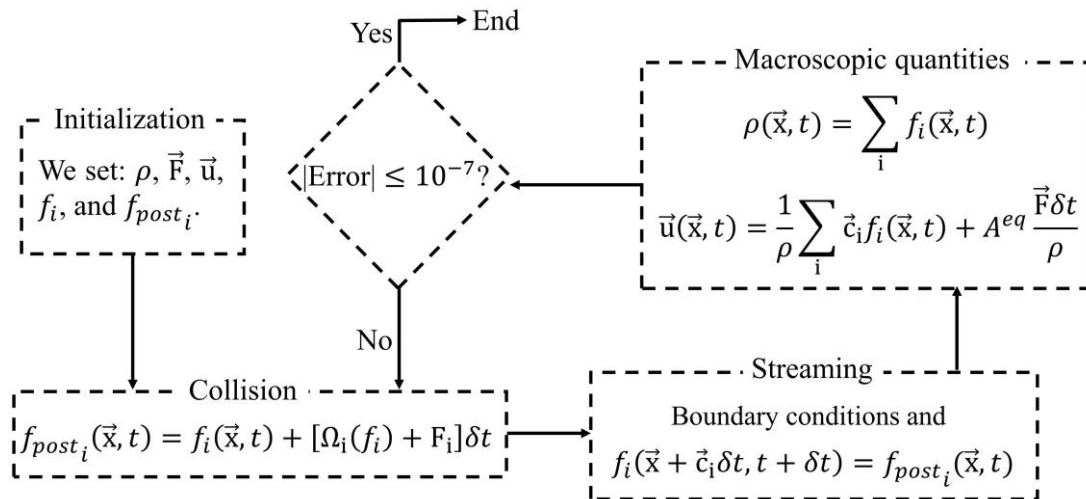


Figure 7: General diagram for an LBM code. Sections 2.3 to 2.5 cover the implementations of  $\Omega_i(f_i)$ ,  $F_i$  and boundary conditions. The error is calculated as the difference of the updated variable (e.g., density and velocity) from its value at a previous distant iteration.

examples of the LBM application: the Couette (Section 4.1) and the square-cavity flows (Section 4.2).

## 4.1 Couette flow

In the Couette flow problem, a fluid is confined between a top and a bottom walls and presents zero initial velocity. The top wall ensures the flow since it moves to the right with a constant horizontal velocity  $\vec{u}_w$ , as shown in Figure 8. After the system reaches the steady state, the velocity profile  $u_x(y)$  achieved is [62]:

$$u_x(y) = \frac{y}{h} |\vec{u}_w| , \quad (4.1)$$

where  $y$  is the vertical position,  $h$  is the height between the walls, and  $L$  is the length from the inlet to the outlet.

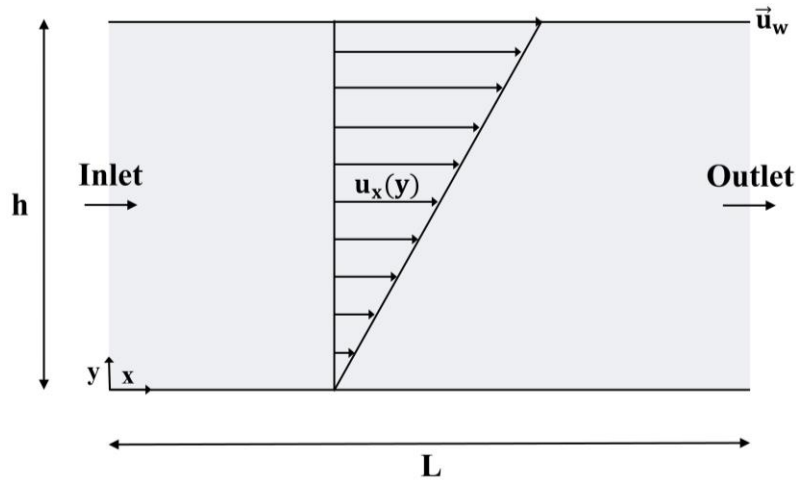


Figure 8: Illustrative sketch of the Couette flow benchmark, where the blue region and the arrows represent, respectively, the fluid and the velocity profile.

Assume, for illustration, that the fluid is water, the Reynolds number is  $Re = 1000$ , and the geometry specification are  $h = 0.01$  m and  $L = 5h$ . Then  $|\vec{u}_w|$  can be calculated for the Couette flow benchmark as:

$$Re = \frac{L|\vec{u}_w|}{\nu} , \quad (4.2)$$

where  $\nu$  is the kinematic viscosity, which is  $\nu = 10^{-6}$  m<sup>2</sup>/s for water at 20°C.

However, a proper implementation of the LBM requires a careful unit conversion of the physical problem specifications (originally in the International System of Units in this case) into lattice units (l.u.). This conversion is usually performed through similarity scaling. For instance, the ratio between the real density ( $\rho^R$ ) and the lattice density ( $\rho^L$ ) determines the density conversion factor  $(C_f)^{\rho}$ :

$$(C_f)^{\rho} = \frac{\rho^R}{\rho^L} . \quad (4.3)$$

The density in LBM is usually specified around one ( $\rho^L = 1$ ) to ensure stability, which results  $(C_f)^{\rho} = \rho^R$ . For water ( $\rho = 1000$  kg/m<sup>3</sup>),  $(C_f)^{\rho} = 1000$  kg/m<sup>3</sup>.

Notice the proportion of the domain is determined in Figure 8, which implies that one only needs to determine  $h$  or  $L$  in the LB implementation. However, as covered in Chapter 2, the lattice is discretely composed of nodes, and  $(\delta x)^L$  is generally fixed as  $(\delta x)^L = 1$ . Thus, it is more straightforward to set the number of nodes in the horizontal ( $N_x$ ) or vertical ( $N_y$ ) directions.

There are two walls in the vertical direction. We place the top wall at row = 1 (solid nodes) and the bottom wall at row =  $N_y$  (solid nodes). Figure 9 helps the visualization. The first row/column of the arrays and matrices is identified as position zero in C/C++ language, differently to, e.g., MATLAB. In other words, we ignored row = 0 for convenience. Consequently, there are  $N_y + 1$  nodes over the vertical direction (considering row = 0), but only  $N_y - 2$  fluid nodes (discarding row = 0 and the walls). On the other hand, there are no walls in the horizontal direction. Then, the fluid nodes stand from column = 1 to column =  $N_x$ . Consequently, there are  $N_x$  fluid nodes over the horizontal direction.

A given variable that presents a particular value for each domain position is a matrix in the implementation. Note that the call of a matrix in the C/C++ language is

matrix\_name[row][column]. For instance, the dimension of the density matrix is rho[Ny + 1][Nx + 1] but their values are only calculated at  $1 < \text{row} < N_y$  and  $1 \leq \text{column} \leq N_x$ .

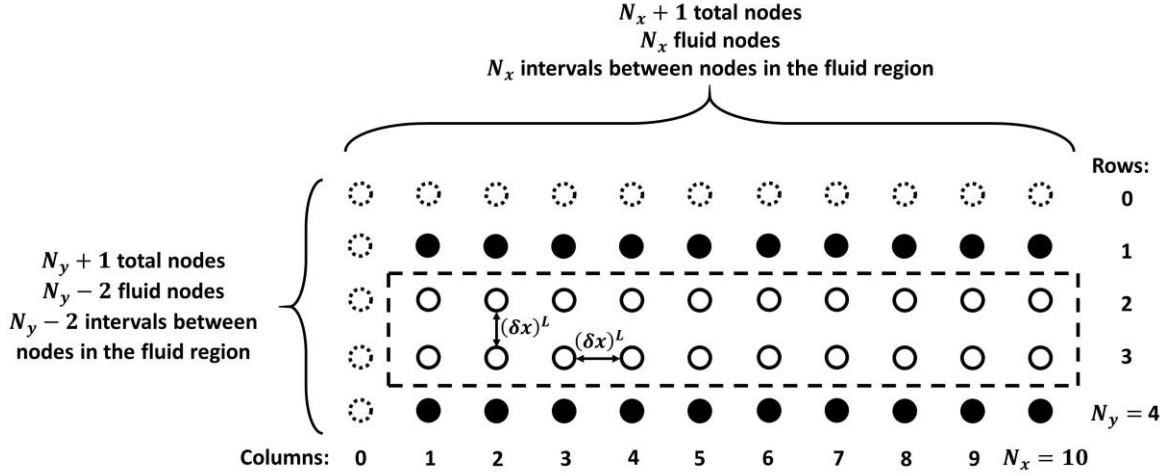


Figure 9: Domain representation for the Couette flow problem considered when  $N_y = 4$ . The solid, fluid and ignored nodes are, respectively, the black, white and dashed nodes. The dashed lines (--) are the computational boundary in the link-wise approach.

If one specifies  $N_y = 100$  nodes,  $N_x$  is calculated from similarity. Based on Equation (4.3), the conversion factor for distances  $(C_f)^d$  is:

$$(C_f)^d = \frac{h}{(N_y - 2)(\delta x)^L} . \quad (4.4)$$

Note that  $(N_y - 2)(\delta x)^L$  is written in the denominator because one must compare distances rather than node quantities. As discussed above, there are  $N_y - 2$  fluid nodes over the vertical direction, which leads to  $N_y - 3$  intervals between fluid nodes, one interval between the fluid node and the top wall, and one interval between the fluid node and the bottom wall. But we intend to incorporate the link-wise approach (Section 2.4.1), which places the wall midway the solid and fluid nodes. Hence, there is, actually, 0.5 interval between the fluid node and each wall. As a result, the total number of intervals between nodes

is  $N_y - 3 + 0.5 + 0.5$ , i.e., there are  $N_y - 2$  intervals over the vertical direction. Then,  $N_y - 2$  must be multiplied by the length of each interval  $(\delta x)^L$  to allow the distance comparison.

Similarly,  $(C_f)^d$  can also be written using  $L$ :

$$(C_f)^d = \frac{L}{N_x(\delta x)^L} . \quad (4.5)$$

Matching Equations (4.4) and (4.5),

$$N_x = \frac{L(N_y - 2)}{h} . \quad (4.6)$$

Stipulating  $N_y = 100$  nodes, Equation (4.6) achieves  $N_x = 490$  nodes. Categorically for this benchmark, one could implement a less refined lattice without losing accuracy because the Couette flow has linear dependence. For the same reason, the problem is independent of the relaxation time, corroborating to carry out the BGK model.

Therefore, LBM-BGK simulations were employed with  $\tau = 0.6$  and  $\tau = 1.0$ , which provides, respectively,  $\nu = 0.033$  l.u. and  $\nu = 0.167$  l.u. from Equation (2.30). As suggested in Figure 7, the first step in the implementation is to initialize all the variables. The macroscopic velocities in the x-direction ( $u_x[\text{row}][\text{column}]$ ) and in the y-direction ( $u_y[\text{row}][\text{column}]$ ) are zero for all fluid nodes ( $1 < \text{row} < N_y$  and  $1 \leq \text{column} \leq N_x$ ). For the same range, the initial density is  $\rho[\text{row}][\text{column}] = 1.0$ .

Notice that the initial values of the probability distribution function  $f[\text{row}][\text{column}][\text{direction}]$  are required to conduct the collision step and may impact the following calculations. This influence is only evidenced in transient issues or problems that depend on the initial conditions [21], which is not the case for the Couette flow problem.

However, to initialize  $f[\text{row}][\text{column}][\text{direction}]$  consistently with transient problems is an LBM programming good practice. In this case, the equilibrium scheme is a frequent initialization, in which  $f[\text{row}][\text{column}][\text{direction}] = f_{eq}$  for all fluid nodes. Alternatively, one can implement the (i) non-equilibrium scheme, through which the non-equilibrium part is also inserted in the initialization [63], or the (ii) iterative method, which

resolves the Poisson equation to initialize  $f[\text{row}][\text{column}][\text{direction}]$  consistently with the velocity field [64, 65].

As displayed in Figure 10, the equilibrium distribution function  $feq$  is computed from Equation (2.12) using the initial densities and velocities for the equilibrium scheme.

```
//First collision (BGK model)
for(row = 2; row < Ny; row++){
  for(column = 1; column <= Nx; column++){
    for(direction = 0; direction < 9; direction++){
      cu = cx[direction] * ux[row][column] + cy[direction] * uy[row][column]; // Dot product
      U2 = ux[row][column] * ux[row][column] + uy[row][column] * uy[row][column]; // Dot product
      feq = w[direction] * rho[row][column] * (1 + 3*cu + 4.5*cu*cu - 1.5*U2); // Equation (2.12)
      f[row][column][direction] = feq; // Equilibrium scheme
    }
  }
}
```

Figure 10: Initialization of the probability distribution function employing the equilibrium scheme, in which  $cu \equiv \vec{c}_i \cdot \vec{u}$ ,  $U2 \equiv \vec{u} \cdot \vec{u}$ ,  $feq \equiv f_i^{eq}$ , and  $w \equiv \omega_i$ . The discrete velocities  $cx[\text{direction}]$  and  $cy[\text{direction}]$  are found in Equation (2.14).

Note that  $f[\text{row}][\text{column}][\text{direction}]$ , different from the density and velocities, is a three-dimensional array because it also contemplates the lattice directions  $i$  (Section 2.2). Since  $0 \leq \text{direction} \leq 8$  for the D2Q9 model,  $f[\text{row}][\text{column}][\text{direction}]$  is composed of nine two-dimensional arrays with individual dimensions of  $N_y + 1 \times N_x + 1$ .

Contrarily, a proper initialization scheme for  $f\_post[\text{row}][\text{column}][\text{direction}]$  is unnecessary because the LBE calculates  $f_{post_i}$  in the collision step. However, to declare and initialize all the variables as zero, including  $f\_post[\text{row}][\text{column}][\text{direction}]$ , is a good programming practice. This habit guarantees the variables will not collect garbage values and avoids the algorithm having undefined behavior.

The collision is measured in Figure 11. The difference from Figure 10 is that Figure 11 evaluates the LBE to calculate  $f\_post[\text{row}][\text{column}][\text{direction}]$ . The collision step becomes, then, a straightforward way to initialize  $f_{post_i}$  consistently with  $f_i$ , and with the velocity and density fields. Note that one can write  $\omega$  ( $\equiv 1/\tau$ ) rather than  $\tau$  ( $\equiv \tau$ ) in the LBE to improve the time performance of the algorithm preventing undesirable divisions.

```

//Collision step with BGK model
for(row = 2; row < Ny; row++){
  for(column = 1; column <= Nx; column++){
    for(direction = 0; direction < 9; direction++){
      cu = cx[direction] * ux[row][column] + cy[direction] * uy[row][column]; // Dot product
      U2 = ux[row][column] * ux[row][column] + uy[row][column] * uy[row][column]; // Dot product
      feq = w[direction] * rho[row][column] * (1 + 3*cu + 4.5*cu*cu - 1.5*U2); // Equation (2.12)

      // Equation (2.29)
      f_post[row][column][direction] = f[row][column][direction] - ((f[row][column][direction] - feq) * omega);
    }
  }
}

```

Figure 11: BGK collision step, in which  $cu \equiv \vec{c}_i \cdot \vec{u}$ ,  $U2 \equiv \vec{u} \cdot \vec{u}$ ,  $feq \equiv f_i^{eq}$ ,  $w \equiv \omega_i$ , and  $\omega \equiv 1/\tau$ . The discrete velocities  $cx[direction]$  and  $cy[direction]$  are found in Equation (2.14).

According to Figure 7, the next step is the streaming, in which  $f_i$  propagates through the nodes as a result of the collisions performed. Since D2Q9 model was implemented,  $f_i$  is allowed to propagate to nine different neighboring nodes. To track which neighboring node at position  $(rho\_new, column\_new)$  is chosen depending on the value of  $i$  (or direction), one must recall the definition of the velocity magnitudes, i.e.,  $c_x = (\delta x)^L / (\delta t)^L = (column\_new - column) / \delta t$  and  $c_y = (row - row\_new) / \delta t$ , and, then, calculate  $column\_new$  and  $row\_new$  as follows:

$$column\_new = column + cx[direction] , \quad (4.7)$$

$$row\_new = row - cy[direction] , \quad (4.8)$$

where the sign before  $\vec{c}_i$  is intentionally inverted because the identification of the matrix rows increases downwards while  $c_y$  is negative for this direction.

In Figure 12, the periodic conditions are implemented at  $column = 1$  and  $column = N_x$  and the halfway bounce-back scheme at  $row = 2$  and  $row = N_y - 1$ . The distribution function, which always originates from a fluid node, is exposed to five different situations: (i)  $f_i$  propagates and hits the moving wall at  $row\_new = 1$  (Equation (2.44) is implemented), (ii)  $f_i$  propagates and hits the bottom wall at  $row\_new = N_y$  (Equation (2.45) is implemented), (iii)  $f_i$  propagates and arrives at an ignored node at  $column\_new = N_x + 1$  (Equation (2.50) is implemented), (iv)  $f_i$  propagates and arrives at an ignored node at

column\_new = 0 (Equation (2.51) is implemented), and (v)  $f_i$  propagates to other fluid node (Equation (2.16) is implemented).

```

//Streaming step
for(row = 2; row < Ny; row++){
  for(column = 1; column <= Nx; column++){
    for(direction = 0; direction < 9; direction++){

      column_new = column + cx[direction]; //Equation (3.7)
      row_new = row - cy[direction];      //Equation (3.8)

      if(row_new == 1 || row_new == Ny){

        switch(row_new){
          case 1:
            //Equation (2.44)
            f[row][column][rc[direction]] = f_post[row][column][direction]
              - 6 * w[direction] * rho[row][column] * cx[direction] * uw;
            break;

          case Ny:
            f[row][column][rc[direction]] = f_post[row][column][direction]; //Equation (2.45)
            break;
          }

        }else{

          switch(column_new){
            case Nx+1:
              f[row_new][1][direction] = f_post[row][column][direction]; //Equation (2.50)
              break;

            case 0:
              f[row_new][Nx][direction] = f_post[row][column][direction]; //Equation (2.51)
              break;

            default :
              f[row_new][column_new][direction] = f_post[row][column][direction]; //Equation (2.16)
              break;
            }

          }

        }

      }
    }
  }
}

```

Figure 12: Streaming step calculation. The discrete velocities  $cx[direction]$  and  $cy[direction]$  are found in Equation (2.14).

When  $f_i$  propagates from a fluid node to a solid one, its direction changes due to the solid boundary condition (Section 2.4.1). As an example,  $f_4$  at a node  $(N_y - 1, \text{column})$  hits the wall at  $(N_y - 0.5, \text{column})$ , becomes  $f_2$  and propagates back to the original node at  $(N_y - 1, \text{column})$ . To capture this change, the halfway bounce-back scheme is implemented in Figure 12 with an extra variable, `rc[direction]`, which only recalculates the direction of  $f_i$  when the algorithm requests the boundary condition. The variable `rc[direction]` is declared as:

$$\text{int rc}[9] = \{0, 3, 4, 1, 2, 7, 8, 5, 6\}; \quad (4.9)$$

and it is equivalent to the values of  $\bar{i}$  in Chapter 2.

The macroscopic quantities are updated after the streaming step. One may apply “for loops” to calculate the densities and velocities in Equations (2.22) and (2.23), but one can simplify this by writing the equations in their complete form, as displayed in Figure 13. Through this description, the density is measured at once, and the algorithm is released to perform various irrelevant  $\vec{c}_i f_i$  multiplications since the  $\vec{c}_i$  values are directly inserted in the velocity calculations.

```
//Macroscopic quantities computation
for(row = 2; row < Ny; row++){
  for(column = 1; column <= Nx; column++){

    // Equation (2.22)
    rho[row][column] = f[row][column][0] + f[row][column][1] + f[row][column][2] + f[row][column][3]
      + f[row][column][4] + f[row][column][5] + f[row][column][6] + f[row][column][7]
      + f[row][column][8];

    // Equation (2.23)
    ux[row][column] = (f[row][column][1] + f[row][column][5] + f[row][column][8]
      - f[row][column][3] - f[row][column][6] - f[row][column][7]) / rho[row][column];
    uy[row][column] = (f[row][column][2] + f[row][column][5] + f[row][column][6]
      - f[row][column][4] - f[row][column][7] - f[row][column][8]) / rho[row][column];

  }
}
```

Figure 13: Macroscopic quantities calculation through Equations (2.22) and (2.23). The discrete velocities `cx[direction]` and `cy[direction]` are already considered for  $\delta x = 1$  and  $\delta t = 1$ .

At this moment, the data of this time step can be exported to the hard disk if desired. Next, the algorithm returns to the collision step (Figure 11) to update  $f_{post_i}$  using the newest macroscopic densities and velocities. The algorithm proceeds to conform to Figure 7 until the macroscopic quantities converge.

Figure 14 compares Equation (4.1) with the velocity profile obtained in the post-processing employing our LBM code. The velocities agree well with the analytical profile both for  $\tau = 0.6$  and  $\tau = 1.0$ . As expected, the Couette flow is  $\tau$ -independent because it provides linear spatial dependence.

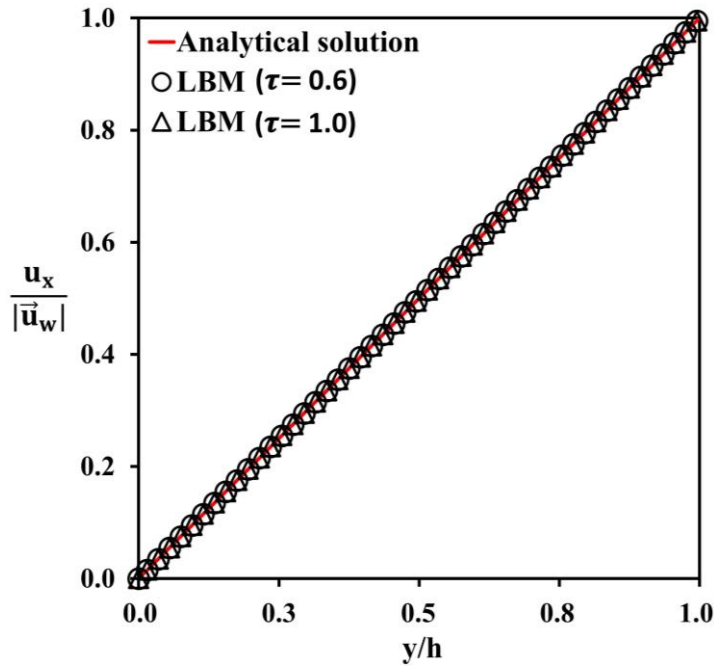


Figure 14: Normalized velocity profile of the Couette flow for  $|\vec{u}_w| = 0.067$  l.u. ( $\tau = 0.6$ ) and  $|\vec{u}_w| = 0.333$  l.u. ( $\tau = 1.0$ ). In both cases,  $Ma = |\vec{u}_w|/c_s < 0.3$ , which ensures accuracy.

Since the link-wise approach was employed, one can only visualize the accurate agreement in Figure 14 if the match between the lattice location and its velocity is evaluated correctly. Based on the definition of the conversion factor, the physical spatial increment  $(\delta x)^R$  between each node is:

$$(\delta x)^R = (C_f)^d (\delta x)^L = \frac{h}{N_y - 2} = \frac{L}{N_x} . \quad (4.10)$$

Hence,  $(\delta x)^R = 0.102$  mm in our simulations. Exemplifying, the physical location of the velocity at row = 2 is  $h - 0.5(\delta x)^R$ , and at row = 3 is  $h - 1.5(\delta x)^R$ . Generalizing, at a given row (for  $1 < \text{row} < N_y$ ), the physical location of the velocity is  $h - (\text{row} - 1.5)(\delta x)^R$ . If this relationship is ignored, Figure 14 will present a deficient agreement.

If desired, the conversion factor of the velocity  $(C_f)^u$  can be promptly evaluated. First, in this case, the conversion factor of the kinematic viscosity is calculated as:

$$(C_f)^v = \frac{\nu^R}{\nu^L} . \quad (4.11)$$

Since  $(C_f)^u$  has a dimension that can be written as a function of the dimensions of  $(C_f)^d$  and  $(C_f)^v$ , one can compute  $(C_f)^u$  as:

$$(C_f)^u = \frac{(C_f)^v}{(C_f)^d} . \quad (4.12)$$

For  $\tau = 0.6$ ,  $(C_f)^u = 0.294$ , and for  $\tau = 1.0$ ,  $(C_f)^u = 0.059$ . Then, the physical velocities are calculated through  $(u_x)^R = (C_f)^u (u_x)^L$ .

## 4.2 Square-cavity flow

In the square-cavity flow benchmark, a cubic region composed of solid walls with length  $L$  confines the fluid, as illustrated in Figure 15(a). Similarly to the Couette flow, the fluid with initial zero velocity gains momentum from the top wall, which is moving to the right with constant velocity  $\vec{u}_w$ . The proposition to construct the lattice in Figure 15(b) is the same as in Section 4.1. Still, differently, there are solid walls on the lateral sides.

Again, the physical parameters of the real problem are specified first: simulations of water at  $20^\circ\text{C}$  ( $\nu = 10^{-6} \text{ m}^2/\text{s}$ ) were carried out for  $L = 1 \text{ m}$ ,  $Re = 400$ , and  $Re = 5000$ . The velocity of the moving wall is calculated through Equation (4.2). The square domain ( $N_x = N_y = N$ ) consists of  $N + 1 \times N + 1$  total nodes. By setting the walls as Figure 15(b) suggests, the range of the fluid nodes is  $1 < \text{row} < N_y$  and  $1 < \text{column} < N_x$ .

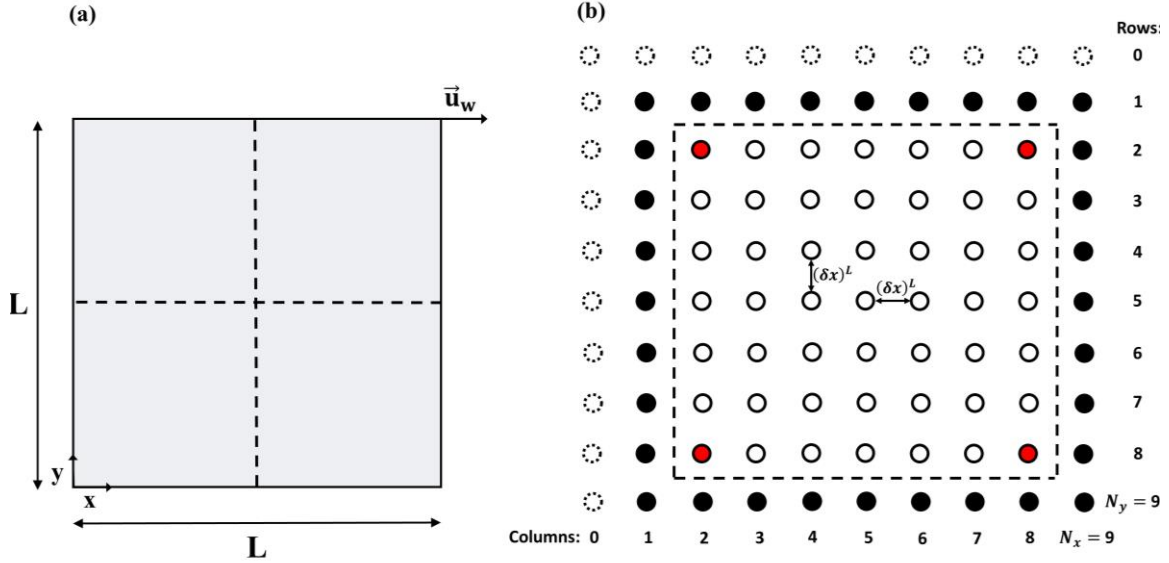


Figure 15: Illustrative sketch of (a) the square-cavity flow benchmark, and (b) LBM domain when  $N_y = 9$ . The blue region represents the fluid. The solid, fluid, corner, and ignored nodes are, respectively, the black, white, red, and dashed nodes. The dashed lines are (a) the central axes of the domain, and (b) the computational boundary for the link-wise approach.

The algorithm for this benchmark is almost the same as for the Couette flow. The difference emerges at the streaming step because the solid boundary conditions must be applied in the lateral walls rather than periodic conditions. However, the halfway bounce-back scheme framework is the same as in Figure 12 and is easily extended for  $\text{column\_new} = 1$  and  $\text{column\_new} = N_x$ .

Moreover, the challenge is to model the boundary conditions in the four corner nodes, i.e., the red nodes in Figure 15(b), and prevent instabilities from arising. At the end of the streaming step, after performing all  $f_i$  propagations and boundary conditions, one must correct two  $f_i$  in each corner node. Hence, the last effort in the streaming step is to incorporate Equation (2.47), as displayed in Figure 16.

The results are compared with the data from Hou *et al.* [66] work, which also accomplished LBM simulations, to validate the algorithm for this benchmark. Both for  $Re = 400$  and  $Re = 5000$ , the density is initialized as  $\rho = 1.0$ . The relaxation time ( $\tau = 0.6$  and  $\tau = 0.8$ ) and the number of nodes ( $N = 101$  and  $N = 257$ ) vary for  $Re = 400$ . The comparison is achieved by analyzing the normalized velocities  $u_x/|\vec{u}_w|$  and  $u_y/|\vec{u}_w|$  over, respectively, the central y-axis and x-axis (see Figure 15(a)).

```
//Corners

//Left-top corner
f[2][2][5] = 0.5*(rho[2][2] - (f[2][2][0] + f[2][2][1] + f[2][2][2] + f[2][2][3] + f[2][2][4] + f[2][2][6] + f[2][2][8]));
f[2][2][7] = f[2][2][5];

//Left-bottom corner
f[Ny-1][2][6] = 0.5*(rho[Ny-1][2] - (f[Ny-1][2][0] + f[Ny-1][2][1] + f[Ny-1][2][2] + f[Ny-1][2][3] + f[Ny-1][2][4]
+ f[Ny-1][2][5] + f[Ny-1][2][7]));
f[Ny-1][2][8] = f[Ny-1][2][6];

//Right-top corner
f[2][Nx-1][6] = 0.5*(rho[2][Nx-1] - (f[2][Nx-1][0] + f[2][Nx-1][1] + f[2][Nx-1][2] + f[2][Nx-1][3]
+ f[2][Nx-1][4] + f[2][Nx-1][5] + f[2][Nx-1][7]));
f[2][Nx-1][8] = f[2][Nx-1][6];

//Right-bottom corner
f[Ny-1][Nx-1][5] = 0.5*(rho[Ny-1][Nx-1] - (f[Ny-1][Nx-1][0] + f[Ny-1][Nx-1][1] + f[Ny-1][Nx-1][2]
+ f[Ny-1][Nx-1][3] + f[Ny-1][Nx-1][4] + f[Ny-1][Nx-1][6] + f[Ny-1][Nx-1][8]));
f[Ny-1][Nx-1][7] = f[Ny-1][Nx-1][5];
```

Figure 16: Corrections of the corner nodes distribution functions in the streaming step, through which Equation (2.47) is incorporated.

Figure 17 shows the reliable agreement of our velocities for  $Re = 400$ . The values remain unaffected by modifying  $\tau$ , but they slightly change at  $0.1 < y/L < 0.5$ ,  $0.1 < x/L < 0.4$ , and  $0.8 < x/L < 1.0$  when adjusting the lattice refinement. In conclusion, the number of fluid nodes is a critical feature to ensure the simulation accuracy for the square-cavity flow. Furthermore, a higher  $N$  may produce colored velocity maps with improved conformity in the post-processing step.

The excellent agreement endures in Figure 18 for a greater Reynolds number ( $Re = 5000$ ). To keep the method stable with the BGK model, the number of nodes increases for  $N = 501$  and the relaxation time drops for  $\tau = 0.55$ . Even with this condition, the Mach number ( $Ma = |\vec{u}_w|/c_s$ ) stays at the limit of accuracy with  $Ma = 0.289 < 0.3$ .

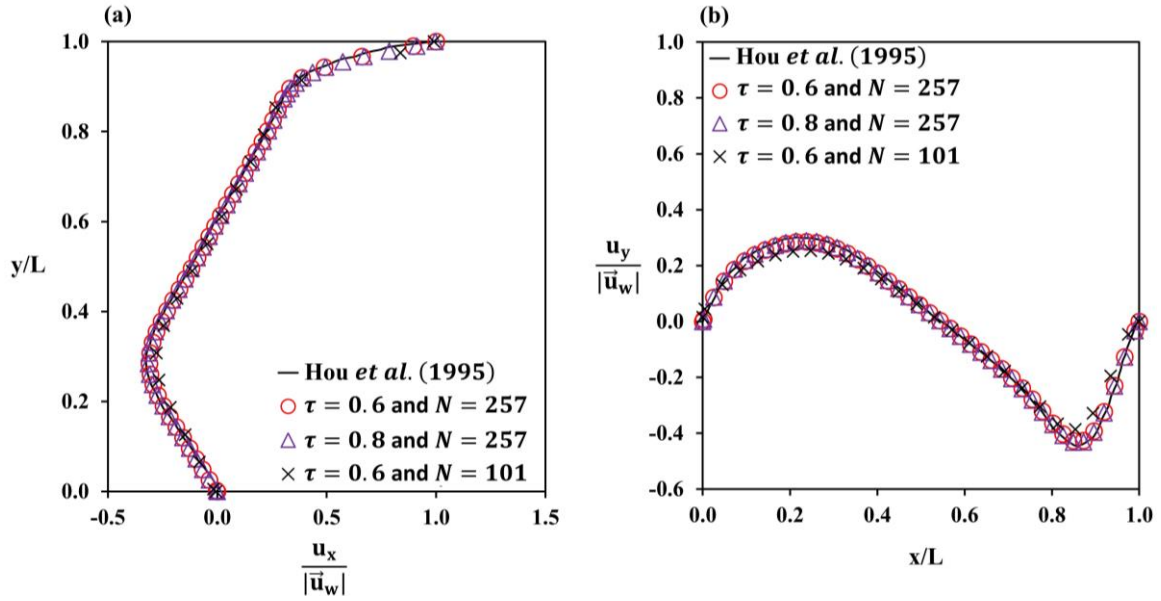


Figure 17: Normalized velocities ( $Re = 400$ ) over the central axes varying the relaxation time ( $\tau = 0.6$  and  $\tau = 0.8$ ) and the number of nodes ( $N = 101$  and  $N = 257$ ), which leads to  $|\vec{u}_w| = 0.052$  l.u. ( $\tau = 0.6$  and  $N = 257$ ),  $|\vec{u}_w| = 0.157$  l.u. ( $\tau = 0.8$ ), and  $|\vec{u}_w| = 0.135$  l.u. ( $\tau = 0.6$  and  $N = 101$ ).

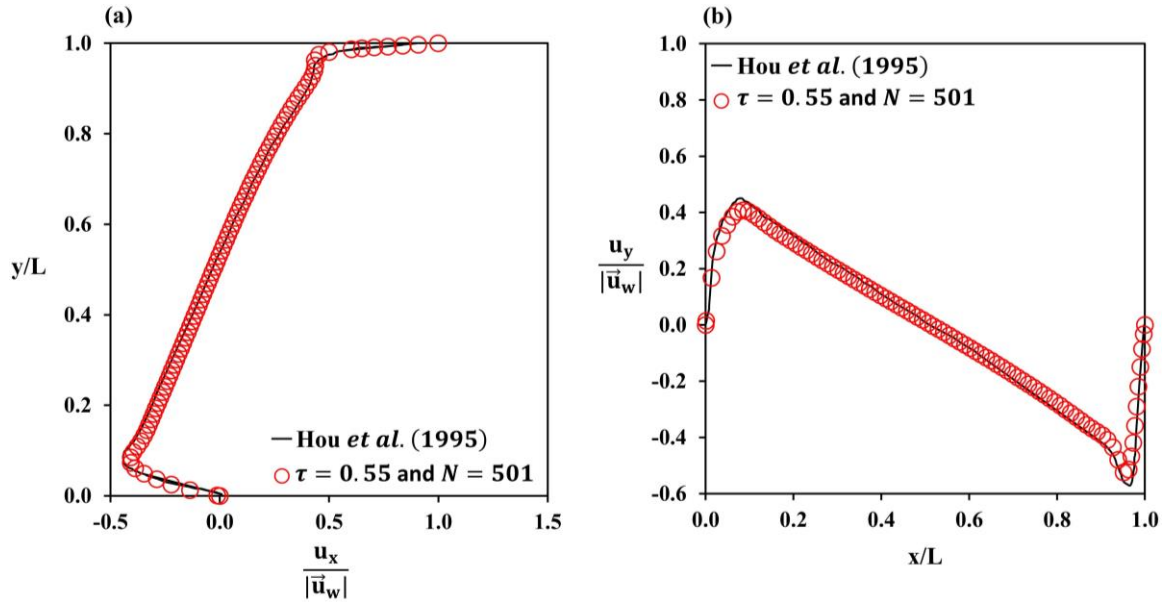


Figure 18: Normalized velocities ( $Re = 5000$ ) over the central axes for  $\tau = 0.55$  and  $N = 501$ , which leads to  $|\vec{u}_w| = 0.167$  l.u.

# Chapter 5

## Unified multiphase model

The previous chapters presented the main LBM features regarding theory, the connection between scales, and implementation aspects. Their discussion also prepares the reader to advance to other LB topics, such as the multiphase analysis. At this point, Chapter 5 delivers the second independent part of this dissertation: the unified multiphase model proposal. Here, we incorporate the bottom-up-based pseudopotential methodology, centered in the Shan-Chen model, into the LBM formalism.

### 5.1 Introduction

Several multiphase models have been addressed in LBM literature. Gunstensen *et al.* [67], based on the Rothman-Keller model [68] for the Lattice Gas Automata, proposed in 1991 the first multiphase approach for LBM, the colored model. It provides a different color for each fluid, causing the interface to arise from the color gradient promptly. Besides the simplicity, the model is ineffective in incorporating thermodynamic concepts.

On the other hand, the free energy model, proposed by Swift *et al.* in 1995 [69, 70], presents a profound thermodynamic foundation. By setting a free energy functional, the non-ideal pressure tensor is calculated and incorporated in LBM. A third approach, initially proposed by He *et al.* in 1999 [71], is based on the phase-field theory. The model incorporates the order parameter and recovers the Cahn-Hilliard or a Cahn-Hilliard-like equation, which discriminates the phase regions.

Many researchers, however, adopt the pseudopotential model proposed by Shan and Chen in 1993 [15] because it is simple to implement and provides good results and computational efficiency [16, 17]. Their insight was to mimic the interactions through an indirect function of space: the pseudopotential. Nevertheless, important limitations have

already been remarked in the literature, such as thermodynamic inconsistency [45, 72], narrow temperature range of application [9, 73], low-density ratios [9, 74, 75], weak stability [51, 76, 77], coupling of physical properties [52, 78, 79], and large spurious currents [80, 81]. Spurious velocities or currents are unphysical velocities that arise in the lattice domain, mainly near curved interfaces, because of a lack of isotropy to calculate the interaction forces [80] and the mesoscopic redistribution [81].

In general, the strategies to mitigate the constraints can be classified into four broad categories: (i) the incorporation of better equations of state (EOS) and optimal parameters [53, 74, 82], (ii) the adoption of forcing schemes [51, 53, 79], (iii) the implementation of different approaches for interaction forces [9, 72, 80, 83], and (iv) the inclusion of enhanced collision operators [31, 84, 85]. Yuan and Schaefer demonstrated that incorporating real EOS can minimize spurious currents and increase density ratios [74]. Additionally, a proper forcing scheme can enhance the thermodynamic consistency, enlarge the temperature range [45], condense spurious currents [86], and independently adjust interface thickness and surface tension from density ratios [79]. However, the third strategy, which involves calculating the interaction force, will be the main focus of this work.

Many seemingly independent interaction models, such as Kupershtokh *et al.* [9], Zhang-Chen [87], Gong-Cheng (also known as  $\beta$ -scheme) [83], and Yang-He [73] are often used in the literature [76, 88, 89]. Fine-tuning of additional parameters certainly enriches the pseudopotential LBM. It can achieve density ratios larger than  $10^4$  with Peng-Robinson EOS [90] or even larger than  $10^9$  with Carnahan-Starling EOS [9], as well as good thermodynamic consistency and a wide temperature range of stability [83]. Besides having been implemented in multicomponent multiphase simulations [8, 88], some models have been successfully carried out in heat problems [91, 92, 93].

Despite their attested individual performances, Kupershtokh *et al.*, Gong-Cheng, and Yang-He forces (Section 5.2) are largely accepted as distinct models [90, 94], and parameters are chosen without a theoretical basis. Here, we suggest a unified model by arguing that there is a relationship among models and their parameters, making them equivalent. We demonstrate this both through algebraic manipulations (Section 5.4) and numerical analysis (Sections 5.5 and 5.6) of multiphase droplet simulations. We confront the models and

compare the extent of their limitations regarding spurious currents, thermodynamic consistency, density ratios, and method stability.

## 5.2 Pseudopotential multiphase models

### 5.2.1 Shan-Chen multiphase model

Shan and Chen proposed the first interaction pseudopotential model [15], which is written in the continuum form as:

$$\vec{F}^{\text{SC}}(\vec{x}) = -Gc_s^2\psi(\vec{x})\vec{\nabla}\psi(\vec{x} + \vec{c}_i\delta t)\delta t^2, \quad (5.1)$$

where  $G$  is an interaction strength, and  $\psi$  is the pseudopotential, also named effective mass. The interaction force can be repulsive, if  $G > 0$ , or attractive, if  $G < 0$ . Equation (5.1) is discretized as:

$$\vec{F}^{\text{SC}}(\vec{x}) = -Gc_s^2\psi(\vec{x}) \sum_i w(|\vec{c}_i|^2)\psi(\vec{x} + \vec{c}_i\delta t)\vec{c}_i\delta t, \quad (5.2)$$

where  $w(|\vec{c}_i|^2)$  are the static weights ( $w(|\mathbf{e}_\alpha|^2) = \omega_\alpha/c_s^2$ ). Because of the external force, the behavior of the fluid is described by a non-ideal EOS:

$$p(\vec{x}) = \rho(\vec{x})c_s^2 + \frac{Gc_s^2\delta t^2\psi^2(\vec{x})}{2}. \quad (5.3)$$

### 5.2.2 Other multiphase models

In 2003, working with non-isothermal problems, Zhang and Chen [87] proposed another interaction model,

$$\vec{F}^{\text{ZC}}(\vec{x}) = -\vec{\nabla}U(\vec{x} + \vec{c}_i\delta t), \quad (5.4)$$

where the EOS can be inserted by:

$$U(\vec{x}) = p(\vec{x}) - \rho(\vec{x})c_s^2. \quad (5.5)$$

However, the Zhang-Chen model proved insufficiently accurate and stable to model the multiphase problems in their central discussion [95]. Around 2007, Kupershtokh *et al.* [96] extended this model, which can be rewritten as follows,

$$\vec{F}^{\text{ZC}}(\vec{x}) = -\vec{\nabla}U = \vec{\nabla}(-U) = \vec{\nabla}(\sqrt{-U})^2 = 2\sqrt{-U}\vec{\nabla}(\sqrt{-U}). \quad (5.6)$$

Through adding and subtracting  $\vec{\nabla}(-U)$  multiplied by a constant  $A$  in Equation (5.4),

$$\vec{F}^{\text{K}}(\vec{x}) = \vec{\nabla}(-U) + A\vec{\nabla}(-U) - A\vec{\nabla}(-U). \quad (5.7)$$

Replacing the first and the last terms on the RHS of Equation (5.7) with Equation (5.6),

$$\vec{F}^{\text{K}}(\vec{x}) = 2\sqrt{-U}\vec{\nabla}(\sqrt{-U}) + A\vec{\nabla}(-U) - 2A\sqrt{-U}\vec{\nabla}(\sqrt{-U}). \quad (5.8)$$

Finally, using the definition  $\phi^2 = -U$ , Kupershtokh *et al.* model is given by:

$$\vec{F}^{\text{K}}(\vec{x}) = A\vec{\nabla}\phi^2(\vec{x} + \vec{c}_i\delta t) + 2(1 - A)\phi(\vec{x})\vec{\nabla}\phi(\vec{x} + \vec{c}_i\delta t), \quad (5.9)$$

which can be discretized as follows,

$$\begin{aligned}\vec{F}^K(\vec{x}) &= A \sum_i w(|\vec{c}_i|^2) \phi^2(\vec{x} + \vec{c}_i \delta t) \vec{c}_i \delta t + \\ &+ 2(1 - A) \phi(\vec{x}) \sum_i w(|\vec{c}_i|^2) \phi(\vec{x} + \vec{c}_i \delta t) \vec{c}_i \delta t.\end{aligned}\tag{5.10}$$

However, Kupershtokh *et al.* model is originally written differently. If we add and subtract  $2A\vec{V}(-U)$  in Equation (5.4) instead of  $A\vec{V}(-U)$  and repeat the previous steps, we get:

$$\vec{F}^K(\vec{x}) = 2A\vec{V}\phi^2(\vec{x} + \vec{c}_i \delta t) + 2(1 - 2A)\phi(\vec{x})\vec{V}\phi(\vec{x} + \vec{c}_i \delta t),\tag{5.11}$$

which can be discretized similarly,

$$\begin{aligned}\vec{F}^K(\vec{x}) &= 2A \sum_i w(|\vec{c}_i|^2) \phi^2(\vec{x} + \vec{c}_i \delta t) \vec{c}_i \delta t + \\ &+ 2(1 - 2A) \phi(\vec{x}) \sum_i w(|\vec{c}_i|^2) \phi(\vec{x} + \vec{c}_i \delta t) \vec{c}_i \delta t.\end{aligned}\tag{5.12}$$

Between these two options, we apply Equation (5.10) in our study since it is a commonly used [16, 76, 94] form of the Kupershtokh *et al.* model.

In 2012, Gong and Cheng [83] investigated a proposition similar to the one above but in the Shan-Chen model. The authors rewrote Equation (5.1) as:

$$\vec{F}^{SC}(\vec{x}) = -Gc_s^2 \psi(\vec{x}) \vec{V} \psi(\vec{x} + \vec{c}_i \delta t) \delta t^2 = -\frac{Gc_s^2}{2} \vec{V} \psi^2(\vec{x} + \vec{c}_i \delta t) \delta t^2.\tag{5.13}$$

Through adding and subtracting  $Gc_s^2 \psi \vec{V} \psi \delta t^2$  multiplied by a constant  $\beta$  in Equation (5.13),

$$\vec{F}^\beta(\vec{x}) = -\frac{Gc_s^2}{2} \vec{V} \psi^2(\vec{x} + \vec{c}_i \delta t) \delta t^2 - \beta Gc_s^2 \psi(\vec{x}) \vec{V} \psi(\vec{x} + \vec{c}_i \delta t) \delta t^2 +\tag{5.14}$$

$$+\beta G c_s^2 \psi(\vec{x}) \vec{\nabla} \psi(\vec{x} + \vec{c}_i \delta t) \delta t^2 .$$

Recalling that  $\psi \vec{\nabla} \psi = \vec{\nabla} \psi^2 / 2$ , the last term on the RHS of Equation (5.14) can be rewritten. Consequently, the Gong-Cheng model, also called  $\beta$ -scheme, is given by:

$$\vec{F}^\beta(\vec{x}) = -\beta G c_s^2 \psi(\vec{x}) \vec{\nabla} \psi(\vec{x} + \vec{c}_i \delta t) \delta t^2 - \frac{(1 - \beta) G c_s^2}{2} \vec{\nabla} \psi^2(\vec{x} + \vec{c}_i \delta t) \delta t^2, \quad (5.15)$$

which can be discretized as follows,

$$\begin{aligned} \vec{F}^\beta(\vec{x}) = & -\beta G c_s^2 \psi(\vec{x}) \sum_i w(|\vec{c}_i|^2) \psi(\vec{x} + \vec{c}_i \delta t) \vec{c}_i \delta t + \\ & - \frac{(1 - \beta) G c_s^2}{2} \sum_i w(|\vec{c}_i|^2) \psi^2(\vec{x} + \vec{c}_i \delta t) \vec{c}_i \delta t . \end{aligned} \quad (5.16)$$

Yang-He interaction model was similarly derived [73],

$$\begin{aligned} \vec{F}^{\text{YH}}(\vec{x}) = & -\varepsilon G c_s^2 \psi(\vec{x}) \sum_i w(|\vec{c}_i|^2) \psi(\vec{x} + \vec{c}_i \delta t) \vec{c}_i \delta t + \\ & -(1 - \varepsilon) \sum_i w(|\vec{c}_i|^2) U(\vec{x} + \vec{c}_i \delta t) \vec{c}_i \delta t , \end{aligned} \quad (5.17)$$

where  $\varepsilon$  is the Yang-He parameter. The model presented spurious velocities, density ratio range, and thermodynamic consistency only slightly better than the  $\beta$ -scheme [73].

### 5.3 Equations of State and thermodynamic consistency

Yuan and Schaefer [74] presented how to incorporate several EOS in LBM through the pseudopotential methodology. In this way, general cubic EOS, such as Peng-Robinson [74], van der Waals [51], Carnahan-Starling [8, 82, 97], and even EOS like CPA (Cubic-

Plus-Association) [86, 98] can be introduced in the method. The non-ideal EOS given by Equation (5.3) is rewritten as:

$$\psi(\vec{x}) = \sqrt{\frac{2[p(\vec{x}) - \rho(\vec{x})c_s^2]}{Gc_s^2\delta t^2}} . \quad (5.18)$$

When the effective mass given by Equation (5.18) is substituted into the interaction model, the parameter  $G$  cancels out. Only its sign, however, remains relevant to ensure that the term inside the square root is positive [74].

Phase densities for a single-component system can be calculated from the Maxwell equal-area construction rule and compared to densities obtained from LBM. Therefore, this approach is often adopted to check the thermodynamic consistency of LBM multiphase calculations [16, 17]. The Yuan-Schaefer's methodology naturally causes inconsistency [45] because the pseudopotential model requires an appropriate  $\psi$  to achieve consistency, i.e.,  $\psi \propto \exp(-1/\rho)$  [72]. Zhang and Tian, to avoid what they have characterized as an unphysical methodology, have proposed to introduce the EOS through a modification in the equilibrium distribution function [99]. Since their approach violates the Galilean invariance [45], Yuan and Schaefer's methodology stands as a practical step to introduce well-known EOS in LBM. The consistency can be later enforced by adding some degrees of freedom in the discrete forces [9, 83] or employing Li *et al.* forcing scheme [45].

The Maxwell construction imposes the following condition for a chosen EOS at a given reduced temperature  $T_r = T/T_c$ , where  $T_c$  is the critical temperature:

$$\int_{\rho_v}^{\rho_l} [p_0 - p_{EOS}(\rho)] dv = 0 , \quad (5.19)$$

where  $\rho_v$  is the vapor density,  $\rho_l$  is the liquid density,  $p_0$  is the saturation pressure,  $v$  is the molar volume and  $p_{EOS}$  incorporates the expression of the chosen EOS. After some iterations, we reach the equilibrium,  $p_0 = p_{EOS}(\rho_v, T_r) = p_{EOS}(\rho_l, T_r)$ , and, consequently, get the phase

density values. The reduced volume is similarly defined as  $v_r = \rho_c/\rho$ , where  $\rho_c$  is the critical density.

## 5.4 A unified multiphase model

Here, we propose a unified model that gathers the pseudopotential models displayed in Section 5.2. We briefly demonstrate the association among the models in Section 5.4.1, and we further compare the pressure tensors in Section 5.4.2.

### 5.4.1 Model proposal

It will be demonstrated that the  $\beta$ -scheme can be turned into the Kupershtokh *et al.* interaction model. This is possible because  $\psi$  can be written as a function of  $U$  and vice versa,

$$\psi(\vec{x}) = \sqrt{\frac{2(p - \rho c_s^2)}{G c_s^2 \delta t^2}} = \sqrt{\frac{2}{G c_s^2 \delta t^2}} \sqrt{U(\vec{x})}. \quad (5.20)$$

Equation (5.20) can be substituted into Equation (5.15), and the  $\beta$ -scheme is now given by:

$$\vec{F}^\beta(\vec{x}) = -2\beta\sqrt{U(\vec{x})}\vec{\nabla}\sqrt{U(\vec{x} + \vec{c}_1\delta t)} - (1 - \beta)\vec{\nabla}U(\vec{x} + \vec{c}_1\delta t). \quad (5.21)$$

Recalling that  $\phi^2 = -U$ ,

$$\vec{F}^\beta(\vec{x}) = -2\beta\phi(\vec{x})i\vec{\nabla}\phi(\vec{x} + \vec{c}_1\delta t)i + (1 - \beta)\vec{\nabla}\phi^2(\vec{x} + \vec{c}_1\delta t), \quad (5.22)$$

where  $i$  is the unit imaginary number ( $i^2 = -1$ ), which gives:

$$\vec{F}^\beta(\vec{x}) = 2\beta\phi(\vec{x})\vec{\nabla}\phi(\vec{x} + \vec{c}_i\delta t) + (1 - \beta)\vec{\nabla}\phi^2(\vec{x} + \vec{c}_i\delta t). \quad (5.23)$$

Now, we must make the definition  $A + \beta = 1$ , which makes it possible to write Equation (5.23) as follows,

$$\vec{F}^\beta(\vec{x}) = 2(1 - A)\phi(\vec{x})\vec{\nabla}\phi(\vec{x} + \vec{c}_i\delta t) + A\vec{\nabla}\phi^2(\vec{x} + \vec{c}_i\delta t) = \vec{F}^K(\vec{x}). \quad (5.24)$$

Therefore, when it is assumed that  $A + \beta = 1$ ,  $\beta$ -scheme can be successfully turned into Equation (5.24), the Kupershtokh *et al.* interaction model. We must note that the parameters were initially adjusted in Section 5.5.1 without imposing this constraint in our simulations, but their optimal values naturally converged to satisfy it. Hence, Kupershtokh *et al.* model can be converted to  $\beta$ -scheme and vice versa.  $\beta$ -scheme can also be recovered from the Yang-He model when we incorporate  $\psi = \psi(U)$  and  $\varepsilon = \beta$ . Consequently, the small discrepancies the authors [73] observed between the models may be due either to differences in parameter values or to numerical errors.

Given all the previous models, a last unified model can be written in continuous form as:

$$\vec{F}(\vec{x}) = -Y G c_s^2 \psi(\vec{x}) \vec{\nabla} \psi(\vec{x} + \vec{c}_i \delta t) \delta t^2 + \quad (5.25)$$

$$- \frac{(1 - Y) G c_s^2}{2} \vec{\nabla} \psi^2(\vec{x} + \vec{c}_i \delta t) \delta t^2,$$

where  $Y$  is the unified parameter whose appropriate value recovers the desired model:

$$Y = \begin{cases} 1, \text{Shan-Chen model} \\ 0, \text{Zhang-Chen model} \\ 1 - A, \text{Kupershtokh } et al. \text{ model} \\ \beta, \text{Gong-Cheng model} \\ \varepsilon, \text{Yang-He model} \end{cases} \quad (5.26)$$

Hence, the unified model groups the recurrent multiphase interaction forces in a uniform format and emphasizes that these models, especially for the commonly identified different models (i.e., Kupershtokh *et al.*, Gong-Cheng, and Yang-He models), are, actually, the same. This general equation might simplify future discussions and direct the reader to tune only one parameter in only one multiphase interaction model.

The final unified discrete form, further detailed in Section 5.4.2, is:

$$\begin{aligned} \vec{F}(\vec{x}) = & -Y G c_s^2 \psi(\vec{x}) \sum_i w(|\vec{c}_i|^2) \psi(\vec{x} + \vec{c}_i) \vec{c}_i + \\ & - \frac{(1-Y) G c_s^2}{2} \sum_i w(|\vec{c}_i|^2) \psi^2(\vec{x} + \vec{c}_i) \vec{c}_i, \end{aligned} \quad (5.27)$$

where the simplification  $\delta t = 1$  is already considered. Note also that, Equation (5.9) is the Kupershtokh *et al.* model recovered by  $Y = 1 - A$ , causing the relationship  $A + \beta = 1$  to originate. If Equation (5.11) is recognized as the Kupershtokh *et al.* model instead, the relationship must be rewritten as  $Y = 1 - 2A$ , which provides  $2A + \beta = 1$ .

## 5.4.2 Checking the pressure tensors

In this section, we compare the pressure tensors in discrete form. Shan, in his paper, gave some attention to how to correctly calculate the pressure tensor and assure the exact mechanical balance [100]. Instead of calculating it through Taylor expansion, the discrete force is used in the definition of the pressure tensor  $\mathbf{P}$ ,

$$\vec{dF} = \vec{dA} \cdot \mathbf{P}, \quad (5.28)$$

where  $\vec{dA}$  is an infinitesimal area element and  $\vec{dF}$  is the interaction force through  $\vec{dA}$ .

The force is integrated over a closed volume afterward. As a result, the pressure tensor corresponding to the Shan-Chen model and 4th degree of isotropy is:

$$\mathbf{P}^{\text{SC}} = -\frac{Gc_s^2}{2}\psi(\vec{x}) \sum_i w(|\vec{c}_i|^2)\psi(\vec{x} + \vec{c}_i\delta t)\vec{c}_i\delta t\vec{c}_i\delta t. \quad (5.29)$$

Similarly, the pressure tensors corresponding to the  $\beta$ -scheme and the Kupershtokh *et al.* model with 4th degree of isotropy are, respectively,

$$\begin{aligned} \mathbf{P}^\beta &= -\frac{\beta Gc_s^2}{2}\psi(\vec{x}) \sum_i w^\beta(|\vec{c}_i|^2)\psi(\vec{x} + \vec{c}_i\delta t)\vec{c}_i\delta t\vec{c}_i\delta t + \\ &\quad -\frac{(1-\beta)Gc_s^2}{4}\sum_i w^\beta(|\vec{c}_i|^2)\psi^2(\vec{x} + \vec{c}_i\delta t)\vec{c}_i\delta t\vec{c}_i\delta t, \end{aligned} \quad (5.30)$$

$$\begin{aligned} \mathbf{P}^{\text{K}} &= (1-A)\phi(\vec{x}) \sum_i w^{\text{K}}(|\vec{c}_i|^2)\phi(\vec{x} + \vec{c}_i\delta t)\vec{c}_i\delta t\vec{c}_i\delta t + \\ &\quad +\frac{A}{2}\sum_i w^{\text{K}}(|\vec{c}_i|^2)\phi^2(\vec{x} + \vec{c}_i\delta t)\vec{c}_i\delta t\vec{c}_i\delta t, \end{aligned} \quad (5.31)$$

where “ $\beta$ ” and “K” in  $w(|\vec{c}_i|^2)$  identify the dimensions of the weights used in the  $\beta$ -scheme and Kupershtokh *et al.* model, respectively. This distinction will be understood soon.

Making the substitution of Equation (5.20) into the Equation (5.30),

$$\mathbf{P}^\beta = -\frac{1}{(\delta t)^2} \left[ \begin{aligned} &\beta\sqrt{U(\vec{x})} \sum_i w^\beta(|\vec{c}_i|^2)\sqrt{U(\vec{x} + \vec{c}_i\delta t)}\vec{c}_i\delta t\vec{c}_i\delta t + \\ &+\frac{(1-\beta)}{2}\sum_i w^\beta(|\vec{c}_i|^2)U(\vec{x} + \vec{c}_i\delta t)\vec{c}_i\delta t\vec{c}_i\delta t \end{aligned} \right], \quad (5.32)$$

and reminding that  $\phi^2 = -U$ ,

$$\mathbf{P}^\beta = \frac{1}{(\delta t)^2} \left[ \begin{aligned} &\beta\phi(\vec{x}) \sum_i w^\beta(|\vec{c}_i|^2)\phi(\vec{x} + \vec{c}_i\delta t)\vec{c}_i\delta t\vec{c}_i\delta t + \\ &+\frac{(1-\beta)}{2}\sum_i w^\beta(|\vec{c}_i|^2)\phi^2(\vec{x} + \vec{c}_i\delta t)\vec{c}_i\delta t\vec{c}_i\delta t \end{aligned} \right]. \quad (5.33)$$

Again, we must use the previous definition that  $A + \beta = 1$ , which turns Equation (5.33) into:

$$\mathbf{P}^\beta = \frac{1}{(\delta t)^2} \left[ \begin{aligned} &(1 - A)\phi(\vec{x}) \sum_i w^\beta(|\vec{c}_i|^2) \phi(\vec{x} + \vec{c}_i \delta t) \vec{c}_i \delta t \vec{c}_i \delta t + \\ &+ \frac{A}{2} \sum_i w^\beta(|\vec{c}_i|^2) \phi^2(\vec{x} + \vec{c}_i \delta t) \vec{c}_i \delta t \vec{c}_i \delta t \end{aligned} \right]. \quad (5.34)$$

Since the weighting values are the same, i.e.,  $|w^\beta(|\vec{c}_i|^2)| = |w^K(|\vec{c}_i|^2)|$ , Equation (5.31) can be substituted into Equation (5.34),

$$\mathbf{P}^\beta = \frac{\mathbf{P}^K}{(\delta t)^2}. \quad (5.35)$$

Equation (5.35) shows the models are the same only when  $\delta t = 1$ . This happens because the discretized gradients of the models in the continuum form are different. To clarify the relationship, note that the dimension (here, we use the notation [variable/parameter] to declare the dimension of the variable/parameter) of the weight in the  $\beta$ -scheme is  $[w^\beta(|\vec{c}_i|^2)] = \text{time}^2/\text{length}^2$ , which can be deduced by recognizing that  $\beta$  is a dimensionless parameter and  $[\psi] = [\rho] = \text{mass}/\text{length}^3$ , inspecting  $[\bar{\mathbf{F}}]$  and  $[G]$  in Equations (2.66) and (5.18), respectively, and finally discovering  $[w(|\vec{c}_i|^2)]$  in Equation (5.16). On the other hand, the dimension of the Kupershtokh *et al.* weight is  $[w^K(|\vec{c}_i|^2)] = 1/\text{length}^2$ , which can be deduced regarding that  $A$  is a dimensionless parameter, investigating  $[\phi]$  in Equation (5.5) and then verifying  $[w(|\vec{c}_i|^2)]$  in Equation (5.10). Because of  $[w^\beta(|\vec{c}_i|^2)] \neq [w^K(|\vec{c}_i|^2)]$ , both Equations (5.31) and (5.34), and consequently, Equation (5.35) preserve the dimensional homogeneity. Therefore, when  $A + \beta = 1$  and  $\delta t = 1$ , we check that  $\mathbf{P}^\beta = \mathbf{P}^K$ .

## 5.5 Static droplet

In this section, we numerically demonstrate the results from the unified model that ensure the connection between the models. The first benchmark is the stationary droplet problem.

### 5.5.1 Methodology

We perform isothermal single-component phase transition simulations in a  $200 \times 200$  periodic lattice. The droplet is initialized at the center of a convection-free domain  $(x_c, y_c)$  with radius  $R_0 = 30$  l.u. and interface thickness  $W = 3$  l.u., as defined by the following equation:

$$\rho(x, y) = \frac{\rho_l + \rho_v}{2} - \frac{\rho_l - \rho_v}{2} \left[ \tanh \left( 2 \frac{\sqrt{(x - x_c)^2 + (y - y_c)^2} - R_0}{W} \right) \right]. \quad (5.36)$$

A hydrostatic domain is chosen for the droplet to capture the formation of any spurious current in the system [78]. In this work, the Carnahan-Starling EOS with the van der Waals attractive term (CSvdW EOS),

$$p(\vec{x}) = \rho(\vec{x})RT \left\{ \frac{1 + \eta(\vec{x}) + \eta^2(\vec{x}) - \eta^3(\vec{x})}{[1 - \eta(\vec{x})]^3} \right\} - a\rho^2(\vec{x}), \quad (5.37)$$

is inserted in Equation (5.18), where  $R$  is the universal gas constant,  $T$  is the temperature,  $\eta = b\rho/4$ ,  $a = 0.4963R^2T_c^2/p_c$ ,  $b = 0.18727RT_c/p_c$  and  $T_c$  and  $p_c$  are the critical temperature and pressure, respectively. The CSvdW EOS is adopted to describe the phase transition by setting  $a = 1$ ,  $R = 1$  and  $T_c = 0.094$  as in reference [45].

The initial densities of the vapor ( $\rho_v$ ) and liquid ( $\rho_l$ ) phases are obtained from the Maxwell construction (see Section 5.3) for each  $T_r$ . We implement BGK and D2Q9 models with  $\delta x = 1$  and  $\delta t = 1$ , along with the fourth-order isotropy degree and the EDM forcing

scheme to calculate interaction forces and insert them in the LBM approach. The relaxation time is fixed as  $\tau = 0.95$ , around which the EDM stability begins to saturate [51].

We write our codes in C/C++ to ensure fast LBM simulations and calculate the absolute values of the density differences after each  $10^4$  iterations for every fluid node. The convergence criteria is  $|\rho_{\bar{x},t} - \rho_{\bar{x},t-10^4}| \leq 10^{-7}$ , which is reached up to iteration  $\approx 10^5$ , depending on  $T_r$ . The illustrative images are produced using the open-access software GNU Octave 5.1.0 [101]. The density results were compared to the Maxwell construction points in the range of  $T_r = [0.40, 0.95]$  with 0.05 increments. Following the procedure in [8, 9, 76, 83], the optimal fit for simulation points and the Maxwell coexistence curve is found for  $A = -0.152$  and  $\beta = 1.152$ . The value of  $A$  agrees well with the Kupershtokh *et al.* work [9], but we expected a higher  $\beta$  like in the reference [102]. Nevertheless, our values are in agreement with Equation (5.26) and reinforce the connection between the parameters.

## 5.5.2 Results and discussion

### 5.5.2.1 Numerical validation

The coexistence curve for each model is shown in Figure 19. Zhang-Chen model delivers the most unstable simulations, as addressed in the literature [73, 83]. Before the instability emerges at  $T_r = 0.85$ , the relative error regarding the Maxwell construction densities already reaches 19.2% in the vapor phase, which is 15 times higher than the average error of the other models at the same conditions. Because of this narrow range of stability, we will omit the Zhang-Chen model in the next discussions. Additionally, from our unified model, we see that the  $\beta$ -scheme and Yang-He parameters are equivalent, i.e.,  $\beta = \varepsilon$ . Consequently, what is going to be said about the  $\beta$ -scheme will also be valid to the Yang-He model.

Relative errors regarding the Maxwell construction densities for both vapor and liquid phases are displayed in Figure 20. Although the Shan-Chen model is stable at low temperatures, it performs worse than the others. The relative errors for the Shan-Chen model are small in the liquid phase but nearly reach 100% in the interval  $T_r = [0.40, 0.50]$ . In fact, for all the models, the vapor phase matching is worse than the liquid phase.

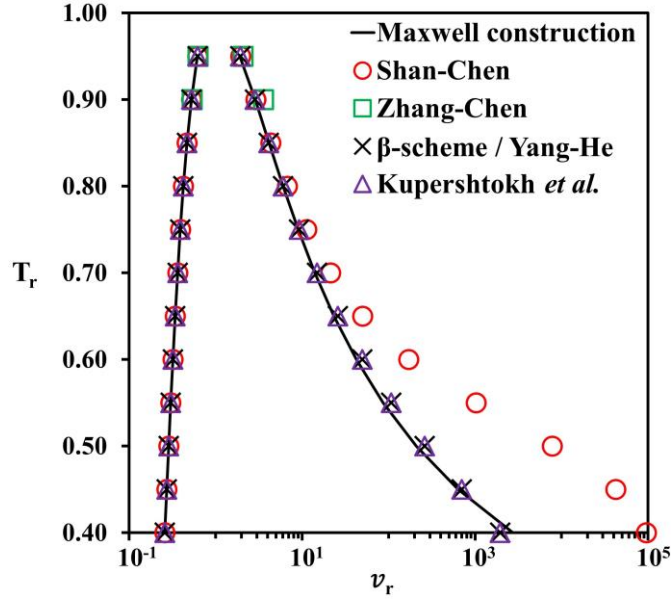


Figure 19: Comparison of the Maxwell coexistence curve with the LB interaction models coexistence curves.

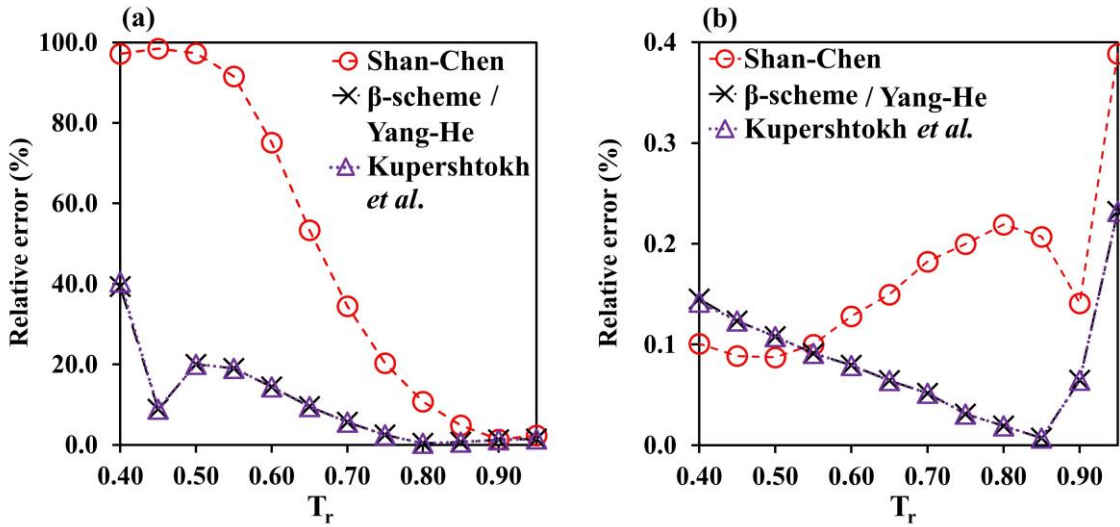


Figure 20: Relative errors of the LBM densities in the (a) vapor and (b) liquid phases. The Maxwell construction densities were considered as a benchmark to calculate the errors. Lines are plotted to help guide the eye.

Since the vapor-phase density varies more with the parameter, we tuned  $A$  and  $\beta$  using only the vapor densities from the Maxwell construction. For each  $T_r$ , we investigated the parameter range that best matches the points, and we found that it is more limited at low temperatures. Just exemplifying, when we reduce  $\beta$  by 0.03 from its optimal value, the error reaches 57% at  $T_r = 0.40$  but only 5% at  $T_r = 0.80$ . Therefore, optimal parameter values

should be chosen to minimize the deviations from the Maxwell vapor densities at low temperatures. Since the optimal range is wide at large temperatures, we easily confirmed that the adjusted values are suitable for the entire range.

Because of the extra parameters, the coexistence curve fits well for the Kupershtokh *et al.* model and  $\beta$ -scheme. Figure 20(a) shows that the relative error in the vapor phase decreases with temperature and is less than 10% in the interval  $T_r = [0.65, 0.95]$ . There is, however, an outlier at  $T_r = 0.45$ , which has a smaller relative error than the neighboring points because the parameters tuned are closer to the required optimal values at  $T_r = 0.45$ . In Figure 20(b), despite the Shan-Chen model yielding the greatest errors for the liquid phase at temperatures above  $T_r = 0.55$ , the differences among the models are negligible, considering that the relative errors are less than 0.4% for the entire temperature range. Although the parameters were set independently, the final coexistence curve is the same for Kupershtokh *et al.* model and  $\beta$ -scheme.

Further investigation showed that other physical quantities also vary similarly between the models. Figure 21 brings the spurious velocities changes with the temperature. The maximum spurious velocities from Kupershtokh *et al.* model and  $\beta$ -scheme are also similar. A cubic polynomial fit well describes the dependence on reduced temperature. All three models show comparable spurious velocities when  $T_r$  is above 0.70. Below it, the

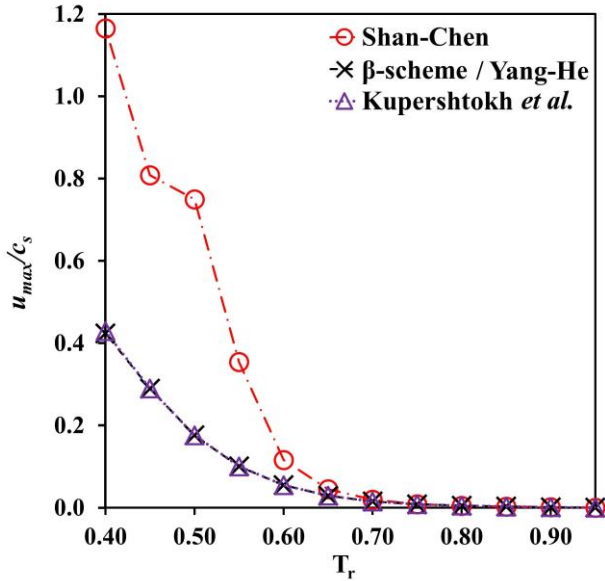


Figure 21: Maximum spurious velocities versus reduced temperature for the interaction models considered. Lines are plotted to help guide the eye.

velocity from the Shan-Chen model increases faster and more disorderly. The top is reached at  $T_r = 0.40$ , when  $u_{max}/c_s$  for the Shan-Chen model is approximately three times higher than for the other models. In Figure 22, this difference in magnitude depends on the lattice node location and that the maximum values emerge in no more than few areas near the interface. Note also that the spurious velocities from Kupershtokh *et al.* model and  $\beta$ -scheme are similar in every node of the domain.

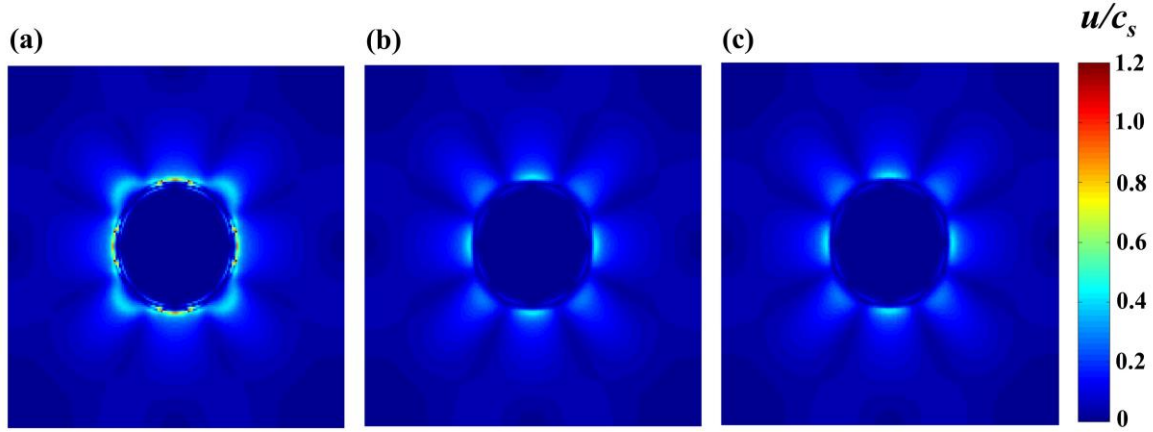


Figure 22: Location of the spurious velocities in the domain for (a) Shan-Chen model, (b)  $\beta$ -scheme and Yang-He models, and (c) Kupershtokh *et al.* model.

Besides the spurious velocities, the method stability is also associated with the interface thickness [77] and density ratio [74]. The EDM forcing scheme, the CSvdW EOS, and the chosen relaxation time help keeping the method stable in a wide temperature range of the simulations. In Figure 23, the interface thickness contraction, which immediately happens at high temperatures, follows the temperature decrease. Here, we consider the interface thickness as the lattice length between the different phases where the densities still varying from the average bulk values. With the conditions used in this work, the stability and the interface thickness behavior stay unaffected when varying the interaction models. The density ratios achieved at  $T_r = 0.40$ , however, are different: 367885:1 (Shan-Chen model); 7488:1 (Kupershtokh *et al.* model); and 7549:1 ( $\beta$ -scheme).

The Shan-Chen model attains the greatest ratio, but the value strongly deviates from the Maxwell construction (10534:1), as expected from Figure 19. Again, the Kupershtokh *et al.* model and  $\beta$ -scheme come closest to the analytical solution. Although the density ratios

from these last models seem to be different, the similar relative errors regarding the Maxwell construction ratio (28.91% for Kupershtokh *et al.* model and 28.34% for  $\beta$ -scheme) show the opposite. The explanation is that the differences are intensified when the ratio is analyzed, even when there are small density variations.

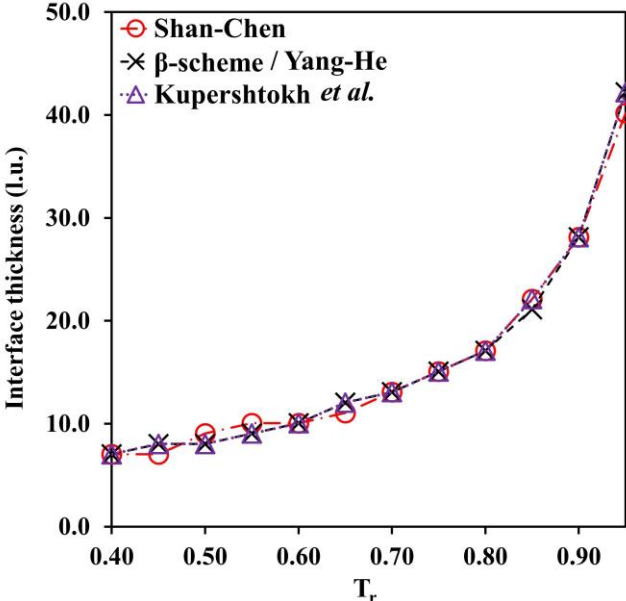


Figure 23: Interface thickness changes with reduced temperature for the interaction models considered. Lines are plotted to help guide the eye.

### 5.5.2.2 Parameter improvement

The stationary droplet benchmark successfully validates the interphase models in Section 5.5.2.1. As observed, the optimal parameters are dependent on  $T_r$ , therefore, we now propose  $A = A(T_r)$  and  $\beta = \beta(T_r)$  instead of tuning only one value for all  $T_r$ . These functions were found matching a second-degree polynomial curve to the optimal parameter points, as presented in Figure 24. The succeeding results confirm that the six points used were adequate to predict the functions and reduce the thermodynamic inconsistency. As the ranges of optimal parameters are thinner at low  $T_r$ , the three smallest temperatures (i.e.,  $T_r = [0.40, 0.50]$ ) were considered to improve the fitting in this region.

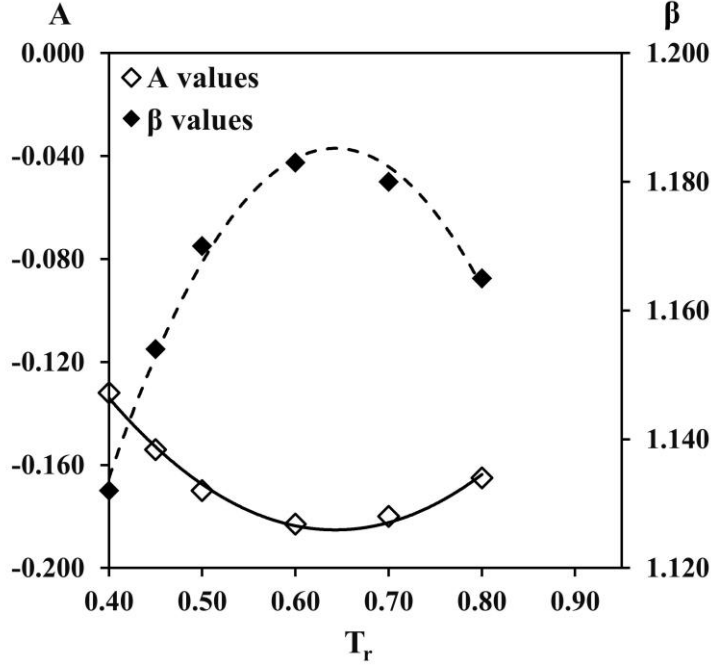


Figure 24: Polynomial fitting of the parameter values. Solid line (—):  $A(T_r) = 0.870 T_r^2 - 1.118 T_r + 0.174$ . Dashed line (---):  $\beta(T_r) = -0.870 T_r^2 + 1.118 T_r + 0.826$ .

Since the Kupershtokh *et al.* and  $\beta$ -scheme models are interchangeable, we can develop the parameter related to the stated functions as  $A(T_r) + \beta(T_r) = 1$  and then choose only one model to check the improvement. In this section, only the Kupershtokh *et al.* model (26.95 iterations/s) is used because its computational performance was almost 2.5 times faster than the  $\beta$ -scheme (11.33 iterations/s). This variation in computational time is due to differences in implementation.

In Figure 25, we compare the relative errors of the Kupershtokh *et al.* model with the fixed parameter  $A = -0.152$  (say “fixed model”) and with  $A = A(T_r)$  (say “function model”). In the vapor phase, Figure 25(a), the largest error of the function model is 7.50% at  $T_r = 0.45$ , which is more than 5 times lower than for the fixed model. The relative errors are less than 1.0% for  $T_r = [0.55, 0.90]$ . Below this range, the error increases because of the large sensitivity of the densities related to the parameter value. The thermodynamic consistency in the liquid phase, i.e., Figure 25(b), remains markedly good after the improvement.

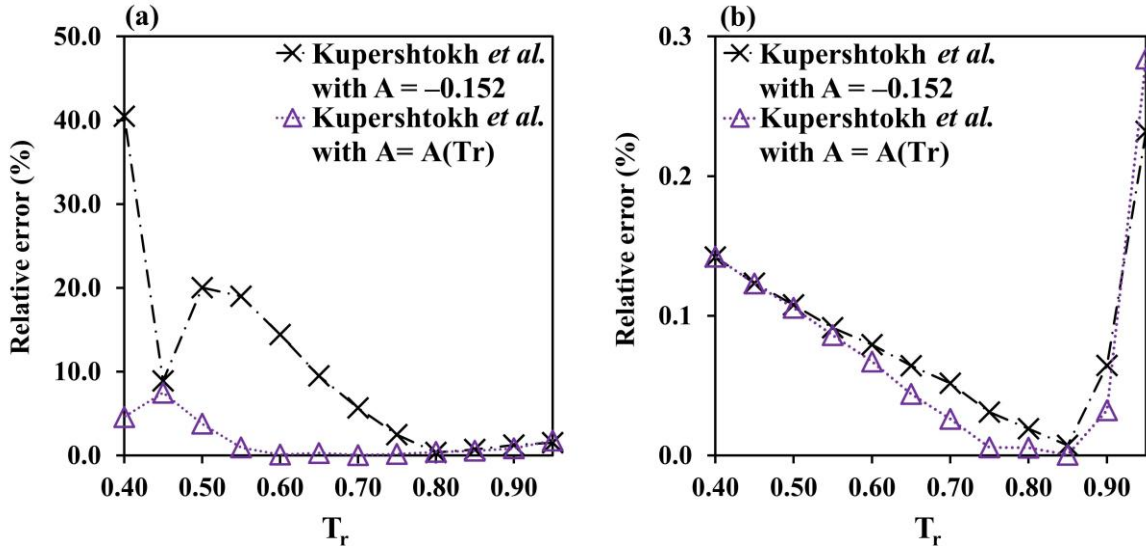


Figure 25: Comparison between the density relative errors using Kopershtokh *et al.* model in the (a) vapor and (b) liquid phases. The Maxwell construction densities were considered as a benchmark to calculate the errors. Lines are plotted to help guide the eye.

In Figure 26, spurious velocities and interface thickness are plotted to check if the parameter improvement affects these quantities. The performance of the spurious current changes slightly, reaching the top at  $T_r = 0.40$ , when  $u_{max}/c_s = 0.500$  (16.55% larger than for the fixed model). Conversely, there are no critical changes in the description of the interface thickness. The method preserved the stability in the same evaluated range by employing parameter improvement.

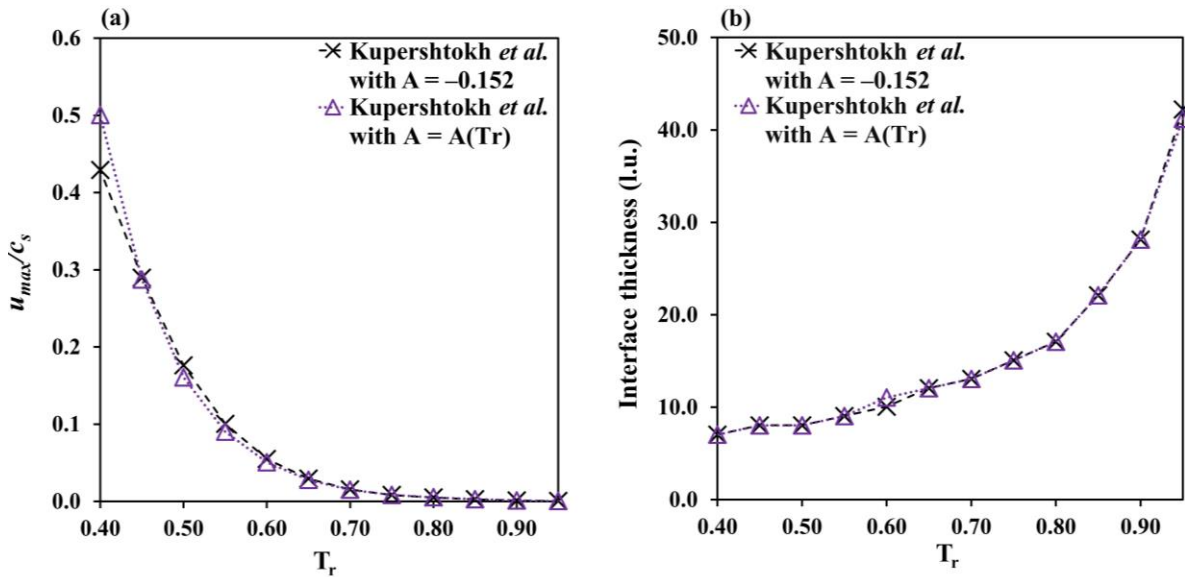


Figure 26: Changes in (a) maximum spurious velocities and (b) interface thickness with the reduced temperature for the Kopershtokh *et al.* model. The lines are plotted to help guide the eye.

## 5.6 Droplet oscillation

Now, we validate the dynamic behavior of the unified model. In this benchmark, an elliptic droplet is initialized in the center of a convection-free domain. The attractive interactions inside the liquid phase cause oscillations in the droplet shape until it reaches the equilibrium spherical format.

### 5.6.1 Methodology

We implement the same procedure described in Section 5.5.1, but  $R_0$  is now a function of the space to provide the elliptical configuration, i.e.,  $R_0^2 = (x - x_c)^2 + (y - y_c)^2$ . If  $y$  is specified,  $x$  is calculated (or vice-versa) from the standard ellipse equation, which reads for a horizontal ellipse:

$$\frac{(x - x_c)^2}{R_{max}^2} + \frac{(y - y_c)^2}{R_{min}^2} = 1, \quad (5.38)$$

where  $R_{max}$  and  $R_{min}$  are the maximum and minimum radius of the ellipse.

The analytical solution considered here to track the droplet radius  $R_{el}$  at an angle  $\theta$  with the horizontal axis is, for a bidimensional domain [103]:

$$R_{el}(\theta, t) = R_{eq} \left( 1 + \varepsilon_n \cos(n\theta) - \frac{\varepsilon_n^2}{4} \right), \quad (5.39)$$

where  $R_{eq}$  is the final equilibrium radius,  $\varepsilon_n = \varepsilon_n(t) < 1$ , and  $n$  is the mode oscillation ( $n = 2$  for an initial elliptic droplet). We set  $R_{max} = R_{el}(\theta = 0, t = 0) = 45$  l.u. and  $R_{eq} = 38$  l.u. From Equation (5.39), we find  $\varepsilon_n(0) = 0.19$  and  $R_{min} = 30.29$  l.u.

One can classify the damping regime as overdamped ( $\Delta'_n > 0$ ), critical ( $\Delta'_n = 0$ ), and underdamped ( $\Delta'_n < 0$ ), depending on  $\Delta'_n$ ,

$$\Delta'_n = \lambda_n^2 - \omega_{n,0}^2 . \quad (5.40)$$

For a bidimensional domain,

$$\lambda_n = \frac{2n(n-1)\mu_l}{\rho_l R_{eq}^2} , \quad (5.41)$$

$$\omega_{n,0} = \sqrt{\frac{n(n-1)(n+1)\gamma_s}{\rho_l R_{eq}^3}} , \quad (5.42)$$

where  $\mu_l$  is the shear viscosity of the liquid phase and  $\gamma_s$  is the surface tension.

We perform the Young-Laplace test for  $T_r = [0.50, 0.70, 0.90]$  to compute  $\gamma_s$ . We initialize a spherical droplet with three different radius  $R_0 = [30, 45, 60]$  following the same procedure in Section 5.5.1, and apply  $Y = Y(T_r)$  as suggested in Section 5.5.2.2. The pressure drop between the phases must present linear dependence with the inverse of the spherical droplet radius  $R_{sp}$ , regarding the Young-Laplace law:

$$\delta p = \frac{\gamma_s}{R_{sp}} . \quad (5.43)$$

## 5.6.2 Results and discussion

Figure 27 reveals the Young-Laplace test. Shan-Chen,  $\beta$ -scheme (or Yang-He), and Kupershtokh *et al.* models yield similar outcomes, including for  $T_r = 0.50$ , where the Shan-Chen model reaches massive errors for the equilibrium vapor densities (see Figure 20(a)). Zhang-Chen model also recovers the Young-Laplace law for  $T_r = 0.90$ , but the points differ from the other models. Evidently, the Young-Laplace tests employing the Zhang-Chen model for  $T_r = 0.70$  and  $T_r = 0.50$  were impracticable due to numerical instabilities. We obtain  $\gamma_s$  as the slope of the lines from the linear regression:  $\gamma_s = 0.0025$  l.u. ( $T_r = 0.90$ ),  $\gamma_s = 0.0154$  l.u. ( $T_r = 0.70$ ), and  $\gamma_s = 0.0334$  l.u. ( $T_r = 0.50$ ).

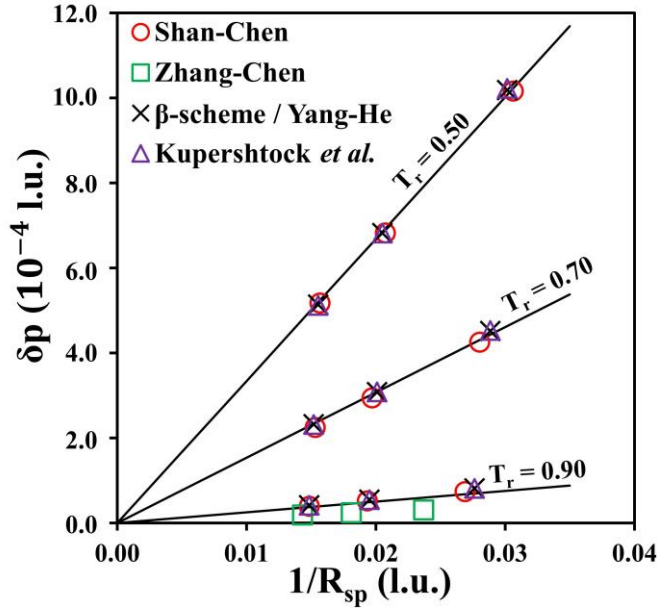


Figure 27: Young-Laplace test for the interaction models considered at  $T_r = [0.50, 0.70, 0.90]$ . Lines are the linear fit of the points.

The surface tension contribution governs the dynamics of the problem over the viscous forces for the three  $T_r$  considered, i.e.,  $\Delta'_n < 0$ . In this case,

$$\varepsilon_n(t) = \varepsilon_{n,max} e^{-\lambda_n t} \cos(\sqrt{-\Delta'_n} t + \zeta_n) , \quad (5.44)$$

where,

$$\varepsilon_{n,max} = \sqrt{\varepsilon_n^2(0) + \left( \frac{\dot{\varepsilon}_n(0) + \lambda_n \varepsilon_n(0)}{\sqrt{-\Delta'_n}} \right)^2} , \quad (5.45)$$

$$\zeta_n = \text{atan} \left( - \frac{\dot{\varepsilon}_n(0) + \lambda_n \varepsilon_n(0)}{\varepsilon_n(0) \sqrt{-\Delta'_n}} \right) . \quad (5.46)$$

The reader can find the equations for the other two types of damping regimes in reference [104].

Figure 28 shows that the LBM with the unified model matches the analytical solution, i.e., Equation (5.39), well and successfully demonstrates the behavior of the underdamped regime, in which the radius of the droplet oscillates with a decaying amplitude until it reaches equilibrium.

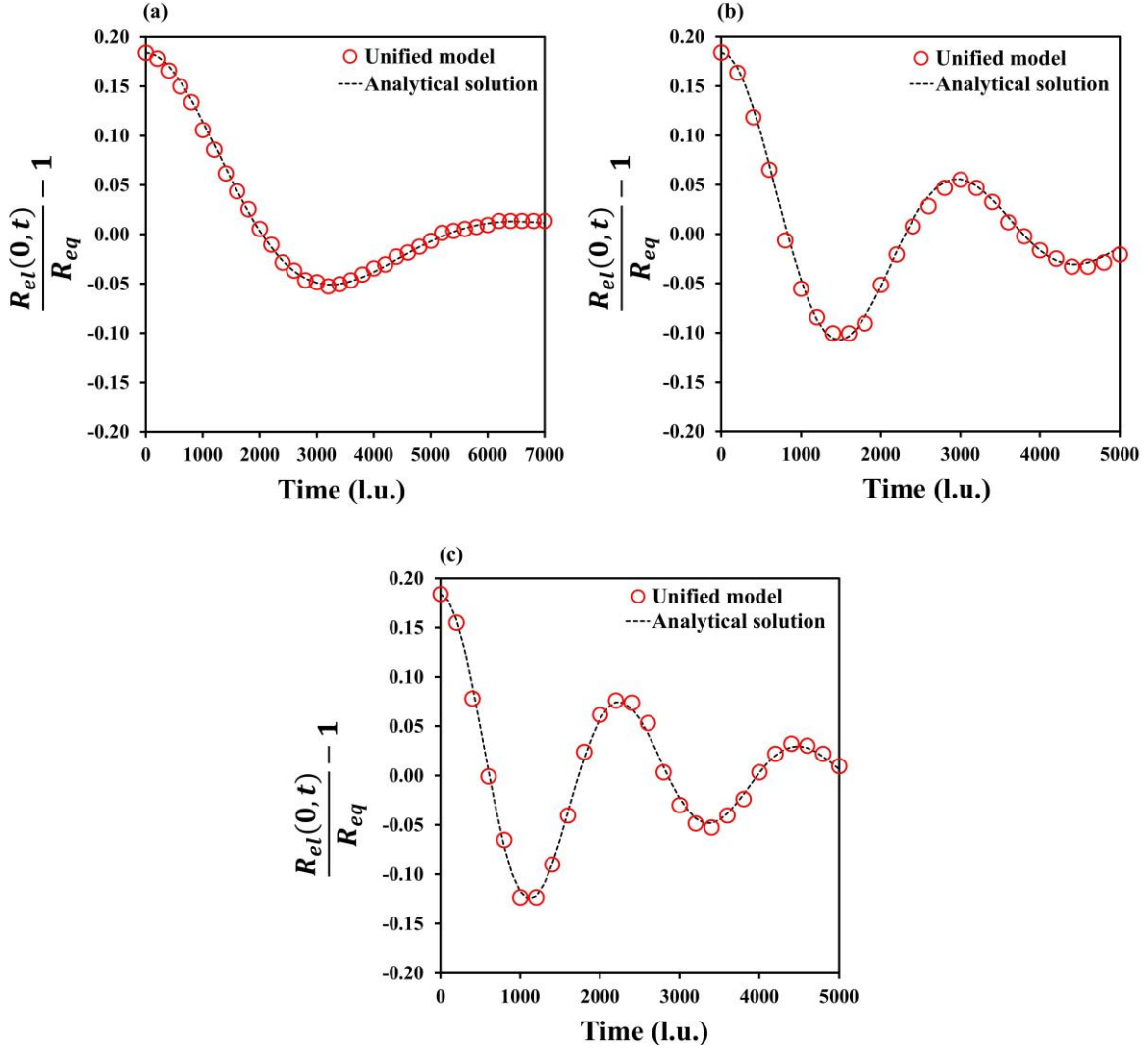


Figure 28: Time evolutions of the elliptic radius for  $\theta = 0$  at (a)  $T_r = 0.90$ , (b)  $T_r = 0.70$ , and (c)  $T_r = 0.50$ . The points were collected at each 200 time steps. We accepted  $\varepsilon_n(0) = 0$  to achieve the analytical solution.

We compute the first period of oscillation as  $T_{p,0} = 2\pi/\omega_{n,0}$ . Figure 29 reveals that the numerical periods are in good agreement with the analytical ones, achieving relative errors lesser than 3.65% regarding the analytical solution. Figures Figure 28 and Figure 29 also demonstrate that the temperature notably affects the first amplitude and the period. This

influence is because these quantities depend on the surface tension, which is dictated by the temperature.

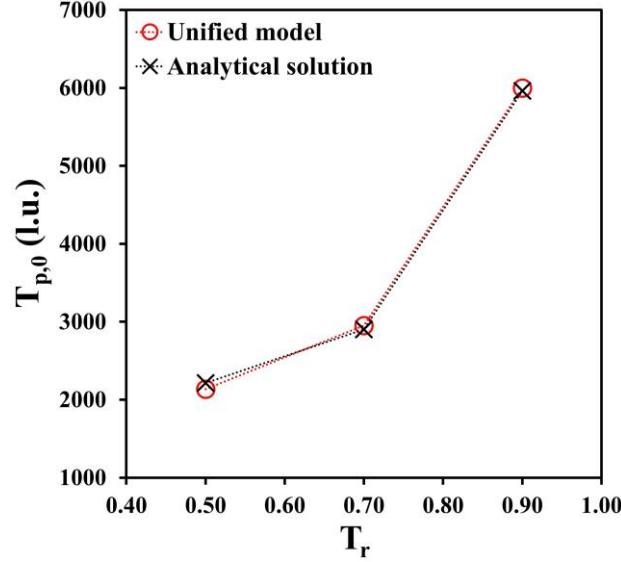


Figure 29: Comparison between the analytical and the simulated initial periods. The lines are plotted to help guide the eye.

Figure 30 presents the velocity maps outside and inside the droplet for  $T_r = 0.50$ . We separated each time step ( $t/T_{p,0} = [0.23, 0.52, 0.80]$ ) into these two cases because the velocity magnitudes inside the droplet are much smaller than outside, hindering the clear visualization of the vector directions if the cases were sketched in only one velocity map. The velocity fields inside the droplet are similar to the results obtained via finite element methods in reference [104].

A few moments after starting the simulations, at  $t/T_{p,0} = 0.23$ , the attractive forces that gather the liquid phase breaks the initial elliptic format to converge the droplet to a spherical shape. This shape adjustment causes the velocity field outside and inside the droplet to rise consistently with the droplet movement, mainly in the axis directions.

At  $t/T_{p,0} = 0.52$ , the droplet already reached its maximum rearrangement and just started contracting again (see  $t = 1100$  in Figure 28(c)). The velocity field inside the droplet is the opposite of the previous step, in agreement with the droplet movement again. However, the velocity vectors outside the droplet stand in the same direction in the central axis lines, as at  $t/T_{p,0} = 0.23$ . The maintenance directions in the exterior field are a consequence of the

droplet contraction in the beginning. Hence, to guarantee physical coherence, the velocity magnitudes rise in the diagonal regions (red dotted square) of the droplet. Nevertheless, we

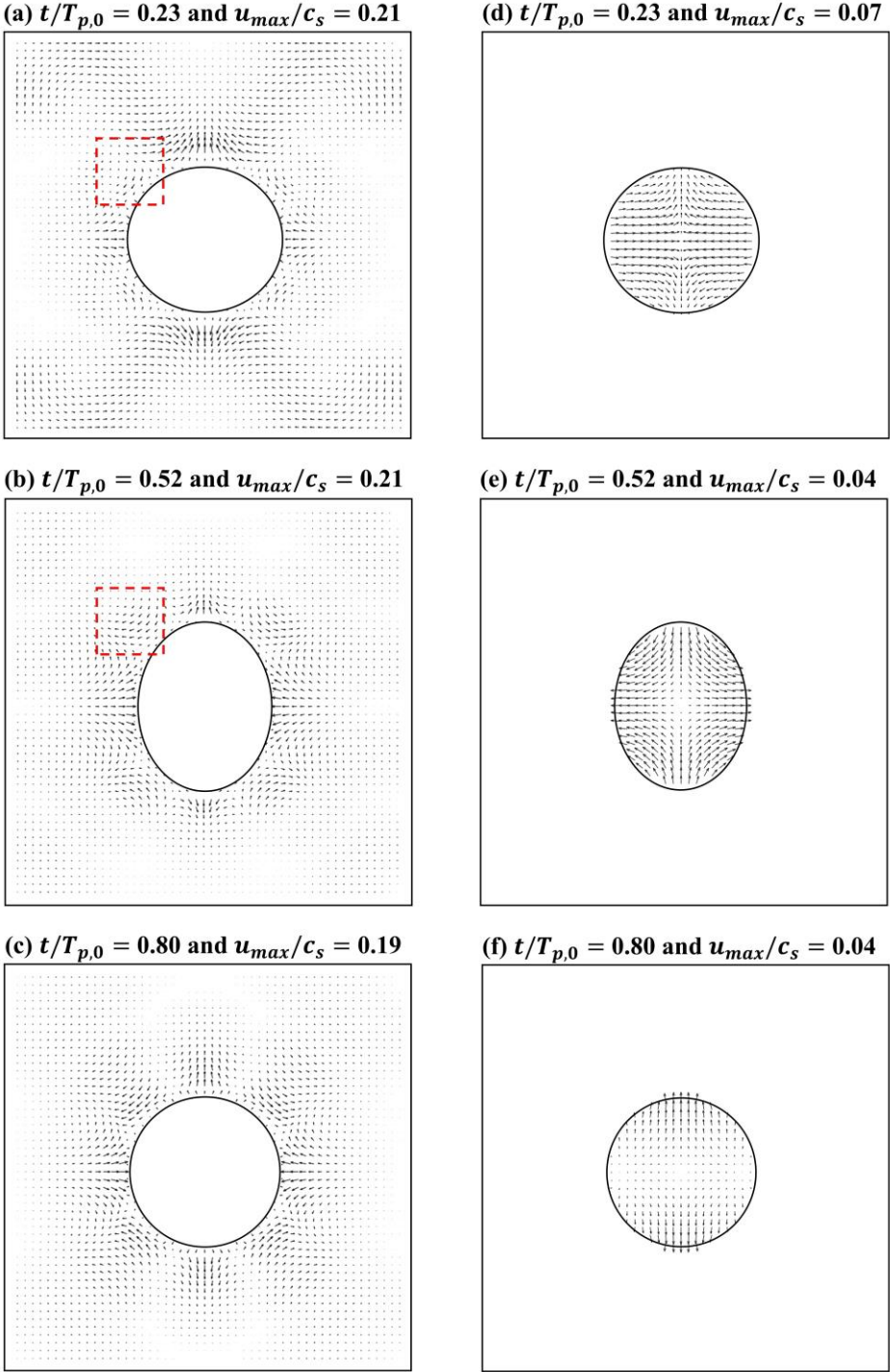


Figure 30: Velocity maps outside (cases (a), (b) and (c)) and inside (cases (d), (e) and (f)) the droplet for  $T_r = 0.50$  at  $t/T_{p,0} = [0.23, 0.52, 0.80]$ .

must highlight that, at  $T_r = 0.50$ , the maximum spurious velocities outside the static droplet observed in Figure 21 present magnitudes ( $u_{max}/c_s \cong 0.2$ ) close to the values seen in Figure 30, becoming impossible a reliable analysis outside the droplets.

Lastly, at  $t/T_{p,0} = 0.80$ , the velocity vectors inside the droplet contradict the droplet movement direction (contraction in the vertical axis). This situation also rises in intermediate stages between  $t/T_{p,0} = 0.23$  and  $t/T_{p,0} = 0.52$ , which we understand as an unphysical deceleration source of the droplet due to the attractive forces inside the liquid phase.

## 5.7 Conclusions

The LBM is becoming a popular choice among engineers to simulate multiphase flows because of its simple interface descriptions. Here we propose a unified model to group five multiphase interaction forces of the pseudopotential approach widely used in the literature: (i) Shan-Chen, (ii) Zhang-Chen, (iii) Kupershtokh *et al.*, (iv) Gong-Cheng, and (v) Yang-He. Although these models are usually considered independent, we have shown that they fall under this more generic single-parameter model. Following careful algebraic manipulations, all these models could be interchanged, and a correlation among their parameters was established. Furthermore, the unified model can make future works more concise and facilitate comparisons between the multiphase interaction models, since they would direct the reader to only one model and tune only one parameter ( $Y$  instead of  $A$ ,  $\beta$  or  $\varepsilon$ ).

We numerically validated the models and demonstrated their performance through two benchmarks: the isothermal stationary and oscillating droplets, both involving a single-component phase transition. The results support what is already addressed in the literature: the extra degree of freedom of the last three alternative models compared to the original Shan-Chen model allows them to mitigate artificial effects in the simulations, such as spurious currents and thermodynamic inconsistency. The interface thickness remained unaffected when the models were varied. The similar density relative errors, spurious

currents fields and magnitudes, interface thickness, and density ratios corroborated the interdependence among the models.

We also observed that even when the parameters are modeled as explicit functions of the reduced temperature,  $T_r$ , simple correlations among the different models remain valid. The inclusion of this temperature dependence improved the thermodynamic consistency without significant losses of stability or increases of spurious velocities and interface thickness. In the dynamic benchmark, the unified model matches well the analytical solution.

# Chapter 6

## Preferential paths of non-Darcy flow

Multiphase conditions are certainly omnipresent in several engineering problems, but its modeling in porous media flows is memorable, mainly because of the petroleum and gas extractions in geological reservoirs. We intend, in the future, to incorporate in porous media studies the unified pseudopotential multiphase model investigated in Chapter 5, but for now, we test an implementation of a single-component fluid flow through an artificial porous media. Hence, Chapter 6 addresses the last part of this dissertation: the LBM performance in porous media flow. Here, we consider a preferential flow problem to understand better the LBM implementation issues in complex geometries.

### 6.1 Introduction

Understanding fluid flow in porous media and mathematically describing its dynamics are still current challenges in research. The relevance of the problem is evidenced by several areas of application, such as EOR in the oil industry [105, 106] and geological and environmental studies [107, 108]. In many cases, one is particularly interested in determining the preferential paths of the flow, which are defined as the higher flow rates in specific sections of the matrix, such as fractures and fingers [109].

Knowledge of the preferential flow allows for the design of microfluidic devices [110, 111], control, and targeted delivery of chemicals [112] and microbes [113], with potential applications in pharmaceutical industries and farming. In soil sciences, preferential flow influences the aeration [114] and contamination of soils [115], and also the formation of subsurface stormflow [116], which causes urban flooding and erosions. Additionally, reservoir oil displacement is optimized when preferential paths are contemplated [117], e.g., through micro- and nanoparticle control [118] in EOR. Hence, an advanced understanding

of the preferential flow dynamics could help develop a theory and spread its applicability in diverse problems.

Preferential flows have several causes, including (i) topological features (e.g., presence of macropores [119] and differences in pore configurations [120]), (ii) physical and chemical properties of the fluid and solid phases along with their interactions (e.g., spatial variability of matrix properties [116], capillarity and surface tension effects), and (iii) flow dynamics (e.g., unstable wetting front [121]). Because of the complexity of the problem, researchers have usually investigated each contribution to establishing their relative importance. Regarding the influence of topology, some authors have identified critical geometry factors for better predictions of the preferential flow, like tortuosity [122], channel size, and pore-to-pore alignment [123].

Ju *et al.* [19] recently proposed and validated a tortuosity-dependent model derived from the Darcy law to predict the preferential trajectories in porous media. However, the geometry features have been mostly restricted to creeping flows with extremely low Reynolds numbers (i.e., the flow rate is a relevant factor [124]). Since the preferential flow depends on several aspects, the current literature still lacks a unifying or generalized theory to determine it [125].

Some works experimentally evaluate the preferential paths through tracer tests [124, 126] or measurements of isotope signatures [127, 128]. However, experimental investigation of preferential flows is often problematic because it causes clogging and interferes with the flow patterns [129], decreasing permeability [130] and changing the outlet pressure [131]. Hence, a helpful alternative is the use of theoretical modeling and simulation.

Depending on the length scale, there are two major modeling approaches for porous media flow: the Representative Element Volume (REV) [132] and the Pore-Scale [133] approaches. The macroscopic properties (e.g., permeability) and continuum models using standard computational fluid dynamic tools characterize the REV simulations. With its connections and discrete models at a microscopic level, the proper matrix is treated in Pore-Scale simulations [3]. REV is easy to implement but uses semi-empirical models (e.g., drag forces), oversimplifies the descriptions, and fails to provide local information about the flow, which is crucial for preferential flow determination. Pore-Scale is precise and detailed, but it is also computationally expensive [3, 4].

LB emerges as a powerful and computationally efficient method to model flows through porous media [4]. Rothman [134] presented one of the first works about LBM in porous media flow. Since then, several works applying LBM have appeared in the literature, e.g., the effects of pore configuration in the flow [135, 136], non-Darcy flow description [137], thermal flows modeling in porous media [138], multiphase flows [139], and so on [3]. REV-LBM, the most popular approach in the literature, represents the porous media through a resistance field model [4]. One successful example is the Guo-Zhao model, which proposed adding the porosity and a forcing term in the LB methodology [140]. Nevertheless, it still relies on macroscopic empirical models, and it is unsuitable for the preferential flow determination problem.

Hence, in this work, we use the Pore-Scale LBM simulations to investigate the geometry and topological effects of the matrix on the preferential flow configuration. First, we validate the Pore-Scale LBM by showing that the numerical results accurately recover the Forchheimer empirical model. Next, focusing on such systems still in the laminar regime but distant from creeping conditions, we show that the Darcy resistance model proposed by Ju *et al.* [19] becomes unreliable. Besides tortuosity, the grain shape and relative orientation also become relevant topological features of the problem. Finally, the Pore-Scale LBM approach demonstrates that clogging of specific pores may obstruct several unclogged pores, creating dead zones (zero flow) in the porous media.

## 6.2 Theoretical description

### 6.2.1 Physical properties

Reynolds number ( $Re$ ) is a dimensionless parameter frequently used to identify the flow regime type by recognizing the balance of inertial and viscous forces. Especially for flows through porous media,  $Re$  can be defined using the Blunt diameter as the characteristic length ( $l_c$ ),

$$Re = \frac{\rho |\vec{u}| l_c}{\mu}, \quad (6.1)$$

$$l_c = \frac{\pi V_b}{A_w}, \quad (6.2)$$

where  $\mu$  is the shear viscosity,  $\vec{u}$  is the macroscopic velocity,  $\rho$  is the macroscopic density,  $V_b$  is the total volume of the porous media, and  $A_w$  is the wetted surface [122, 141].

Additionally, some relevant physical properties characterize the porous media, as permeability, porosity, and tortuosity. The permeability  $K$  measures how easy it is for any fluid, independent of its properties, to percolate the porous pattern. It is generally associated with the fraction of space without solids in the matrix, i.e., the porosity or voidage [142]. Among different types of porosity, we can identify the overall porosity ( $\phi_o$ ) as the ratio between the void ( $V_v$ ) and bulk volumes ( $V_b$ ) of the porous media [143],

$$\phi_o = \frac{V_v}{V_b}, \quad (6.3)$$

and the effective porosity ( $\phi_e$ ) as the fraction that quantifies only the regions with volume  $V_{flow}$  that cooperate with the flow [122],

$$\phi_e = \frac{V_{flow}}{V_b}. \quad (6.4)$$

Although the permeability and porosity are related to the flow magnitude, in this work, we consider the tortuosity  $\tau_{tort}$  as the most crucial matrix property to predict the preferential flow. It measures how sinuous the trajectories are inside a porous medium and can be defined as  $\tau_{tort} = L_e/L$ , where  $L_e$  is the sinuous length through the porous structures, and  $L$  is the linear distance from inlet to outlet of the media [144]. The reader will better understand the relevance of this geometrical parameter on preferential flow in Section 6.2.2.

## 6.2.2 Governing equations in porous media

In systems described by small  $Re$  (i.e., Stokes or creeping flows), only viscous forces control the flow [142, 145]. In this case, the velocity is directly dependent on the pressure drop and inversely dependent on the matrix length, as suggested by the Darcy law,

$$\vec{\nabla} p = -\frac{\mu}{K} \vec{u} . \quad (6.5)$$

Equation (6.5) is the most straightforward equation for modeling one-phase flow in porous media. Its integral form evidences more clearly the effects of the pressure  $p$  and the porous media length  $L_{PM}$  to the velocity flow,

$$|\vec{u}| = \frac{K \delta p}{\mu L_{PM}} . \quad (6.6)$$

Because the velocity must be inversely dependent on the flow resistance  $G_{flow}$ , we can define  $G_{flow} = \mu L_{PM}/K$  [19]. Given, however, that the permeability of the matrix is usually a function of tortuosity [144, 146], the flow resistance through a uniform cross-sectional area can be written in the following form,

$$G_{flow} = C \mu L_{PM} \tau_{tort}^2 , \quad (6.7)$$

where  $C$  is a constant related to the chosen permeability model. Here, we identify Equation (6.7) as the Ju *et al.* model, since it is similar to the Darcy flow resistance equation derived in their work [19]. When modeling a specified fluid through settled porous structures, the fluid and matrix properties are fixed. Consequently, the flow resistance is only dependent on the tortuosity. In these conditions, small tortuosities (i.e., small flow resistances) indicate the preferential paths of the porous medium.

As the flow rate increases, the inertial forces become more and more accentuated, causing regions of greater  $Re$  to arise and disabling the application of the Darcy law. In this

case, the Forchheimer equation is a semi-empirical model that seeks to describe the further complexity of flow through porous media for systems with larger  $Re$ . The resistance, hence, admits contributions from both viscous forces (first term) and inertial forces (second term) [145],

$$-\vec{\nabla}p = \frac{\mu}{K} \left( 1 + \frac{\beta_F \rho K}{\mu} |\vec{u}| \right) \vec{u}, \quad (6.8)$$

where  $\beta_F$  is a constant which, despite some model proposals to predict it [147], is usually obtained empirically. The Forchheimer equation recovers the Darcy law at small  $Re$  when the second term is much smaller than the first term, i.e., when  $\beta_F \rho K |\vec{u}| / \mu \ll 1$ . Thus, it is convenient to give a proper name to this dimensionless term: the permeability Reynolds number  $Re_K = \beta_F \rho K |\vec{u}| / \mu$ . Hence, when  $Re_K \ll 1$ , the inertial contributions become unimportant, and the Forchheimer equation reduces to the Darcy law [145, 148].

Again, to inspect the dependency of the velocity with the pressure gradient, the Forchheimer equation can be rewritten in a more attractive form when we define the apparent permeability  $K_{app} = -\mu |\vec{u}| / |\vec{\nabla}p|$  [149],

$$\frac{1}{K_{app}} = \frac{1}{K} + \frac{\beta_F \rho |\vec{u}|}{\mu}, \quad (6.9)$$

which provides a linear relationship between the velocity  $\vec{u}$  and  $1/K_{app}$  [150].

### 6.3 Methodology

Here, we consider an artificial square porous media of length  $L_{PM} = 1mm$ , as shown in Figure 31. To work with paths with similar areas but also with irregularities and sudden flow changes, we generated the porous structure from a freehand sketch and further converted it into a binary file ( $366 \times 366$ ), which became the numerical simulation input. Water at

25°C ( $\rho = 0.997 \text{ g/cm}^3$ ,  $\mu = 0.890 \text{ cP}$ , and  $\kappa = 2.4 \text{ cP}$  [148]) was initialized as a stationary fluid. The single-component flow was ensured by ten pressure drops equivalent to different heights of water column  $H = [2 \text{ m}, 20 \text{ m}]$  with 2 m increments.

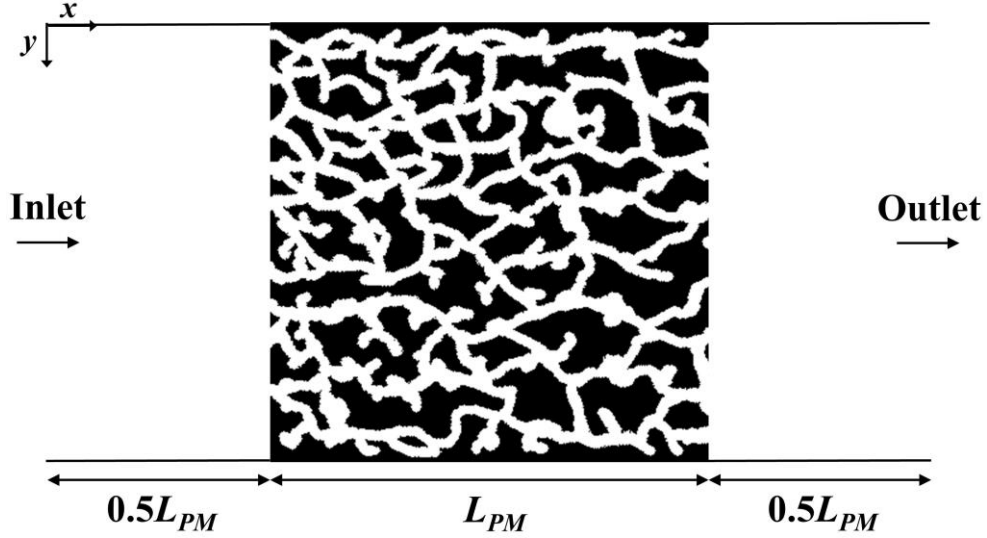


Figure 31: Simulated domain with artificial porous media. White and black areas represent, respectively, fluid and grain regions, while  $L_{PM}$  is the length of the porous medium.

The LBM was implemented with  $\delta x = 1$ ,  $\delta t = 1$ , and the D2Q9 model with no additional forces. Again, we write our codes in C/C++ to ensure fast LBM calculations. The illustrative images are produced using the open-access software GNU Octave 5.1.0 [101]. We considered  $\bar{\rho} = 1$  to adopt the periodic condition with pressure variation in the open boundaries (inlet and outlet in Figure 31). When velocity waves reached  $x = 2L_{PM}$  (Figure 32), the simulations were interrupted to prevent the outflow from affecting the inlet of the porous media. At this stage, the velocity profile inside the porous media has already converged.

Given that fluid properties are assumed constant, and the minimum areas of each channel are considered similar, only the tortuosity governs the preferential path. Therefore, we used Equation (6.7) to investigate the preferential flow and compare initial predictions to simulation results. Since the preferential paths coincide with the channels that develop the highest flow velocities [124], we measured the main paths by evaluating the velocity field.

Figure 33 enumerates pores and outlets for identification, while Table 2 lists a few specific routes in the matrix. The overall route is identified with the notation “number-letter”,

where the number is the inlet, and the letter is the outlet. From Equation (6.7), the smallest resistance  $G$  (smallest  $\tau_{tort}^2$ ) reveals the preferential paths (in red) for each overall route. The tortuosities were calculated by evaluating the proportion  $\tau_{tort} = L_e/L_{PM}$ .

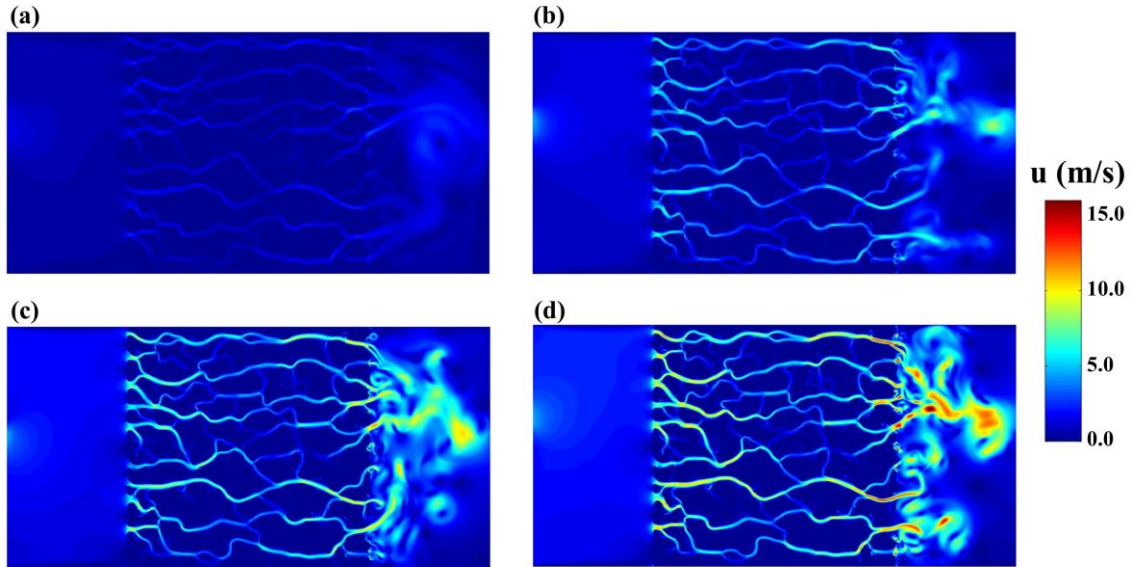


Figure 32: Simulated velocity field for varied heights of water column: (a) 2 m, (b) 8 m, (c) 14 m and (d) 20 m.

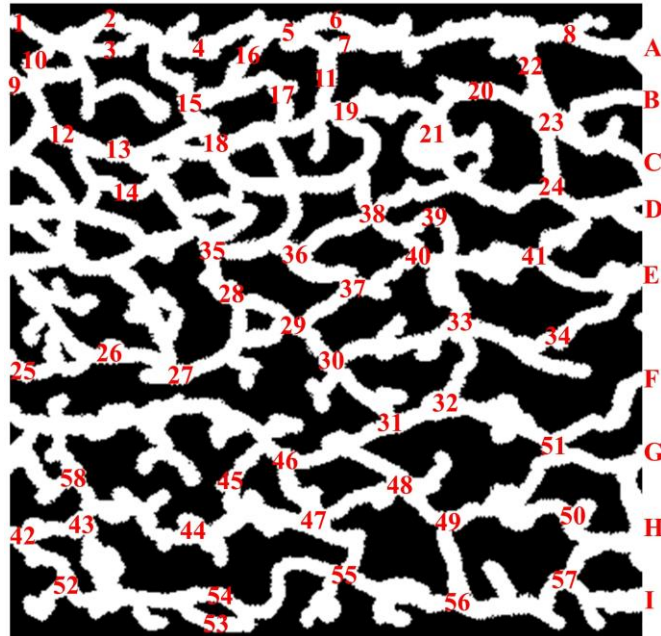


Figure 33: Identification of the nodes, inlets and outlets in the considered porous media.

Table 2. Investigated paths from the given porous media. The preferential paths predicted from Equation (6.7) are in red. The numbers and letters are established in Figure 33.

Paths	$\tau_{tort}^2$	Paths	$\tau_{tort}^2$	Paths	$\tau_{tort}^2$	Paths	$\tau_{tort}^2$
<b>1 - A</b>		<b>1 - C</b>		<b>25 - E</b>		<b>42 - H</b>	
1 - 2 - 4 - 5 - 6 - 8 - A	1.17	1 - 2 - 4 - 5 - 6 - 22 - 23 - C	1.42	25 - 26 - 27 - 29 - 30 - 33 - 34 - E	1.07	42 - 43 - 44 - 47 - 55 - 56 - 57 - H	1.35
1 - 2 - 4 - 5 - 7 - 8 - A	1.17	1 - 2 - 4 - 5 - 7 - 22 - 23 - C	1.42	<b>25 - F</b>		42 - 43 - 44 - 47 - 48 - 49 - 56 - 57 - H	1.48
1 - 3 - 4 - 5 - 6 - 8 - A	1.17	1 - 3 - 4 - 5 - 6 - 22 - 23 - C	1.42	25 - 26 - 27 - 29 - 30 - 31 - 32 - 51 - F	1.31	42 - 52 - 54 - 55 - 56 - 57 - H	1.44
1 - 3 - 4 - 5 - 7 - 8 - A	1.17	1 - 3 - 4 - 5 - 7 - 22 - 23 - C	1.42	<b>42 - F</b>		42 - 52 - 53 - 55 - 56 - 57 - H	1.44
1 - 2 - 15 - 17 - 11 - 8 - A	1.47	1 - 2 - 4 - 5 - 11 - 19 - 20 - 23 - C	1.42	42 - 43 - 44 - 45 - 46 - 31 - 32 - 51 - F	1.35	42 - 43 - 54 - 55 - 56 - 57 - H	1.53
<b>1 - B</b>		1 - 3 - 4 - 5 - 11 - 19 - 20 - 23 - C	1.42	42 - 43 - 44 - 47 - 48 - 49 - 51 - F	1.35	42 - 43 - 53 - 55 - 56 - 57 - H	1.52
1 - 2 - 4 - 5 - 6 - 22 - 23 - B	1.40	1 - 2 - 15 - 17 - 19 - 20 - 23 - C	1.37	42 - 43 - 44 - 45 - 46 - 48 - 49 - 51 - F	1.55	42 - 43 - 44 - 47 - 48 - 49 - 50 - H	1.24
1 - 2 - 4 - 5 - 7 - 22 - 23 - B	1.40	1 - 3 - 15 - 17 - 19 - 20 - 23 - C	1.37	42 - 43 - 44 - 45 - 46 - 47 - 48 - 49 - 51 - F	1.65	42 - 43 - 44 - 45 - 46 - 48 - 49 - 50 - H	1.52
1 - 3 - 4 - 5 - 6 - 22 - 23 - B	1.40	1 - 2 - 15 - 18 - 19 - 20 - 23 - C	1.42	<b>25 - G</b>		42 - 43 - 44 - 45 - 46 - 47 - 48 - 49 - 50 - H	1.55
1 - 3 - 4 - 5 - 7 - 22 - 23 - B	1.40	1 - 3 - 15 - 18 - 19 - 20 - 23 - C	1.42	25 - 26 - 27 - 29 - 30 - 31 - 32 - 51 - G	1.35	<b>42 - I</b>	
1 - 2 - 4 - 5 - 11 - 19 - 20 - 23 - B	1.42	1 - 10 - 12 - 13 - 18 - 19 - 20 - 23 - C	1.57	<b>42 - G</b>		42 - 43 - 44 - 47 - 48 - 49 - 56 - 57 - I	1.42
1 - 3 - 4 - 5 - 11 - 19 - 20 - 23 - B	1.42	<b>25 - D</b>		42 - 43 - 44 - 45 - 46 - 47 - 48 - 49 - 51 - G	1.53	42 - 43 - 44 - 47 - 55 - 56 - 57 - I	1.30
1 - 2 - 15 - 17 - 19 - 20 - 23 - B	1.35	25 - 26 - 27 - 29 - 37 - 40 - 41 - D	1.42	42 - 43 - 44 - 45 - 46 - 48 - 49 - 51 - G	1.44	42 - 52 - 53 - 55 - 56 - 57 - I	1.39
1 - 3 - 15 - 17 - 19 - 20 - 23 - B	1.35	<b>25 - E</b>		42 - 43 - 44 - 45 - 46 - 31 - 32 - 51 - G	1.39	42 - 52 - 54 - 55 - 56 - 57 - I	1.39
1 - 2 - 15 - 18 - 19 - 20 - 23 - B	1.40	25 - 26 - 27 - 29 - 37 - 40 - 41 - E	1.28	42 - 43 - 44 - 47 - 48 - 49 - 51 - G	1.24	42 - 43 - 53 - 55 - 56 - 57 - I	1.46
1 - 3 - 15 - 18 - 19 - 20 - 23 - B	1.40	25 - 26 - 27 - 29 - 37 - 40 - 33 - 34 - E	1.39			42 - 43 - 54 - 55 - 56 - 57 - I	1.46

The lattice volume correspondent to a node at  $(x, y)$  with an axial lattice velocity  $|\vec{u}_{x_{\text{node}}}| > 0.0005 \text{ l.u.} \cong \text{mean velocity}/2$  is taken as  $V_{\text{flow}}$  for the effective porosity calculation. That is,

$$\phi_e = \frac{(\delta x)^2 \sum_{x,y}^{N_x, N_y} b(x, y)}{V_b}. \quad (6.10)$$

where  $N_x$  and  $N_y$  are the total numbers of lattice nodes in the  $x$  and  $y$  directions, and  $b(x, y)$  is a Boolean variable ( $b(x, y) = 1$  if  $|\vec{u}_{x_{\text{node}}}| > 0.0005 \text{ l.u.}$ , or  $b(x, y) = 0$  otherwise).

## 6.4 Results and discussion

### 6.4.1 Preferential paths through porous structures

The ten heights studied generated a Reynolds range of  $Re = [55.4, 274.2]$ . Some recirculation zones are seen in Figure 32, which are related to the transition between porous and non-porous regions and the isolated grains near outlets D and G. Their magnitude and location behind the porous media vary with pressure. This emphasizes that there are substantial modifications to the flow dynamics in this region, which has also been recently observed and reported in the literature [151].

To validate the LB-MRT method with the Pore-Scale approach, we plotted in Figure 34 the relationship between the inverse of the apparent permeability ( $K_{app}$ ) and the average velocity for the ten initial cases studied here. A linear regression of the data shows that the method recovers the linearized Forchheimer equation ( $1/K_{app} = (0.72 |\vec{u}| + 1.37)10^{10}$ ) with a strong correlation ( $R^2 = 0.998$ ) and a permeability of  $K = 0.76 \text{ \AA}^2$ . Additionally, the Blunt diameter and the overall porosity are, respectively,  $l_c = 0.08 \text{ mm}$  and  $\phi_o = 0.45$ , while the effective porosity fluctuates around  $\phi_e \cong 0.34$ .

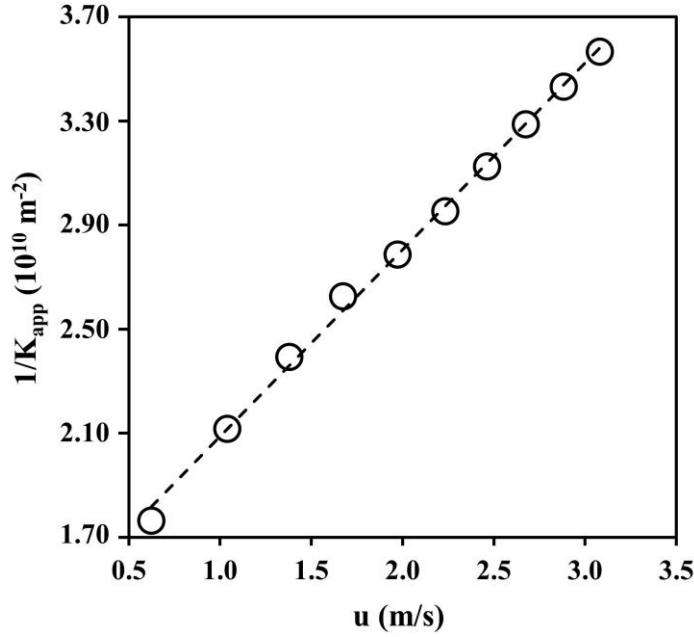


Figure 34: Linear regression of the calculated points (circles) with the linearized Forchheimer equation (dashed line):  $\frac{1}{K_{app}} = (0.72|\vec{u}| + 1.37)10^{10}$  with  $R^2 = 0.998$ .

Having established the matrix physical properties and flow characteristics, the discussion about preferential flow will focus on a sample case at  $H = 10\text{ m}$  with  $Re_K = 1.11 \sim 1$ , which suggests that the inertial forces contribute to describing the flows in our simulations (Forchheimer regime).

The flow profile for  $H = 10\text{ m}$  (Figure 35) confirms that most paths agree with the theoretical prediction in Table 2. However, the overall paths 1-B and 1-C are different from the predicted results since pore 15 would be preferred (Table 2) because of its lower tortuosity. Instead, in the simulation, the velocity field indicates that the path 1-2-4-5-6/7-22-23-B/C, and, consequently, pore 4, is preferred. Next, 22 is the pore chosen to get to the outlets B or C, unless the velocities in pore 15 had been higher than in pore 22. Because path 1-A locally presents the smallest flow resistance (i.e., path 1-A is preferred in the top region of the matrix), the associated velocity field affects the overall paths 1-B and 1-C and changes the pore preference. Indeed, the grain pattern also plays a role in this scenario, but the configuration effect is more easily observed in pores 2 and 3, as discussed next.

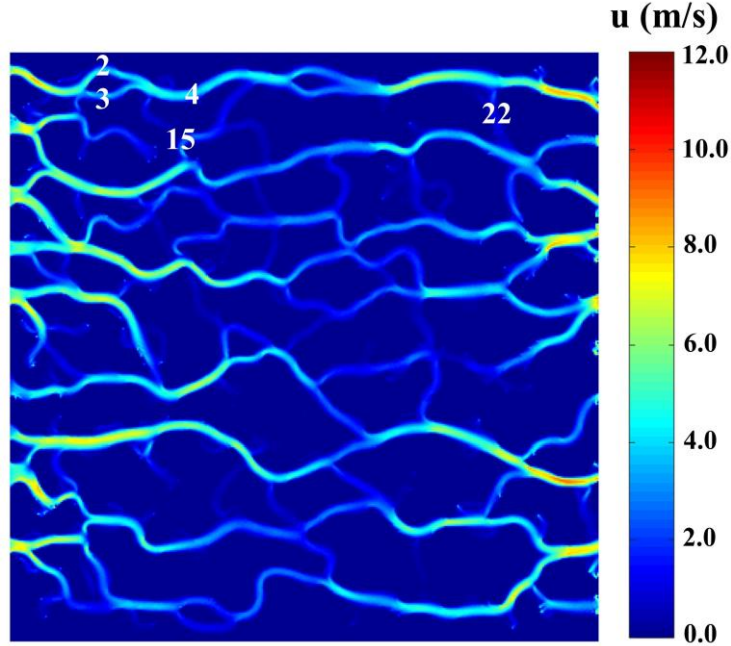


Figure 35: Velocity field of the flow simulation for  $H = 10$  m in the original porous media.

Figure 35 indicates that pore 2 is favored in path 1-A, but Equation (6.7) was incapable of discerning which pore (2 or 3) is preferred. One could argue that the channel area (neglected in the calculation) is the reason for this discrepancy. However, the number of lattice nodes is equal in both pores, i.e., the smallest areas that delimit the flow are the same. Thus, the resistance expressed by Equation (6.7) indeed depends only on the tortuosity. Since the tortuosity of both channels is also similar, it is the grain shape that influences locally the pore that is preferred.

Thus, a controlled flow configuration sketched in Figure 36(a) was simulated to investigate the importance of the local shape. The artificial pore region has a solid triangle at the center with length  $L = 100$  lattice nodes. The two dashed rectangles in Figure 36 (b) indicate regions with the same lattice area of  $3L/5$ , through which the fluid must stream and where the velocity magnitudes can be compared. Although Equation (6.7) predicts that the path under the triangle ( $\tau_{tort}^2 = 1.13$ ) is favored rather than the one above it ( $\tau_{tort}^2 = 1.28$ ), Figure 36(b) shows that the velocities are higher in the dashed rectangle at the top. Thus, the route above the triangle is favored.

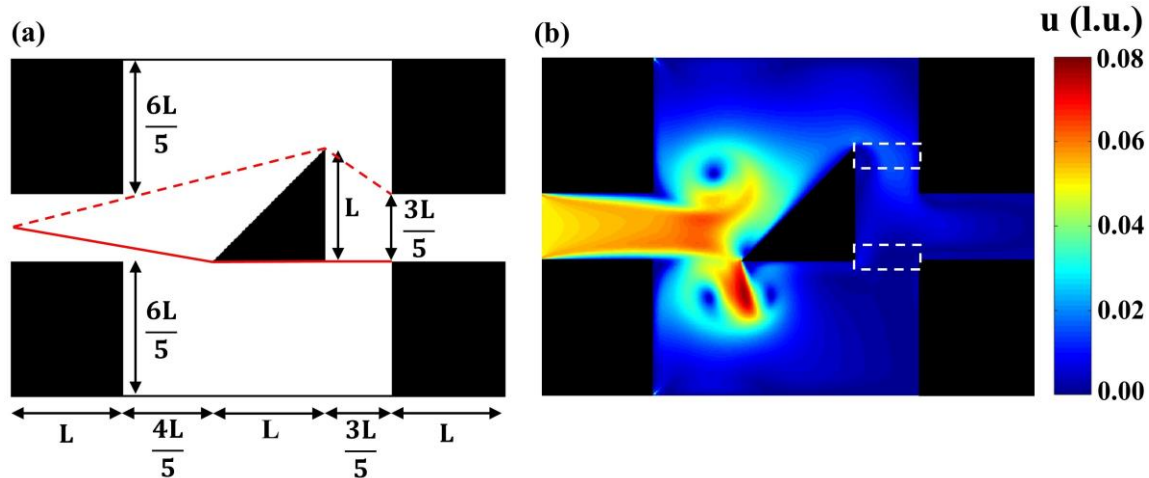


Figure 36: Flow simulation through a rectangular pore with a triangle with length  $L$  in the center. The sketch is presented in (a), where the solid (—) and dashed (---) lines are the shortest paths passing under and above the triangle, respectively. The flow is presented in (b), where the white rectangles specify the two regions that have the same area.

Therefore, both the pore configuration and its orientation relative to the velocity profile are crucial to determining which path will be chosen, even in the laminar regime. Additionally, some small recirculation zones can emerge in the pore due to entrainment, jet effects, and transitional regimes, affecting the preferential paths. These drawbacks make Equation (6.7) unviable to predict the preferential flow in the Forchheimer regime accurately, but it is sufficient to discern what are the main possible trajectories.

### 6.4.2 Flow with clogging

Finally, we obstructed some sections of Figure 33, as seen in Figure 37(a) and (b), and simulated the flow again. When A is blocked, the path 1-2-4-5-6/7-22-23-B/C is preferred. This reinforces what was previously discussed: pore 15 is disfavored, rather than pore 4 when 1-B/C is the overall path considered. Although A is the preferential outlet at the top of the matrix, the flow in the neighbor routes keeps slightly unchanged when A is closed.

On the other hand, when E is obstructed, many routes have their flow locally changed. The flow through connections 33-34 and 33-40 almost disappears, while also decreasing in 40-41. Although D would perhaps be the intuitive path for being the nearest outlet, both simulation and theory indicate that this path is not preferred. Instead, F and G are the preferential outlets when 25 is the inlet.

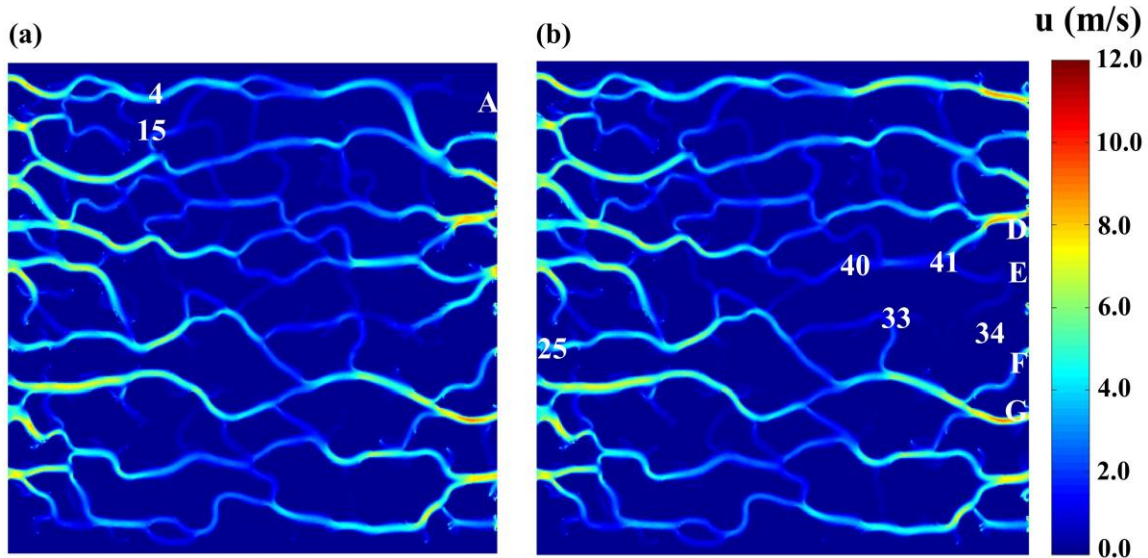


Figure 37: Velocity field of the flow simulation with  $H = 10\text{ m}$  and the outlets (a) A and (b) E closed.

Figure 38 also gathers a set of closed pores. We demonstrated before that pore 4 is favored rather than pore 15. However, pore 4 is blocked in Figure 38(a) and pore 15 is now favored. Even so, the connection 15-17 is still disfavored to reach outlets B and C. The flow is ensured in the connection 15-16, and, then, keep the preferred path to attain A. Alternatively, if we try to close pore 5, as displayed in Figure 38(b), the flow shrinks in pore 15, raises in 16-17, and prefers connection 17-11-7 to get to the outlet. Again, these results disagree with those in Table 2 and disqualify the Equation (6.7) prediction ability for the Forchheimer regime since the flow chooses to stream through a higher tortuous path (17-11-7) rather than take path 17-19-20.

Next, pore 32 is closed in Figure 38(c). This case validates that the velocity fields in the connections 49-51 and 49-50 are similar, as expected from Table 2, since the overall preferential paths 42-G and 42-H present comparable  $\tau_{tort}^2$ . Because of pore 32 being obstructed, the flow in 31 and 51-F shrinks, which demonstrates that the outlet F drastically loses its applicability because the main contribution to the flow in F comes from pore 32.

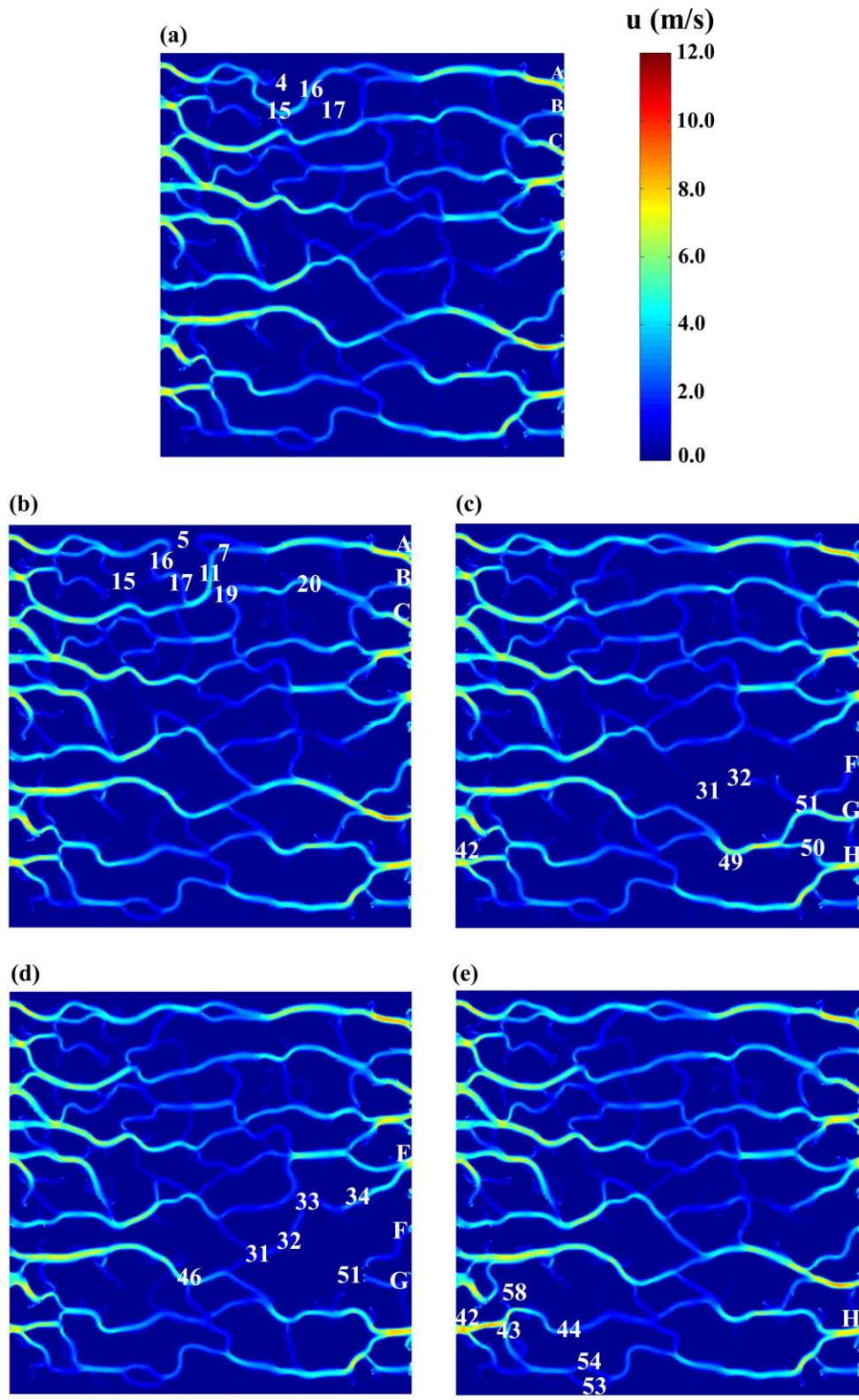


Figure 38: Velocity field of the flow simulation with  $H = 10\text{ m}$  and the nodes (a) 4, (b) 5, (c) 32, (d) 51 and (e) 58 closed.

If pore 51 is obstructed instead, not only F loses its utility but also G, as observed in Figure 38(d). This case illustrates the formation of dead zones near the obstructed pore. Since the flow is close to zero in these regions, it could, e.g., reinforce the surface runoff in soils or even influence the displacement of oil in geological reservoirs. On the other hand, we can also note in Figure 38(d) that 31-32-33-34 is a critical path to reach outlet E from pore 46. Similarly, the obstructed pore 58 in Figure 38(e) indicates that the connection 43-44 is preferred rather than 43-54/53, which ensures 42-43-44-47-48-49-50-H is the preferential path from pore 42, in agreement with Table 2.

## 6.5 Conclusions

Preferential flow is a phenomenon that affects a vast range of problems and needs to be better understood. Because of the attractive advantages of LBM in the Pore-Scale approach (e.g., straightforward no-slip boundary conditions and absence of empirical models), LB is an inviting method to model the flow in porous media and search for preferential pathways. A typical and simplified numerical way to predict these paths is through the geometric investigation of the matrix. Hence, in this work, we tested the Ju *et al.* model, a tortuosity-dependent resistance model, to measure the preferential paths in a non-Darcy flow through an artificial square porous medium.

LBM naturally recovers the Forchheimer equation for the established range of Reynolds. The Ju *et al.* model successfully indicates many preferential paths, but its accuracy is more substantial for Darcy flows. This deficiency is related to the inertial effects in the Forchheimer regime, which the model does not contemplate. Therefore, geometric characteristics like grain shape and pore-to-pore alignment (deflections of the paths) are highlighted features to describe this kind of flow. When clogging occurs, the divergence of some predictions is more noticeable. Additionally, depending on the position of the blocked pores, the flow configuration can change locally, the preferred paths can be modified, and other unblocked pores (common neighbors of the blocked pore) may become useless for the flow, which originates dead zones in the matrix.

# Chapter 7

## Final remarks

Chapters 3, 5, and 6 address the three independent parts of this dissertation. In this chapter, we present a brief overview of them and suggest some future relevant LB outlooks. The reader, however, finds more specific details about the concluding remarks in Sections 5.7 and 6.5.

### 7.1 Work contributions

Initially, in Chapter 3, we meticulously prove through asymptotic analysis that the continuity and the Navier-Stokes equations are recovered from BGK-LBE for low  $Ma$ . As a result, Chapter 3 stands as a didactic and reliable section to demonstrate the transport equations derivation and master mathematical analysis to test LB models. The connection between the mesoscale modeling and the macroscopic properties is ensured through the relaxation time and the kinematic fluid viscosity.

In Chapter 4, we validate our computational implementation by demonstrating two frequent benchmarks (the Couette and square-cavity flows) and used the algorithm as the base for the LBM implementation in the consecutive sections. Then, Chapter 5 proposes and validates the unified pseudopotential model, making future works more concise and facilitating comparisons between the multiphase interaction models. Depending on the parameter, we demonstrate the unified model recovers the (i) Shan-Chen, (ii) Zhang-Chen, (iii) Kupershtokh *et al.*, (iv) Gong-Cheng, and (v) Yang-He models. The unified parameter is explicitly expressed as a function of the reduced temperature, causing a higher thermodynamic consistency.

To implement the unified model in further multiphase works, we consider an independent preferential flow implementation as a starting point. Chapter 6 carries out an LB

Pore-Scale approach to explore preferential paths, from which the Forchheimer equation is recovered. The evaluated Ju *et al.* model predicts many preferential paths correctly, but the grain shape and relative orientation decrease its accuracy when inertial effects are relevant. Furthermore, clogging affects the flow locally, changes the preferential paths, and creates dead zones in the porous media flow.

Finally, LBM presents some advantages (e.g., parallel performance and straightforward boundary conditions) that make it suitable for various engineering problems and justify its progress in several areas. This dissertation is an example of how valuable the LBM is to reproduce multiphase problems and flows in complex geometries. We hope this work can help to develop the method and to attract attention to the mesoscale modeling.

## 7.2 Future works

We aim to develop further applications of the unified model in relevant multiphase problems and investigate its stability in a three-dimensional domain. We expect to model the porous media flow in a real matrix, incorporating multiphase flow (e.g., EOR), mixing, fluid-structure interactions, and heat transfer. We highlight some other pertinent LBM outlooks that we are interested in, such as:

- the insertion of more robust EOS, e.g., CPA and SAFT in the pseudopotential model;
- the modeling of reactive flows to track, e.g., the dissolution of solid structures inside a porous media;
- the coupling of the multiphase pseudopotential approach with turbulent models;
- the modeling of vapor condensation inside porous media using LBM exclusively, and the insertion of capillary effects and other thermodynamic phenomena;
- the assurance of the thermodynamic consistency of multicomponent systems;
- the modeling of liquid-vapor and liquid-liquid equilibria through pseudopotential models, answering, e.g., how to link the relative volatility to the kinetic theory;
- and the development of methodologies that gather machine learning with LBM.

# References

- [1] MCNAMARA, G., ZANETTI, G. "Use of the Boltzmann Equation to Simulate Lattice-Gas Automata," *Phys. Rev. Lett.*, vol. 61, no. 20, pp. 2332-2335, 1988.
- [2] HIGUERA, F., SUCCI, S., BENZI, R. "Lattice Gas Dynamics with Enhanced Collisions," *Europhys. Lett.*, vol. 9, no. 4, pp. 345-349, 1989.
- [3] SHARMA, K., STRAKA, R., TAVARES, F. "Lattice Boltzmann Methods for Industrial Applications," *Ind. Eng. Chem. Res.*, vol. 58, pp. 16205-16234, 2019.
- [4] HE, Y., LIU, Q., LI, Q., *et al.* "Lattice Boltzmann methods for single-phase and solid-liquid phase-change heat transfer in porous media: A review," *International Journal of Heat and Mass Transfer*, vol. 129, pp. 160-197, 2019.
- [5] MURADOGLU, M., TRYGGVASON, G. "A front-tracking method for computation of interfacial flows with soluble surfactants," *J. Comput. Phys.*, vol. 227, no. 4, pp. 2238-2262, 2008.
- [6] DIETER-KISLING, K., MARSCHALL, H., BOTHE, D. "Direct numerical simulation of droplet formation processes under the influence of soluble surfactant mixtures," *Computers & Fluids*, vol. 113, pp. 93-105, 2015.
- [7] THEODORAKAKOS, A., BERGELES, G. "Simulation of sharp gas-liquid interface using VOF method and adaptive grid local refinement around the interface," *International Journal for Numerical Methods in Fluids*, vol. 45, pp. 421-439, 2004.
- [8] MUKHERJEE, S., BERGHOUT, P., VAN DEN AKKER, H. "A Lattice Boltzmann Approach to Surfactant-Laden Emulsions," *AIChE Journal*, vol. 65, no. 2, pp. 811-828, 2019.
- [9] KUPERSHTOKH, A., MEDVEDEV, D. KARPOV, D. "On equations of state in lattice Boltzmann method," *Computers and Mathematics with Applications*, vol. 58, pp. 965-974, 2009.

- [10] KUPERSHTOKH, A. "A lattice Boltzmann equation method for real fluids with the equation of state known in tabular form only in regions of liquid and vapor phases," *Computers and Mathematics with Applications*, vol. 61, pp. 3537-3548, 2011.
- [11] LIU, H., KANG, Q., LEONARDI, C., *et al.* "Multiphase lattice Boltzmann simulations for porous media applications," *Comput Geosci*, vol. 20, pp. 777-805, 2016.
- [12] SHARMA, K.V., STRAKA, R., TAVARES, F.W. "Current status of Lattice Boltzmann Methods applied to aerodynamic, aeroacoustic, and thermal flows," *Prog Aero Sci*, vol. 115, no. 100616, 2020.
- [13] MINO, Y., HASEGAWA, A., SHINTO, H. *et al.*, "Lattice-Boltzmann flow simulation of an oil-in-water emulsion through a coalescing filter: Effects of filter structure," *Chemical Engineering Science*, vol. 177, pp. 210-217, 2018.
- [14] YI, J., XING, H., WANG, J., *et al.* "Pore-scale study of the effects of surface roughness on relative permeability of rock fractures using lattice Boltzmann method," *Chemical Engineering Science*, vol. 209, no. 115178, 2019.
- [15] SHAN, X., CHEN, H. "Lattice Boltzmann model for simulating flows with phases and components," *Physical Review E*, vol. 47, pp. 1815-1819, 1993.
- [16] LI, Q., LUO, K., KANG, Q., *et al.* "Lattice Boltzmann methods for multiphase flow and phase-change heat transfer," *Progress in Energy and Combustion Science*, vol. 52, pp. 62-105, 2016.
- [17] CHEN, L., KANG, Q., MU, Y., *et al.* "A critical review of the pseudopotential multiphase lattice Boltzmann model: Methods and applications," *International Journal of Heat and Mass Transfer*, vol. 76, pp. 210-236, 2014.
- [18] PEREIRA, A., LUCAS, S., MIRANDA, C. "Combining molecular dynamics and lattice Boltzmann simulations: a hierarchical computational protocol for microfluidics," *Microfluid. Nanofluid.*, vol. 20, no. 36, pp. 1-15, 2016.
- [19] JU, Y., LIU, P., ZHANG, D.S., *et al.* "Prediction of preferential fluid flow in porous structures based on topological network models: Algorithm and experimental validation," *Sci China Technol Sci*, vol. 61, no. 8, pp. 1217-1227, 2018.

- [20] GUO, Z., SHU, C. Lattice Boltzmann Method and its applications in Engineering, Singapore: World Scientific, 2013.
- [21] KRUGER, T., KUSUMAATMAJA, H., KUZMIN, A., *et al.* The Lattice Boltzmann Method, principles and practice, Switzerland: Springer International Publishing, 2017.
- [22] HARRIS, S. An Introduction to the Theory of the Boltzmann Equation, New York: Holt, Rinehart & Winston, 1971.
- [23] PRIEVE, D. Advanced Fluid Mechanics with Vector Field Theory, Pittsburgh, 2016.
- [24] BIRD, R., STEWART, W., LIGHTFOOT, E. Transport Phenomena, 2 ed., New York: John Wiley & Sons, 2002, p. 914.
- [25] AURSJØ, O., PRIDE, S. "Lattice Boltzmann method for diffusion-limited partial dissolution," *APS Physics. E.*, vol. 92, no. 013306, 2015.
- [26] HOSSEINI, S., DARABIHA, N., THÉVENIN, D. "Mass-conserving advection–diffusion Lattice Boltzmann model for multi-species reacting flows," *Physica A.*, vol. 499, pp. 40-57, 2018.
- [27] CHAI, Z., GUO, X., WANG, L., *et al.* "Maxwell-Stefan-theory-based lattice Boltzmann model for diffusion in multicomponent mixtures," *Phys. Rev. E*, vol. 99, no. 023312, 2019.
- [28] MCQUARRIE, D. Statistical Mechanics, United States of America: Harper & Row, 1976.
- [29] QIAN, Y., D'HUMIÈRES, D., LALLEMAND, P. "Lattice BGK models for Navier-Stokes equation," *Europhys. Lett.*, no. 17, pp. 479-484, 1992.
- [30] VIGGEN, E. *The lattice Boltzmann method with applications in acoustics*, Department of Physics, NTNU, 2009, p. 108.
- [31] GEIER, M., GREINER, A., KORVINK, J.G. "Cascaded digital lattice Boltzmann automata for high Reynolds number flow," *Phys. Rev. E*, vol. 73, no. 066705, 2006.
- [32] LYCETT, D., LUO, K. "Multiphase cascaded lattice Boltzmann method," *Computers and Mathematics with Applications*, vol. 67, pp. 350-362, 2014.

- [33] SHARMA, K.V., STRAKA, R., TAVARES, F.W. "New Cascaded Thermal Lattice Boltzmann Method for simulations of advection-diffusion and convective heat transfer," *International Journal of Thermal Sciences*, vol. 118, pp. 259-277, 2017.
- [34] BOSCH, F., CHIKATAMARLA, S., KARLIN, I. "Entropic multirelaxation lattice Boltzmann models for turbulent flows," *Phys. Rev. E.*, vol. 92, no. 043309, 2015.
- [35] KARLIN, I., GORBAN, A. "Maximum Entropy Principle for Lattice Kinetic Equations," *Physical Review Letters*, vol. 81, no. 1, 1998.
- [36] KARLIN, I., FERRANTE, A., ÖTTINGER, H. "Perfect entropy functions of the Lattice Boltzmann method," *Europhys. Lett.*, vol. 47, pp. 182-188, 1999.
- [37] WAGNER, A. "An H-theorem for the lattice Boltzmann approach to hydrodynamics," *Europhys.*, vol. 44, pp. 144-149, 1998.
- [38] BHATNAGAR, P., GROSS, E., KROOK, M. "A model for collision processes in gases I: Small amplitude processes in charged and neutral one-component systems," *Physical Review*, vol. 94, pp. 511-525, 1954.
- [39] PAN, C., LUO, L.-S., MILLER, C.T. "An evaluation of lattice Boltzmann schemes for porous medium flow simulation," *Comput Fluids*, vol. 35, pp. 898-909, 2006.
- [40] D'HUMIÈRES, D. "Generalized lattice-Boltzmann equations," in *Rarefied Gas Dynamics: Theory and Simulations*, vol. 159, SHIZGAL, B. D., WEAVER, D. P. Eds., Washington, AIAA, 1992, pp. 450-458.
- [41] SUKOP, M., THORNE JR, D. *Lattice Boltzmann Modeling: An Introduction for Geoscientists and Engineers*, New York: Springer, 2006.
- [42] LADD, A.J.C. "Numerical simulations of particulate suspensions via a discretized Boltzmann equation. Part 1. Theoretical foundation," *J Fluid Mech*, vol. 271, pp. 285-309, 1994.
- [43] ZOU, Q., HE, X. "On pressure and velocity boundary conditions for the lattice Boltzmann BGK model," *Physics of Fluids*, vol. 9, no. 7, pp. 1591-1598, 1997.
- [44] KIM, S.H., PITSCH, H. "A generalized periodic boundary condition for lattice Boltzmann method simulation of a pressure driven flow in a periodic geometry," *Phys Fluids*, vol. 19, p. 108101, 2007.

- [45] LI, Q., LUO, K., LI, X. "Forcing scheme in pseudopotential lattice Boltzmann model for multiphase flows," *Physical Review E*, vol. 86, no. 016709, pp. 1-9, 2012.
- [46] KUPERSHTOKH, A., MEDVEDEV, D. "Lattice Boltzmann equation method in electrohydrodynamic problems," *Journal of Electrostatics*, vol. 64, pp. 581-585, 2006.
- [47] GUO, Z., ZHENG, C., SHI, B. "Discrete lattice effects on the forcing term in the lattice Boltzmann method," *Physical Review E*, vol. 65, no. 46308, 2002.
- [48] LUO, L. "Unified Theory of Lattice Boltzmann Models for Nonideal Gases," *Phys. Rev. Lett.*, vol. 81, no. 1618, 1998.
- [49] LADD, A., VERBERG, R. "Lattice-Boltzmann Simulations of Particle-Fluid Suspensions," *Journal of Statistical Physics*, vol. 104, pp. 1191-1251, 2001.
- [50] HE, X., SHAN, X., DOOLEN, G. "Discrete Boltzmann equation model for nonideal gases," *Phys. Rev. E*, vol. 57, no. R13, 1998.
- [51] HUANG, H., KRAFCZYK, M., LU, X. "Forcing term in single-phase and Shan-Chen-type multiphase lattice Boltzmann models," *Physical Review E*, vol. 84, no. 046710, pp. 1-15, 2011.
- [52] LI, Q., LUO, K. "Achieving tunable surface tension in the pseudopotential lattice Boltzmann modeling of multiphase flows," *Physical Review E*, vol. 88, no. 053307, pp. 1-10, 2013.
- [53] LI, Q., LUO, K., LI, X. "Lattice Boltzmann modeling of multiphase flows at large density ratio with an improved pseudopotential model," *Physical Review E*, vol. 87, no. 053301, pp. 1-11, 2013.
- [54] MCCRACKEN, M., ABRAHAM, J. "Multiple-relaxation-time lattice-Boltzmann model for multiphase flow," *Phys. Rev. E*, vol. 71, no. 036701, 2005.
- [55] YU, Z., FAN, L. "Multirelaxation-time interaction-potential-based lattice Boltzmann model for two-phase flow," *Phys. Rev. E*, vol. 82, no. 046708, 2010.
- [56] LATT, J., MALASPINAS, O., KONTAXAKIS, D., *et al.* "Palabos: Parallel Lattice Boltzmann Solver," *Computers & Mathematics with Applications*, vol. 81, pp. 334-350, 2021.

- [57] KRAUSE, M., AVIS, S., KUSUMAATMAJA, H., *et al.* *OpenLB Release 1.4: Open Source Lattice Boltzmann Code. Version 1.4.*, 2020.
- [58] COON, E., PORTER, M., KANG, Q. "Taxila LBM: a parallel, modular lattice Boltzmann framework for simulating pore-scale flow in porous media," *Comput Geosci*, vol. 18, pp. 17-27, 2014.
- [59] BAUER, M., EIBL, S., GODENSCHWAGER, C., *et al.* "waLBerla: A block-structured high-performance framework for multiphysics simulations," *Computers and Mathematics with Applications*, vol. 81, pp. 478-501, 2021.
- [60] DASSAULT SYSTÈMES SIMULIA CORPORATION, "POWERFLOW - CFD SOFTWARE SOLUTION FOR AERODYNAMIC DESIGN," [Online]. Available: <https://www.3ds.com/products-services/simulia/products/powerflow/>. [Accessed April 07th 2021].
- [61] NUMECA INTERNATIONAL, "OMNIS/LB," [Online]. Available: <https://www.numeca.com/product/omnis-lb>. [Accessed April 07th 2021].
- [62] COUETTE, M. "Oscillations tournantes d'un solide de révolution en contact avec un fluide visqueux," *Compt. Rend. Acad. Sci.*, vol. 105, pp. 1064-1067, 1887.
- [63] SKORDOS, P. "Initial and boundary conditions for the lattice Boltzmann method," *Phys. Rev. E*, vol. 48, pp. 4823-4842, 1993.
- [64] CAIAZZO, A. "Analysis of lattice Boltzmann initialization routines," *J. Stat. Phys.*, vol. 121, pp. 37-48, 2005.
- [65] MEI, R., LUO, L.-S., LALLEMAND, P., *et al.* "Consistent initial conditions for lattice Boltzmann simulations," *Comput. Fluids*, vol. 35, pp. 855-862, 2006.
- [66] HOU, S., ZOU, Q., CHEN, S., *et al.* "Simulation of Cavity Flow by the Lattice Boltzmann Method," *Journal of Computational Physics*, vol. 118, no. 2, pp. 329-347, 1995.
- [67] GUNSTENSEN, A., ROTHMAN, D., ZALESKI, S., *et al.* "Lattice Boltzmann model of immiscible fluids," *Physical Review A*, vol. 43, no. 8, pp. 4320-4327, 1991.
- [68] ROTHMAN, D., KELLER, J. "Immiscible cellular-automaton fluids," *Journal of Statistical Physics*, vol. 52, no. 3-4, pp. 1119-1127, 1988.

- [69] SWIFT, M., OSBORN, W., YEOMAN, J. "Lattice Boltzmann simulation of nonideal fluids," *Phys. Rev. Lett.*, vol. 75, no. 5, pp. 830-833, 1995.
- [70] SWIFT, M., ORLANDINI, E., OSBORN, W., *et al.* "Lattice Boltzmann simulations of liquid-gas and binary fluid systems," *Phys. Rev. E*, vol. 54, no. 5041, 1996.
- [71] HE, X., CHEN, S., ZHANG, R. "A Lattice Boltzmann Scheme for Incompressible Multiphase Flow and Its Application in Simulation of Rayleigh–Taylor Instability," *J. Comput. Phys.*, vol. 152, no. 2, pp. 642-663, 1999.
- [72] SBRAGAGLIA, M., SHAN, X. "Consistent pseudopotential interactions in lattice Boltzmann models," *Physical Review E*, vol. 84, no. 036703, pp. 1-6, 2011.
- [73] YANG, C., HE, H. "Simulation of liquid-vapour phase transitions and multiphase flows by an improved lattice Boltzmann model," *International Journal of Computational Fluid Dynamics*, vol. 29, pp. 423-433, 2016.
- [74] YUAN, P., SCHAEFER, L. "Equations of state in a lattice Boltzmann model," *Phys. Fluids*, vol. 18, pp. 1-11, 2006.
- [75] BAO, J., SCHAEFER, L. "Lattice Boltzmann equation model for multi-component multi-phase flow with high density ratios," *Applied Mathematical Modelling*, vol. 37, pp. 1860-1871, 2013.
- [76] HU, A., LI, L., UDDIN, R. "Force Method in a Pseudo-potential Lattice Boltzmann Model," *J. Comput. Phys.*, vol. 294, pp. 78-89, 2015.
- [77] WAGNER, A., POOLEY, C. "Interface width and bulk stability: Requirements for the simulation of deeply quenched liquid-gas systems," *Physical Review E*, vol. 76, no. 045702, 2007.
- [78] SBRAGAGLIA, M., BENZI, R., BIFERALE, L. "Generalized lattice Boltzmann method with multirange pseudopotential," *Physical Review E*, vol. 75, no. 026702, pp. 1-13, 2007.
- [79] LYCETT-BROWN, D., LUO, K. "Improved forcing scheme in pseudopotential lattice Boltzmann methods for multiphase flow at arbitrarily high density ratios," *Physical Review E*, vol. 91, no. 023305, pp. 1-12, 2015.

- [80] SHAN, X. "Analysis and reduction of the spurious current in a class of multiphase lattice Boltzmann models," *Physical Review E*, vol. 73, no. 047701, pp. 1-4, 2006.
- [81] PENG, C., AYALA, L., AYALA, O., *et al.* "Isotropy and spurious currents in pseudo-potential multiphase lattice Boltzmann models," *Computers and Fluids*, vol. 191, no. 104257, 2019.
- [82] MONTESSORI, A., FALCUCCI, G., LA ROCCA, M. "Three-Dimensional Lattice Pseudo-Potentials for Multiphase Flow Simulations at High Density Ratios," *J Stat Phys*, no. DOI: 10.1007/s10955-015-1318-6, 2015.
- [83] GONG, S., CHENG, P. "Numerical investigation of droplet motion and coalescence by an improved lattice Boltzmann model for phase transitions and multiphase flows," *Computers & Fluids*, vol. 53, pp. 93-104, 2012.
- [84] CHIKATAMARLA, S.S., ANSUMALI, S., KARLIN, I.V. "Entropic Lattice Boltzmann Models for Hydrodynamics in Three Dimensions," *Phys. Rev. Lett.*, vol. 97, no. 010201, 2006.
- [85] ROSIS, A., COREIXAS, C. "Multiphysics flow simulations using D3Q19 lattice Boltzmann methods based on central moments," *Phys. Fluids*, vol. 32, no. 117101, 2020.
- [86] ASADI, M., ZENDEHBOUDI, S. "Hybridized method of pseudopotential lattice Boltzmann and cubic-plus-association equation of state assesses thermodynamic characteristics of associating fluids," *Phys. Rev. E.*, vol. 100, no. 043302, pp. 1-14, 2019.
- [87] ZHANG, R., CHEN, H. "Lattice Boltzmann method for simulations of liquid-vapor thermal flows," *Physical Review E*, vol. 67, no. 066711, pp. 1-15, 2003.
- [88] STILES, C., XUE, Y. "High density ratio lattice Boltzmann method simulations of multicomponent multiphase transport of H<sub>2</sub>O in air," *Computers and Fluids*, vol. 131, pp. 81-90, 2016.
- [89] ZACHARIAH, G.T., PANDA, D., SURASANI, V.K. "Lattice Boltzmann simulations for invasion patterns during drying of capillary porous media," *Chemical Engineering Science*, vol. 196, pp. 310-323, 2019.

- [90] NEMATI, M., ABADY, A., TOGHRAIE, D., *et al.* "Numerical investigation of the pseudopotential lattice Boltzmann modeling of liquid-vapor for multi-phase flows," *Physica A: Statistical Mechanics and its Applications*, vol. 489, pp. 65-77, 2018.
- [91] KUPERSHTOKH, A., MEDVEDEV, D., GRIBANOV, I. "Thermal lattice Boltzmann method for multiphase flows," *Physical Review E*, vol. 98, no. 023308, pp. 1-10, 2018.
- [92] MÁRKUS, A., HÁZI, G. "Simulation of evaporation by an extension of the pseudopotential lattice Boltzmann method: A quantitative analysis," *Physical Review E*, vol. 83, no. 046705, 2011.
- [93] DOU, S., HAO, L. "Numerical study of droplet evaporation on heated flat and micro-pillared hydrophobic surfaces by using the lattice Boltzmann method," *Chemical Engineering Science*, vol. 229, no. 116032, 2021.
- [94] HU, A., LI, L., CHEN, S., *et al.* "On equations of state in pseudo-potential multiphase lattice Boltzmann model with large density ratio," *International Journal of Heat and Mass Transfer*, vol. 67, pp. 159-163, 2013.
- [95] ZENG, J., LI, L., LIAO, Q., *et al.* "Simulation of phase transition process using lattice Boltzmann method," *Chinese Science Bulletin*, vol. 54, pp. 4596-4603, 2009.
- [96] KUPERSHTOKH, A., KARPOV, D., MEDVEDEV, D. "Stochastic models of partial discharge activity in solid and liquid dielectrics," *IET Sci. Meas. Technol.*, vol. 1, no. 6, pp. 303-311, 2007.
- [97] ZHANG, L., ZHU, Y., CHENG, X. "Numerical investigation of multi-droplets deposited lines morphology with a multiple-relaxation-time lattice Boltzmann model," *Chemical Engineering Science*, vol. 171, pp. 534-544, 2017.
- [98] ASADI, M., DE ROSIS, A., ZENDEHBOUDI, S. "Central-Moments-Based Lattice Boltzmann for Associating Fluids: A New Integrated Approach," *The Journal of Physical Chemistry B*, vol. 124, pp. 2900-2913, 2020.
- [99] ZHANG, J., TIAN, F. "A bottom-up approach to non-ideal fluids in the lattice Boltzmann method," *A Letters Journal Exploring The Frontiers of Physics*, vol. 81, no. 66005, 2008.

- [100] SHAN, X. "Pressure tensor calculation in a class of nonideal gas lattice Boltzmann models," *Physical Review E*, vol. 77, no. 066702, pp. 1-6, 2008.
- [101] EATON, J., BATEMAN, D., HAUBERG, S., *et al.*, *GNU Octave version 5.1.0 manual: a high-level interactive language for*, 2019.
- [102] ZARGHAMI, A., LOOIJIE, N., VAN DEN AKKER, H. "Assessment of interaction potential in simulating nonisothermal multiphase systems by means of lattice Boltzmann modeling," *Physical Review E*, vol. 92, no. 023307, 2015.
- [103] LAMB, H. "On the Oscillations of a Viscous Spheroid," *London Mathematical Society*, vol. 13, no. 1, pp. 51-70, 1881.
- [104] AALILIJA, A., GANDIN, C.-A., HACHEM, E. "On the analytical and numerical simulation of an oscillating drop in zero-gravity," *Computers and Fluids*, vol. 197, no. 104362, 2020.
- [105] KUMAR, S., MANDAL, A. "A comprehensive review on chemically enhanced water alternating gas/CO<sub>2</sub> (CEWAG) injection for enhanced oil recovery," *J Petrol Sci Eng*, vol. 157, pp. 696-715, 2017.
- [106] QIN, T., GOUAL, L., PIRI, M., *et al.* "Nanoparticle-stabilized microemulsions for enhanced oil recovery from heterogeneous rocks," *Fuel*, vol. 274, no. 117830, 2020.
- [107] MICHAEL, H.A., KHAN, M.R. "Impacts of physical and chemical aquifer heterogeneity on basin-scale solute transport: Vulnerability of deep groundwater to arsenic contamination in Bangladesh," *Adv Water Resour*, vol. 98, pp. 147-158, 2016.
- [108] PORTOIS, C., BOEIJIE, C.S., BERTIN, H.J., *et al.* "Foam for Environmental Remediation: Generation and Blocking Effect," *Transp Porous Med*, vol. 124, pp. 787-801, 2018.
- [109] NIMMO, J.R., "Vadose Water," in *Encyclopedia of Inland Waters*, G. E. LIKENS, Ed., Academic Press, 2009, pp. 766-777.
- [110] BHAGAT, A.A.S., KUNTAEGOWDANAHALLI, S.S., PAPAUTSKY, I. "Inertial microfluidics for continuous particle filtration and extraction," *Microfluid Nanofluid*, vol. 7, pp. 217-226, 2009.

- [111] TANYERI, M., RANKA, M., SITTIPOLKUL, N., *et al.* "A microfluidic-based hydrodynamic trap: design and implementation," *Lab Chip*, vol. 11, no. 1786, 2011.
- [112] FISHKIS, O., NOELL, U., DIEHL, L., *et al.* "Multitracer irrigation experiments for assessing the relevance of preferential flow for non-sorbing solute transport in agricultural soil," *Geoderma*, vol. 371, no. 114386, 2020.
- [113] WANG, Y., BRADFORD, S.A., SIMUNEK, J. "Physicochemical Factors Influencing the Preferential Transport of Escherichia coli in Soils," *Vadose Zone J*, vol. 13, no. 1, 2014.
- [114] XIAO, K., WILSON, A.M., LI, H., *et al.* "Crab burrows as preferential flow conduits for groundwater flow and transport in salt marshes: A modeling study," *Adv Water Resour*, vol. 132, no. 103408, 2019.
- [115] KOZUSKANICH, J.C., NOVAKOWSKI, K.S., ANDERSON, B.C., *et al.* "Anthropogenic Impacts on a Bedrock Aquifer at the Village Scale," *Groundwater*, vol. 52, no. 3, pp. 474-486, 2014.
- [116] DUSEK, J., VOGEL, T., DOHNAL, M., *et al.* "Combining dual-continuum approach with diffusion wave model to include a preferential flow component in hillslope scale modeling of shallow subsurface runoff," *Adv Water Resour*, vol. 44, pp. 113-125, 2012.
- [117] BOUQUET, S., DOUARCHE, F., ROGGERO, F., *et al.* "Characterization of Viscous Fingering and Channeling for the Assessment of Polymer-Based Heavy Oil Displacements," *Transp Porous Med*, vol. 131, pp. 873-906, 2020.
- [118] DONATH, A., KANTZAS, A., BRYANT, S. "Opportunities for Particles and Particle Suspensions to Experience Enhanced Transport in Porous Media: A Review," *Transp Porous Med*, vol. 128, pp. 459-509, 2019.
- [119] GUO, L., LIU, Y., WU, G.-L., *et al.* "Preferential water flow: Influence of alfalfa (*Medicago sativa* L.) decayed root channels on soil water infiltration," *J Hydrol*, vol. 578, no. 124019, 2019.
- [120] CLOTHIER, B.E., GREEN, S.R., DEURER, M. "Preferential flow and transport in soil: progress and prognosis," *Eur J Soil Sci*, vol. 59, pp. 2-13, 2008.

- [121] PARLANGE, J.-Y., HILL, D.E. "Theoretical Analysis of Wetting Front Instability in Soils," *Soil Sci*, vol. 122, no. 4, pp. 236-239, 1976.
- [122] VIBERTI, D., PETER, C., BORELLO, E.S., *et al.* "Pore structure characterization through path-finding and Lattice Boltzmann simulation," *Adv Water Resour*, vol. 141, no. 103609, 2020.
- [123] YEATES, C., YOUSSEF, S., LORENCEAU, E. "Assessing Preferential Foam Flow Paths in 2D Micromodel Using a Graph-Based 2-Parameter Model," *Transp Porous Med*, vol. 133, pp. 23-48, 2020.
- [124] LIU, J., JU, Y., ZHANG, Y., *et al.* "Preferential Paths of Air-water Two-phase Flow in Porous Structures with Special Consideration of Channel Thickness Effects," *Sci Rep*, vol. 9, no. 16204, 2019.
- [125] WEILER, M. "Macropores and preferential flow—a love-hate relationship," *Hydrological Processes*, vol. 31, pp. 15-19, 2017.
- [126] YAO, C., ZHAO, Y., LEI, G., *et al.* "Insert Carbon Nanoparticles for the Assessment of Preferential Flow in Saturated Dual-Permeability Porous Media," *Ind Eng Chem Res*, vol. 56, pp. 7365-7374, 2017.
- [127] MA, B., LIANG, X., LIU, S., *et al.* "Evaluation of diffuse and preferential flow pathways of infiltrated precipitation and irrigation using oxygen and hydrogen isotopes," *Hydrogeol J*, vol. 25, pp. 675-688, 2017.
- [128] VOLKMANN, T.H.M., WEILER, M. "Continual in situ monitoring of pore water stable isotopes in the subsurface," *Hydrol Earth Syst Sci*, vol. 18, pp. 1819-1833, 2014.
- [129] PARVAN, A., JAFARI, S., RAHNAMA, M., *et al.* "Insight into particle retention and clogging in porous media; a pore scale study using lattice Boltzmann method," *Adv Water Resour*, vol. 138, no. 103530, 2020.
- [130] LIU, Q., ZHAO, B., SANTAMARINA, J.C. "Particle Migration and Clogging in Porous Media: A Convergent Flow Microfluidics Study," *JGR Solid Earth*, vol. 124, no. 9, pp. 9495-9504, 2019.

- [131] SHEN, J., NI, R. "Experimental investigation of clogging dynamics inhomogeneous porous medium," *Water Resour Res*, vol. 53, no. 3, pp. 1879-1890, 2017.
- [132] ZHANG, D., ZHANG, R., CHEN, S., *et al.* "Pore-scale study of flow in porous media: scale dependency, REV, and statistical REV," *Geophys Res Lett*, vol. 27, pp. 1195-1198, 2000.
- [133] BLUNT, M.J., BIJELJIC, B., DONG, H., *et al.* "Pore-scale imaging and modelling," *Adv Water Resour*, vol. 51, pp. 197-216, 2013.
- [134] ROTHMAN, D.H. "Cellular-automaton fluids: A model for flow in porous media," *Geophysics*, vol. 53, no. 4, pp. 509-518, 1988.
- [135] JU, Y., GONG, W., CHANG, W., *et al.* "Effects of pore characteristics on water-oil two-phase displacement in non-homogeneous pore structures: A pore-scale lattice Boltzmann model considering various fluid density ratios," *Int J Eng Sci*, vol. 154, no. 103343, 2020.
- [136] SHARMA, K., ARAUJO, O., NICOLINI, J., *et al.* "Laser-induced alteration of microstructural and microscopic transport properties in porous materials: Experiment, modeling and analysis," *Materials and Design*, vol. 155, pp. 307-316, 2018.
- [137] CHAI, Z., SHI, B., LU, J., *et al.* "Non-Darcy flow in disordered porous media: A lattice Boltzmann study," *Comput Fluids*, vol. 39, pp. 2069-2077, 2010.
- [138] KEFAYATI, G.H.R., TANG, H., WANG, X. "A lattice Boltzmann model for thermal non-Newtonian fluid flows through porous media," *Comput Fluids*, vol. 176, pp. 226-244, 2018.
- [139] KASHYAP, D., DASS, A.K. "Two-phase lattice Boltzmann simulation of natural convection in a Cu-water nanofluid-filled porous cavity: Effects of thermal boundary conditions on heat transfer and entropy generation," *Adv Powder Technol*, vol. 29, pp. 2707-2724, 2018.
- [140] GUO, Z., ZHAO, T.S. "Lattice Boltzmann model for incompressible flows through porous media," *Phys Rev E*, vol. 66, no. 3, p. 036304, 2002.
- [141] BLUNT, M.J. *Multiphase Flow in Permeable Media: A Pore-Scale Perspective*, Cambridge University Press, 2017.

- [142] RICHARDSON, J., HARKER, J., BACKHURST, J. Coulson and Richardson's Chemical Engineering, 5 ed., vol. 2, Oxford: Butterworth-Heinemann, 2002, p. 1229.
- [143] GUO, B. Well Productivity Handbook: Vertical, Fractured, Horizontal, Multilateral, Multi-fractured, and Radial-Fractured Wells, Gulf Professional Publishing, 2019.
- [144] CLENNELL, M.B. "Tortuosity: A guide through the maze," *Geological Society of London Special Publications*, vol. 122, pp. 299-344, 1997.
- [145] MCKIBBIN, R. "Mathematical Models for Heat and Mass Transport in Geothermal Systems," in *Transport Phenomena in Porous Media*, Elsevier Ltd., 1998, pp. 131-154.
- [146] GUO, P. "Dependency of Tortuosity and Permeability of Porous Media on Directional Distribution of Pore Voids," *Transp Porous Med*, vol. 95, pp. 285-303, 2012.
- [147] TAKHANOV, D. "Forchheimer Model for Non-Darcy Flow in Porous Media and Fractures," 2011.
- [148] DUKHIN, A.S., GOETZ, P.J. "Bulk viscosity and compressibility measurement using acoustic spectroscopy," *J Chem Phys*, vol. 130, no. 124519, 2009.
- [149] HUANG, H., AYOUB, J. "Applicability of the Forchheimer Equation for Non-Darcy Flow in Porous Media," *SPE*, pp. 112-122, 2008.
- [150] IRIARTE, J., HEGAZY, D., KATSUKI, D., *et al.* "Fracture Conductivity Under Triaxial Stress Conditions," in *Hydraulic Fracture Modeling*, 2018, pp. 513-525.
- [151] TANG, T., YU, P., YU, S., *et al.* "Connection between pore-scale and macroscopic flow characteristics of recirculating wake behind a porous cylinder," *Phys Fluids*, vol. 32, no. 083606, 2020.

# Appendix A

## Perturbation theory

The perturbation theory is a method for solving algebraic or differential equations, linear or not, generally applied when the resolution is cumbersome, or there is no analytical solution. It is an alternative to Taylor's expansion, which may not converge or incorrectly represent the real behavior of the function depending on which one is selected. The perturbation theory is summarized in the expansion of a variable of interest  $r$  as:

$$r = r_0 + \epsilon r_1 + \epsilon^2 r_2 + \epsilon^3 r_3 + \dots , \quad (\text{A.1})$$

where  $\epsilon$  is a small parameter.

The solution of the following quadratic equation will be exemplified to demonstrate the method.

$$r^2 - 2\epsilon r - 9 = 0 \quad (\text{A.2})$$

The analytical solution of Equation (A.2) is:

$$r = \frac{2\epsilon \pm \sqrt{4\epsilon^2 + 36}}{2} \quad (\text{A.3})$$

Through asymptotic expansion and neglecting terms of order equal to or greater than  $\mathcal{O}(\epsilon^3)$ , we write  $r$  as:

$$r = m_0 + \epsilon m_1 + \epsilon^2 m_2 + \mathcal{O}(\epsilon^3) \quad (\text{A.4})$$

Equation (A.4) should be replaced in the central equation, Equation (A.2). Initially, the term  $r^2$  can be evaluated first. Thus, performing a binomial expansion when Equation (A.4) is replaced in  $r^2$  and neglecting terms of order equal to or greater than  $\mathcal{O}(\epsilon^3)$ :

$$r^2 = r_0^2 + 2\epsilon^2 r_0 r_1 + 2\epsilon r_0 r_2 + \epsilon^2 r_1^2 \quad (\text{A.5})$$

Now replacing Equations (A.4) and (A.5) into Equation (A.2),

$$r_0^2 + 2\epsilon(r_0 r_1 + \epsilon r_0 r_2) + \epsilon^2 r_1^2 - 2\epsilon(r_0 + \epsilon r_1 + \epsilon^2 r_2) = 9 \quad (\text{A.6})$$

Again, neglecting terms of order equal to or greater than  $\mathcal{O}(\epsilon^3)$ ,

$$r_0^2 + 2\epsilon(r_0 r_1 + \epsilon r_0 r_2) + \epsilon^2 r_1^2 - 2\epsilon(r_0 + \epsilon r_1) = 9 \quad (\text{A.7})$$

Identifying the different degrees related to  $\epsilon$ :

$$\mathcal{O}(\epsilon^0): r_0^2 = 9 \quad (\text{A.8})$$

$$\mathcal{O}(\epsilon^1): 2r_0 r_1 - 2r_0 = 0 \quad (\text{A.9})$$

$$\mathcal{O}(\epsilon^2): 2r_0 r_2 + r_1^2 - 2r_1 = 0 \quad (\text{A.10})$$

From Equations (A.8) and (A.9), respectively, we find that  $r_0 = \pm 3$  and  $r_1 = 1$ . Substituting  $r_0$  and  $r_1$  into Equation (A.10), we determine  $r_2 = \pm 1/6$ . Finally substituting these values into the asymptotic expansion of  $r$ , i.e., Equation (A.4), the solution of the chosen quadratic equation through the perturbation theory is:

$$r = \pm 3 + \epsilon \pm \frac{1}{6}\epsilon^2 \quad (\text{A.11})$$

The lower  $\epsilon$  is, the more accurate the solution will be. To demonstrate this, Figure A.1 compares the solution through perturbation theory with the analytical solution. The perturbation theory agrees well with the analytical solution only in the range of small  $\epsilon$ ; it diverges, however, when  $\epsilon > 1$ .

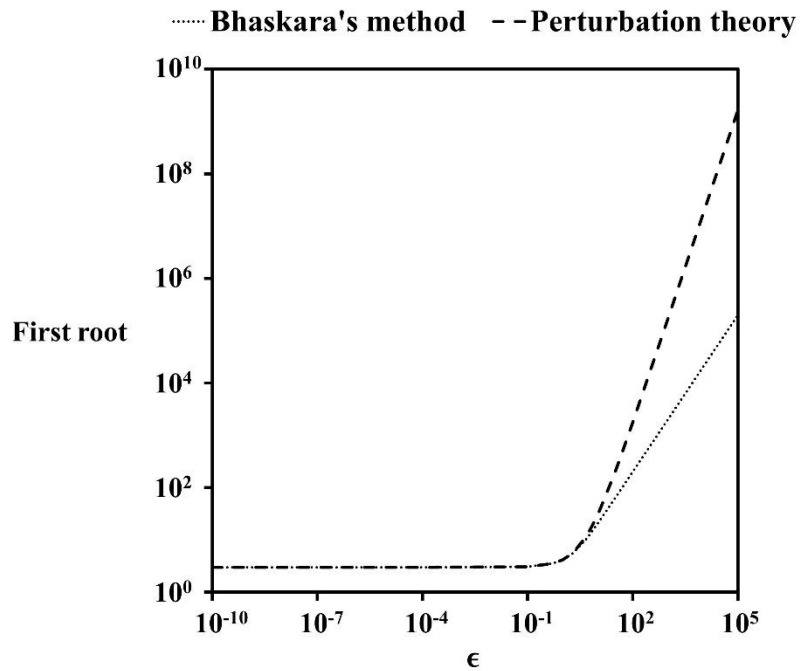


Figure A.1: The logarithmic plot compares the analytical first roots of the quadratic equation with the ones from perturbation theory.

# Appendix B

## Moments and isotropy in LBM

The zeroth and first-order moments are, respectively,

$$\rho = \sum_i f_i \quad (\text{B.1})$$

$$\rho \vec{u} = \sum_i \vec{c}_i f_i \quad (\text{B.2})$$

To define the second-order moment, we define, first, the tensor  $\mathbf{Q}_i$  as:

$$\mathbf{Q}_i = \vec{c}_i \vec{c}_i - c_s^2 \mathbf{I} \quad (\text{B.3})$$

and then multiply it by  $f_i^{(k)}$ , where  $k$  is the order in the Chapman-Enskog expansion,

$$\mathbf{Q}_i f_i^{(k)} = \vec{c}_i \vec{c}_i f_i^{(k)} - c_s^2 \mathbf{I} f_i^{(k)} \quad (\text{B.4})$$

We define the second-order moment  $\boldsymbol{\pi}^{(k)}$  when we sum  $\mathbf{Q}_i f_i^{(k)}$  over all  $i$  possibilities,

$$\boldsymbol{\pi}^{(k)} = \sum_i \mathbf{Q}_i f_i^{(k)} = \sum_i \vec{c}_i \vec{c}_i f_i^{(k)} - c_s^2 \mathbf{I} \sum_i f_i^{(k)} \quad (\text{B.5})$$

Similarly, we can write the third-order moment  $\mathbf{R}^{(k)}$ ,

$$\mathbf{R}^{(\mathbf{k})} = \sum_i \vec{c}_i \vec{c}_i \vec{c}_i f_i^{(k)} \quad (\text{B.6})$$

To ensure the LBM equations will recover the transport equations, the weights  $\omega_i$  must be correctly chosen. In this way, the isotropy conditions (independent of the orthogonal transformations) are imposed in the lattice model. The combination and solution of them makes the  $\omega_i$  values to arise. The isotropy conditions are:

$$\sum_i \omega_i = 1 \quad (\text{B.7})$$

$$\sum_i \omega_i \vec{c}_i = \sum_i \omega_i c_{i\alpha} = \vec{0} \quad (\text{B.8})$$

$$\sum_i \omega_i \vec{c}_i \vec{c}_i = \sum_i \omega_i c_{i\alpha} c_{i\beta} = c_s^2 \delta_{\alpha\beta} \quad (\text{B.9})$$

$$\sum_i \omega_i \vec{c}_i \vec{c}_i \vec{c}_i = \sum_i \omega_i c_{i\alpha} c_{i\beta} c_{i\gamma} = \mathbf{0} \quad (\text{B.10})$$

$$\sum_i \omega_i \vec{c}_i \vec{c}_i \vec{c}_i \vec{c}_i = \sum_i \omega_i c_{i\alpha} c_{i\beta} c_{i\gamma} c_{i\delta} = c_s^4 (\delta_{\alpha\beta} \delta_{\gamma\delta} + \delta_{\alpha\gamma} \delta_{\beta\delta} + \delta_{\alpha\delta} \delta_{\beta\gamma}) \quad (\text{B.11})$$

$$\sum_i \omega_i \vec{c}_i \vec{c}_i \vec{c}_i \vec{c}_i \vec{c}_i = \sum_i \omega_i c_{i\alpha} c_{i\beta} c_{i\gamma} c_{i\delta} c_{i\epsilon} = \mathbf{0} \quad (\text{B.12})$$